

# Visible-to-THz near-field nanoscopy

Rainer Hillenbrand<sup>1,2</sup>✉, Yohannes Abate<sup>3</sup>✉, Mengkun Liu<sup>4,5</sup>✉, Xinzhong Chen<sup>4,6</sup> & D. N. Basov<sup>6</sup>

## Abstract

Optical microscopy has a key role in research, development and quality control across a wide range of scientific, technological and medical fields. However, diffraction limits the spatial resolution of conventional optical instruments to about half the illumination wavelength. A technique that surpasses the diffraction limit in the wide spectral range between visible and terahertz frequencies is scattering-type scanning near-field optical microscopy (s-SNOM). The basis of s-SNOM is an atomic force microscope in which the tip is illuminated with light from the visible to the terahertz spectral range. By recording the elastically tip-scattered light while scanning the sample below the tip, s-SNOM yields near-field optical images with a remarkable resolution of 10 nm, simultaneously with the standard atomic force microscopic topography image. This resolution is independent of the illumination wavelength, rendering s-SNOM a versatile nanoimaging and nanospectroscopy technique for fundamental and applied studies of materials, structures and phenomena. This Review presents an overview of the fundamental principles governing the measurement and interpretation of near-field contrasts and discusses key applications of s-SNOM. We also showcase emerging developments that enable s-SNOM to operate under various environmental conditions, including cryogenic temperatures, electric and magnetic fields, electrical currents, strain and liquid environments. All these recent developments broaden the applicability of s-SNOMs for exploring fundamental solid-state and quantum phenomena, biological matter, catalytic reactions and more.

## Sections

Introduction

Basic near-field probing mechanism

Instrumentation

Near-field probing mechanisms

Near-field spectroscopic material response

Modelling of near-field images and spectra

s-SNOM with distinct sample environments

Applications

Perspectives

<sup>1</sup>CIC nanoGUNE BRTA and Department of Electricity and Electronics at UPV/EHU, Donostia-San Sebastián, Spain.

<sup>2</sup>Ikerbasque, Basque Foundation for Science, Bilbao, Spain. <sup>3</sup>Department of Physics and Astronomy, University of Georgia, Athens, GA, USA.

<sup>4</sup>Department of Physics and Astronomy, Stony Brook University, Stony Brook, NY, USA.

<sup>5</sup>National Synchrotron Light Source II, Brookhaven National Laboratory, Upton, NY, USA. <sup>6</sup>Department of Physics, Columbia University, New York, NY, USA.

✉ e-mail: [r.hillenbrand@nanogune.eu](mailto:r.hillenbrand@nanogune.eu); [yohannes.abate@uga.edu](mailto:yohannes.abate@uga.edu); [mengkun.liu@stonybrook.edu](mailto:mengkun.liu@stonybrook.edu)

## Introduction

Optical imaging and spectroscopy are essential for characterizing materials, structures and phenomena across biology, chemistry and physics. However, conventional far-field techniques cannot resolve features that are smaller than half of the illumination wavelength  $\lambda$ , a constraint imposed by the diffraction limit of light<sup>1</sup>. Several far-field nanoscopy techniques have been developed to circumvent the diffraction limit, such as stimulated emission depletion microscopy, photoactivated localization microscopy and stochastic optical reconstruction microscopy, allowing for routine nanoscale optical imaging<sup>2–4</sup>. These methods are widely used in biological imaging and offer 3D visualization, but they require fluorescent labels and imaging at visible and near-infrared (near-IR) frequencies, which may limit access to intrinsic material properties. For non-fluorescent materials in which labelling is not feasible or informative (such as hard solids), label-free nanoscale optical imaging and spectroscopy tools become essential.

Here, we review a versatile technique known as scattering-type scanning near-field optical microscopy (s-SNOM), also referred to as s-NSOM or apertureless SNOM, which enables label-free nanoscale imaging across a broad range of frequencies from visible light to sub-terahertz (sub-THz) radiation. s-SNOM relies on detecting light that is elastically scattered (Rayleigh scattering) at atomic force microscopy (AFM) tips, often utilizing nanoscale optical near-field enhancement at the apex of the tip for local optical probing (Fig. 1). Although s-SNOM is a scanning probe technique inherently limited to studying surfaces and features just below them, its capability for nanoimaging and nano-spectroscopy with wavelength-independent resolution makes it highly valuable across various scientific and technological fields. It offers the advantage of label-free characterization of a wide range of optically active excitations. Specifically, s-SNOM is sensitive to mobile carrier oscillations (plasmons) at THz, IR and visible frequencies and to lattice and molecular vibrations (phonons) primarily in the THz and IR ranges. It can also probe excitons in the visible range, providing insights into electronic transitions. These capabilities enable s-SNOM to reveal detailed information about local conductivity, crystallinity, chemical composition, electronic band structure and optical properties in numerous solid-state and soft-matter samples.

The idea to circumvent the diffraction limit via SNOM dates back to Edward Hutchinson Syngé, who proposed creating an optical image with subwavelength resolution by scanning a subwavelength-scale hole in an opaque screen across a sample<sup>5</sup>. This principle was demonstrated for microwaves in 1972 (ref. 6) and for visible light in 1984 (refs. 7,8), leading to the development of SNOM. In the 1990s, a variation of SNOM emerged, detecting light scattered at oscillating scanning probe tips<sup>9–12</sup>, achieving a spatial resolution of  $\lambda/1,000,000$  at radio-wave frequencies<sup>13</sup>. Despite signal demodulation at the oscillation frequency of the tip, this initially named apertureless SNOM suffered from large background scattering, which was mitigated in 2000 by combining signal demodulation at multiples of the tip oscillation frequency<sup>14,15</sup> with amplitude-and-phase-resolved interferometric detection of the tip-scattered light<sup>16</sup>. This breakthrough, combined with established AFM technology, facilitated the advancement and commercialization of s-SNOM, leading to a dynamic and expanding community applying the technique across (nano)photonics, solid-state physics, materials science, geosciences, (bio)chemistry and biology.

Numerous reviews<sup>17–26</sup> cover technical aspects and applications of s-SNOM. Here, we review the broad capabilities of s-SNOM and new

developments, but also provide elementary clarifications, including the role of the tip in various near-field experiments and how s-SNOM material contrasts compare with that of far-field measurements. We conclude with an overview of key applications and a perspective section, in which we briefly compare s-SNOM with other techniques that utilize optical illumination of sharp scanning probe microscopy tips and have been developed in parallel.

## Basic near-field probing mechanism

### Near-field and background scattering

The typical near-field optical probing mechanism of s-SNOM is based on the nanoscale concentration of an illuminating field  $E_{\text{in}}$  by a metalized AFM tip. As demonstrated by numerical simulations and illustrated in Fig. 2a, p-polarized far-field illumination polarizes the tip (black dipole  $p_0$ ) and yields a strongly enhanced and confined near-field spot at the very tip apex<sup>27,28</sup>. When the sample is approached towards the tip, the near-field spot intensifies owing to the reflection of the near field of the tip at the sample surface, which depends on the local complex-valued permittivity of the sample. It yields an additional polarization of the tip. The correspondingly induced dipole  $p_{\text{nf}}$  (Fig. 2a, red vertical arrow) radiates the field  $E_{\text{nf}} \propto p_{\text{nf}}$  (of the same frequency as the incident field, as we consider elastic light scattering), which encodes the local optical properties of the sample.  $p_{\text{nf}}$  arises not solely from a single reflection of the near field of the tip at the sample surface, but rather from multiple near-field scattering events between tip and sample. Additionally, the far-field-induced dipole  $p_0$  radiates a field  $E_{\text{bg}} \propto p_0$ , which represents a major contribution to background scattering and does not contain valuable information about the sample.

### Isolation of near-field signals

To obtain reliable and background-free information about the local optical properties of the sample, exclusively the scattered field  $E_{\text{nf}}$  has to be measured. To suppress  $E_{\text{bg}}$ , the tip is oscillated at a frequency  $\Omega$  with an amplitude  $A$  that is small compared with the illumination wavelength, and the tip-scattered field is detected at a frequency  $n\Omega$  (where  $n \geq 2$ ). We illustrate and explain this procedure in Fig. 2b. Owing to the rapid spatial decay of the near fields at the tip apex,  $|E_{\text{nf}}|$  increases nonlinearly as the tip-sample distance  $h$  decreases. For this reason, the near-field scattering exhibits strong anharmonicity (Fig. 2b, middle) when the tip oscillates sinusoidally as a function of time  $t$  (Fig. 2b, top). By contrast,  $|E_{\text{bg}}|$  changes approximately linearly with  $h$  and thus yields a nearly time-harmonic background scattering (Fig. 2b, bottom). Fourier analysis (FA) of  $E_{\text{bg}}(t)$  and  $E_{\text{nf}}(t)$  yields the Fourier coefficients  $E_{\text{bg},n}$  and  $E_{\text{nf},n}$ . They decrease with increasing  $n$ , but, importantly, the decrease is faster for the background contributions, such that  $E_{\text{bg},n} \rightarrow 0$  for  $n \geq 2$ . Thus, by measuring the tip-scattered field  $E_{\text{sca}} = E_{\text{bg}} + E_{\text{nf}}$  at a frequency  $n\Omega$  with  $n \geq 2$ , one obtains  $E_{\text{sca},n} = E_{\text{bg},n} + E_{\text{nf},n} \simeq E_{\text{nf},n}$ . This method effectively isolates the near-field contribution<sup>14–16,29–31</sup>. It is critical to measure the field rather than the intensity,  $I_{\text{sca}} \propto |E_{\text{sca}}|^2$ , as intensity measurements result in a multiplicative mixing of the near-field and background contributions, preventing the isolation of pure near-field signals<sup>16,32–34</sup>. Furthermore, by using amplitude-resolved and phase-resolved detection (Fig. 3), one can obtain the amplitude  $|E_{\text{nf},n}|$  and phase  $\text{Arg}(E_{\text{nf},n})$  of the pure  $n$ th order near-field scattering signal, which allows for the determination of the sample's local complex-valued permittivity<sup>16,32,35–39</sup> or the mapping of nanoscale near-field distributions<sup>34,40–42</sup> (see the section 'Near-field probing mechanisms').

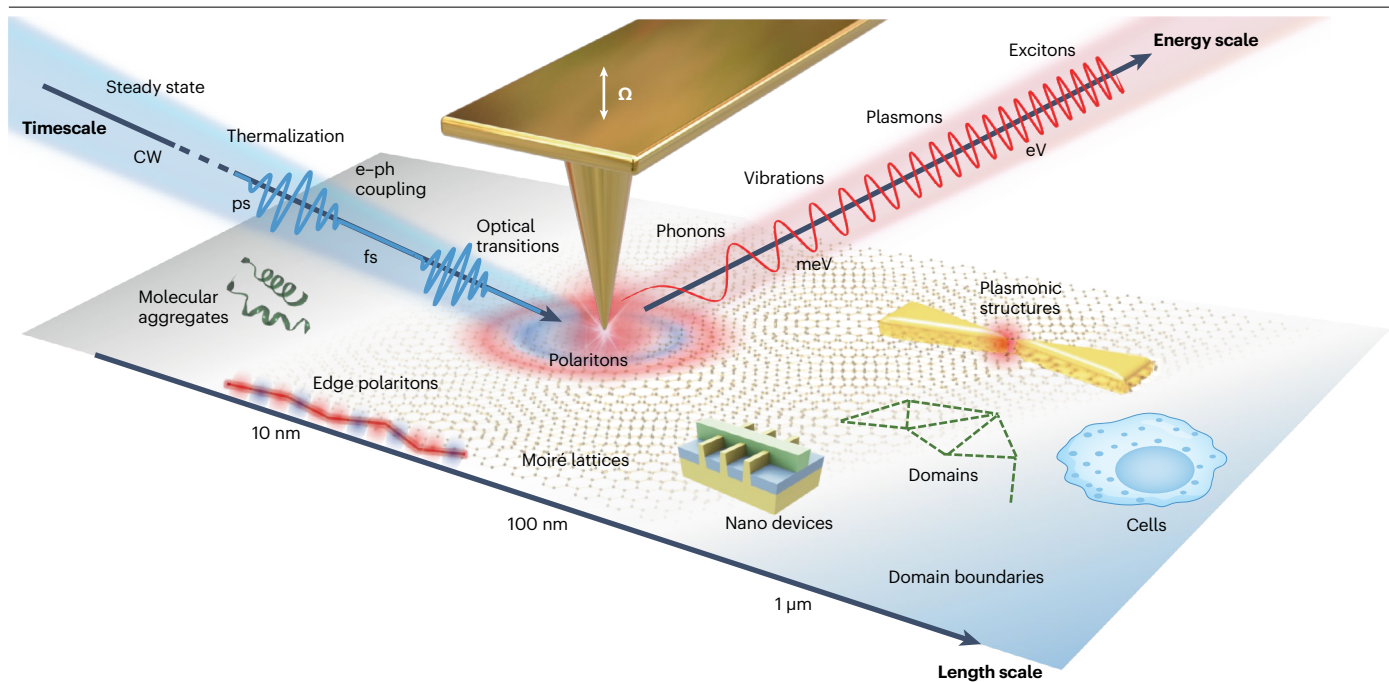


**Fig. 1 | Basic concept of s-SNOM for probing material properties and phenomena throughout various length, time and energy scales.** An atomic force microscopy tip oscillating at a frequency  $\Omega$  is illuminated with a focused light beam. Acting as an optical antenna, the tip concentrates the incident beam into a nanoscale near-field spot (nanofocus) at the very tip apex. The nanofocus diameter is about the size of the tip apex, typically 10–50 nm, and independent of the illumination wavelength. Because of a near-field interaction between the tip and the sample, the tip-scattered light encodes valuable information about the local sample properties. Recording the tip-scattered light while raster-scanning the sample thus yields optical images of the sample surface with nanoscale spatial resolution. The type of illumination can range from monochromatic continuous wave (CW) radiation to broadband femtosecond pulses in the whole visible to sub-terahertz frequency range (corresponding to an energy range of electron volt to millielectron volt) for exploring physical, chemical and biological processes at their native energy, spatial and temporal scales. Examples include the nanoscale probing and

visualization of excitonic and plasmonic responses in the visible and near-infrared (near-IR) range; phonons, plasmon polaritons, phonon polaritons and molecular vibrations in the mid-IR and far-IR range; Drude and plasmonic excitations in the IR–terahertz range. Moreover, with a probing volume of  $<30^3 \text{ nm}^3$  and a scanning area on the order of  $100 \times 100 \mu\text{m}^2$ , scattering-type scanning near-field optical microscopy (s-SNOM) can be employed for examining multi-length-scale phenomena and systems from nanoscopic to mesoscopic scales. These encompass polariton modes confined to sample edges, moiré superlattices, phase domains, semiconductor devices and biological molecular aggregates and cells. When combined with ultrafast time-domain spectroscopy and time-resolved pump-probe techniques, s-SNOM generates time-resolved ‘movies’ capturing ultrafast dynamics, for example, of hot carrier generation, metal–insulator phase percolation and transition and surface plasmon polariton propagation on picosecond-to-femtosecond scales, in addition to the steady states accessible with CW light sources. e, electron; ph, phonon.

## Near-field signal detection and normalization

The tip-scattered field  $E_{\text{sca}}$  from the sample can generally be related to the incident field  $E_{\text{in}}$  through a complex-valued scattering coefficient<sup>16,31,43,44</sup>,  $\sigma_s = s_s e^{i\varphi_s}$ , such that  $E_{\text{sca}} = \sigma_s E_{\text{in}}$ . Accordingly, the background-free demodulated scattered field can be described as  $E_{\text{nf},n} \simeq E_{\text{sca},n} = \sigma_{s,n} E_{\text{in}}$ , in which  $\sigma_{s,n} = s_{s,n} e^{i\varphi_{s,n}}$  is the  $n$ th order Fourier coefficient of  $\sigma_s$  that depends on the local sample permittivity  $\epsilon_s$ . However, in a microscope setup (see the section ‘Instrumentation’), detection of the scattered field combined with signal demodulation yields the complex-valued electrical signals  $S_{s,n} = F E_{\text{nf},n} = F \sigma_{s,n} E_{\text{in}}$ , which are strongly influenced by several factors. These include the transmission of beam splitters, the responsivity of the detector and the precision of the beam alignment (summarized by a factor  $F$ ) as well as the spectral characteristics of the light source,  $E_{\text{in}}$ . To isolate  $\sigma_{s,n}$ , the influence of  $F$  and  $E_{\text{in}}$  is typically eliminated by dividing the complex-valued signal  $S_{s,n}$  by a complex-valued reference signal  $S_{\text{ref},n} = F \sigma_{\text{ref},n} E_{\text{in}}$  from a spectrally flat reference material with a known dielectric permittivity  $\epsilon_{\text{ref}}$

such as gold or silicon<sup>45,46</sup>. This division yields a relative near-field scattering coefficient, often referred to as normalized near-field signal or near-field contrast:

$$\sigma_n = s_n e^{i\varphi_n} \equiv \frac{S_{s,n}}{S_{\text{ref},n}} = \frac{\sigma_{s,n}(\epsilon_s)}{\sigma_{\text{ref},n}(\epsilon_{\text{ref}})}, \quad (1)$$

The relative near-field amplitude and phase signals are given by  $s_n = S_{s,n}/S_{\text{ref},n}$  and  $\varphi_n = \varphi_{s,n} - \varphi_{\text{ref},n}$ , in which  $s_{\text{ref},n}$  and  $\varphi_{\text{ref},n}$  are the amplitude and phase of  $\sigma_{\text{ref},n}$ , respectively. Importantly, referencing is also crucial for a direct comparison of experimental and calculated near-field signals (see the section ‘Modelling of near-field images and spectra’).

We note that in the literature near-field amplitude and phase signals (or spectra) are referred to as normalized near-field amplitude and phase signals, simply near-field amplitude and phase signals (or spectra) or sometimes as near-field amplitude and phase contrasts

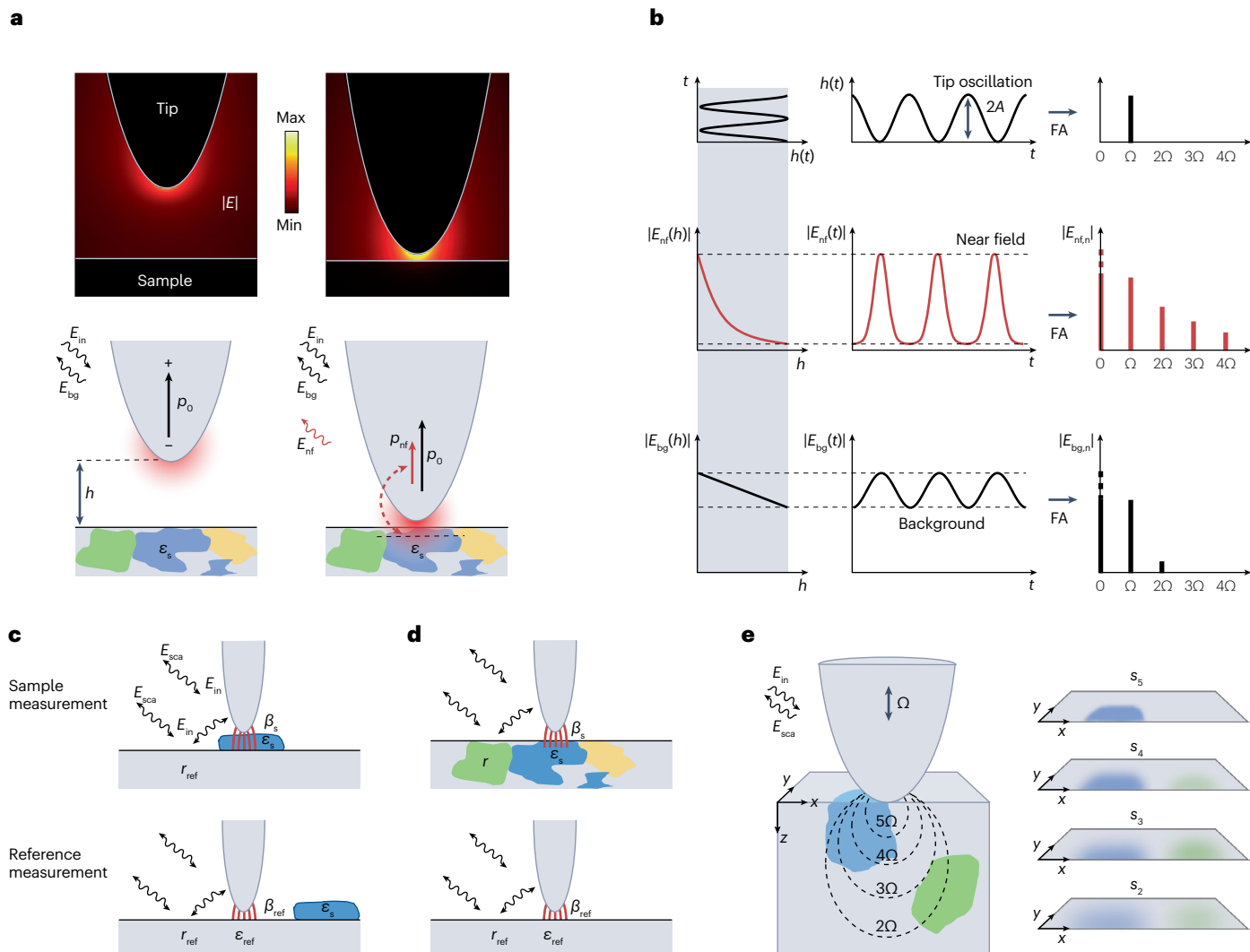


**Fig. 2 | Basic near-field probing mechanism of scattering-type scanning near-field optical microscopy.** **a**, Numerical simulation (top), showing the electric field enhancement and confinement at the apex of a metal tip illuminated with  $p$ -polarized light. Illustration of the near-field scattering process (bottom).  $p_0$  represents the dipole induced by the incident field,  $E_{in}$ , whereas  $p_{nf}$  represents the dipole induced by the tip's near field reflected at the sample surface.  $E_{bg}$  and  $E_{nf}$  represent the fields radiated by  $p_0$  and  $p_{nf}$ , referred as to background and near-field scattering, respectively.  $\epsilon_s$  is the local permittivity of the sample and  $\Omega$  the tip oscillation frequency. **b**, Tip height  $h$  as a function of time  $t$  and Fourier analysis (FA) of  $h(t)$  (top).  $|E_{nf}|$  as a function of  $h$  and  $t$ , as well as FA of

$E_{nf}(t)$  (middle).  $|E_{bg}|$  as a function of  $h$  and  $t$ , as well as FA of  $E_{bg}(t)$  (bottom). **c**, Illustration of near-field signal normalization for the case in which far-field reflections in sample (top) and reference (bottom) measurements cancel out.  $\beta_s$  and  $\beta_{ref}$  indicate near-field reflections.  $r_{ref}$  indicates the far-field reflection at the substrate serving as reference. **d**, Illustration of near-field signal normalization for the case in which far-field reflections in sample ( $r$ , top) and reference ( $r_{ref}$ , bottom) measurements do not cancel out. **e**, Illustration of the sample volumes probed by demodulating the tip-scattered field at  $n\Omega$  (left). The illustrative near-field amplitude images  $s_n$  (right) schematically depict the improved lateral resolution and reduced probing depth as the signal demodulation order  $n$  increases.

(or spectroscopic near-field contrasts). The term near-field amplitude or phase contrast, however, is used in various other contexts, such as to relate the near-field signal of the sample to that of another sample area. These contrasts can arise either from variations in the permittivity of the sample or from differences in the local electromagnetic (EM) fields above the sample surface.

In this Review, we use the following terminology:

- Near-field signals for both non-normalized near-field signals and near-field signals normalized to a reference.
- Near-field spectra for near-field spectra normalized to a reference.

- Near-field material contrasts for contrasts observed in images or spectra arising from spatial or spectral variations of material properties, respectively.

### Consequences of far-field reflection at the sample surface

Up to this point, we have not considered the influence of far-field reflections at the sample surface (Fig. 2c,d). When these reflections are not negligible, the field illuminating the tip is given by  $(1 + cr)E_{in}$ , in which  $r$  is the far-field reflection coefficient of the sample and  $c$  is an unknown weighting factor<sup>31,47–49</sup>. Consequently, the scattered field



# Review article

becomes  $E_{\text{sca}} = (1 + cr)^2 \sigma_s E_{\text{in}}$ , leading to the normalized near-field signal:

$$\sigma_n = \frac{(1 + cr)^2 \sigma_{s,n}}{(1 + cr_{\text{ref}})^2 \sigma_{\text{ref},n}} \quad (2)$$

in which  $r_{\text{ref}}$  is the far-field reflection coefficient for the reference measurement. Equation (2) shows that normalized near-field signals, even after signal demodulation, may contain both near-field and far-field contributions. This mixture can lead to misinterpretation of results, depending on the sample, but may be made

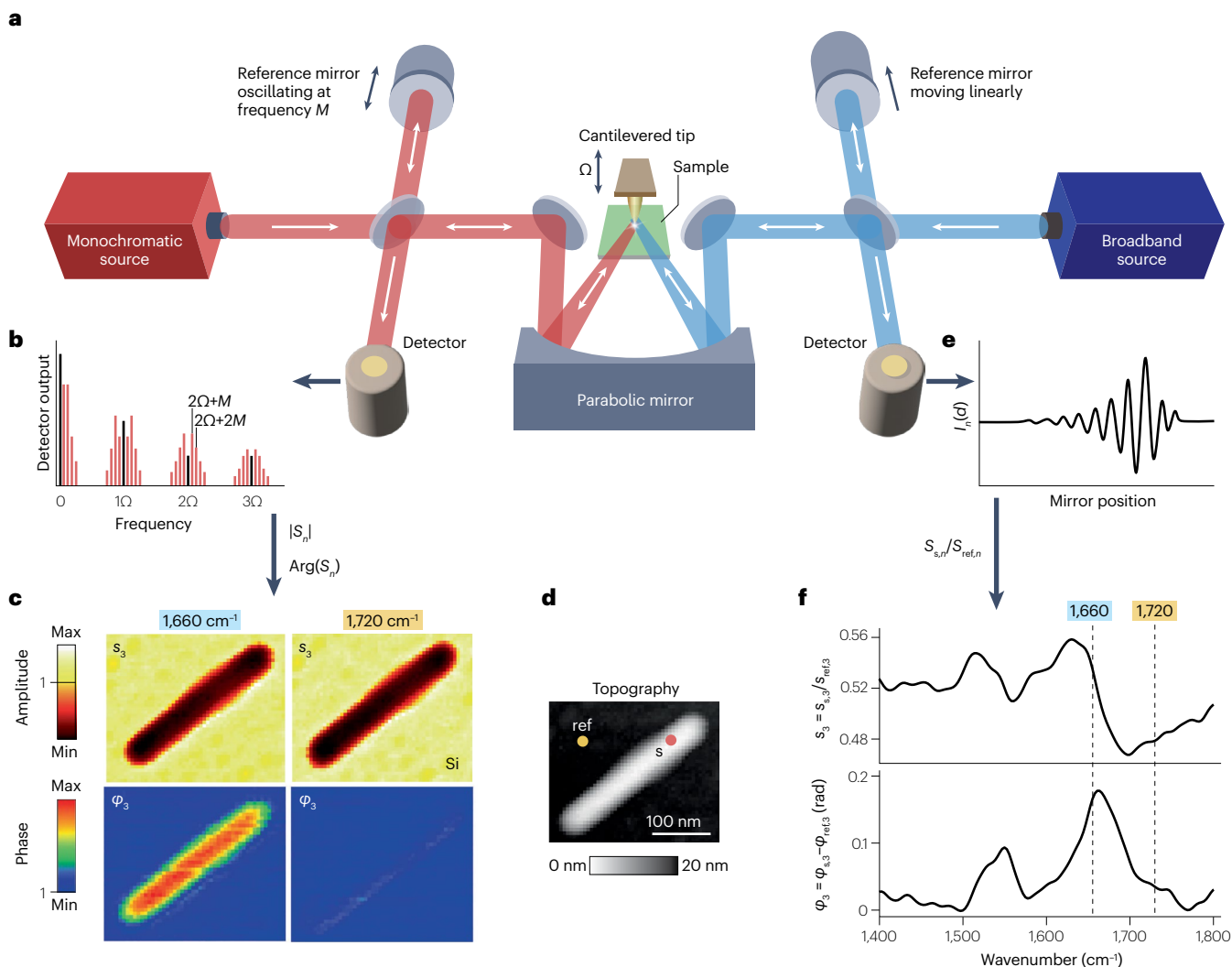


**Fig. 3 | Modern dual-path scattering-type scanning near-field optical microscopy setup.** **a**, Configuration including a monochromatic imaging and a broadband nanoscale Fourier transform infrared (nano-FTIR) spectroscopy module. A parabolic mirror is used for focusing incident light either from the left or the right side onto the atomic force microscopy (AFM) tip oscillating at frequency  $\Omega$ . The parabolic mirror is also used for collecting the tip-scattered light. On the left is the pseudo-heterodyne interferometric detection module, which can operate with various light sources ranging from gas lasers to optical parametric amplifiers. The Michelson-type interferometer uses a reference mirror oscillating at a frequency  $M$  to phase-modulate the reference beam. Detectors are chosen according to the illumination wavelength and used to record the interference between the tip-scattered light and the reference beam. On the right is the Fourier transform spectroscopy module, which can operate with various light sources ranging from broadband laser continua to synchrotron radiation. It is based on a Michelson-type interferometer, in which the reference mirror is linearly translated to be able to record interferograms of the tip-scattered light. In contrast to standard Fourier transform spectroscopy, the sample is located inside one

interferometer arm, yielding amplitude and phase spectra when the interferograms are Fourier-transformed. **b**, Schematic of time-domain Fourier analysis of the detector output for the case of a monochromatic source. Amplitude and phase signals,  $|S_n|$  and  $\text{Arg}(S_n)$ , are calculated in the simplest case from the two signal intensities at  $n\Omega + M$  and  $n\Omega + 2M$  (ref. 32). **c**, Near-field amplitude and phase images of a tobacco mosaic virus (TMV) at  $1,660 \text{ cm}^{-1}$  and  $1,720 \text{ cm}^{-1}$ , normalized to the Si substrate. **d**, AFM topography image of the virus. **e**, To obtain background-free spectra when using a broadband source, the detector signal  $I$  is demodulated at  $n\Omega$  and recorded as a function of the position  $d$  of the reference mirror, yielding asymmetric interferograms  $I_n(d)$ . Fourier transformation of these interferograms and normalization to a reference measurement yield amplitude and phase spectra,  $s_n(\omega)$  and  $\varphi_n(\omega)$  (refs. 37,44,112,114). **f**, Nano-FTIR amplitude and phase spectra of the TMV, showing the typical amide I and II bands of the protein forming the TMV capsid. The spectra were recorded at the position marked by the red dot in the AFM topography image shown in panel **d** and normalized to the reference spectrum at the position marked by the yellow dot. Panel **b** adapted with permission from ref. 32, AIP. Panels **c**, **d** and **f** adapted from ref. 191, CC BY 4.0.

negligible<sup>47,50</sup> or resolved, for example, by changing the sample orientation<sup>47</sup>.

There are two typical scenarios. In the first (Fig. 2c), near-field and far-field contributions are not mixed because the far-field reflection coefficients for the sample and reference measurements are the same. This occurs, for example, when a small object is studied on a substrate serving as the reference. Here, far-field reflections at the position of the object mainly occur at the substrate, such that  $r = r_{\text{ref}}$ , leaving a pure near-field signal as far-field contributions cancel out in equation (2). For more complex samples, similar conditions may be achieved by adjusting the sample orientation<sup>47</sup>. In the second scenario (Fig. 2d), a heterogeneous sample is studied and the reference measurement is performed on a homogeneous material. In this case, the far-field contributions in equation (2) do not cancel out and mix with the near-field signals. This issue can be addressed by analysing the ratio of background-free near-field signals,  $\sigma_n/\sigma_{n-1}$ , in which far-field reflection terms cancel out<sup>47,51,52</sup>, although this reduces the signal-to-noise ratio and near-field contrast. Future developments may offer solutions, such as utilizing multiple near-field signal harmonics<sup>53</sup>.

## Near-field material contrast of low-permittivity materials

For samples with small positive permittivity, such as polymers or biological matter,  $\sigma_n$  is approximately proportional to  $\beta_s$ , where  $\beta_s = (\epsilon_s - 1)/(\epsilon_s + 1)$  is the quasi-electrostatic local near-field reflection coefficient of the sample. Accordingly, near-field amplitude and phase signals are given approximately by  $s_n \propto |\beta_s|$  and  $\varphi_n \propto \text{Arg}[\beta_s]$  (refs. 43,44,46). Interestingly, one also finds the approximate relations  $|\beta_s| \propto |r_s|$  and  $\text{Arg}[\beta_s] \propto A_s$ , in which  $|r_s|^2 = R_s$  is the reflectance and  $A_s$  the absorbance in far-field absorption spectroscopy of macroscopic samples. For this reason,  $s_n$  and  $\varphi_n$  can be related to the local reflectance and absorbance of the sample. A precise quantitative assessment of s-SNOM signals, however, requires careful modelling<sup>43,54</sup>. Furthermore, for materials with negative permittivity values, the above relationships no longer apply. In such cases, accurate modelling becomes essential for even a qualitative understanding of near-field material contrasts<sup>31,45</sup>. For further details, see the sections 'Near-field spectroscopic material response' and 'Modelling of near-field images and spectra'. We note that determining a precise validity range for the above considerations will require future systematic studies.

We note that local sample absorption typically yields a positive phase contrast relative to a non-absorbing reference<sup>43,44,46</sup>. However, thin non-absorbing films on highly reflective substrates may exhibit a negative phase contrast relative to the substrate<sup>36,47,55,56</sup>, with initial studies<sup>57</sup> indicating that this effect arises from larger radiation losses or dissipation when the tip is located directly on the substrate. Although further studies are needed for a more precise understanding, this effect may be corrected through spectroscopic data analysis<sup>57,58</sup>.

## Effects of demodulation order and tip oscillation amplitude

Background suppression largely depends on the oscillation amplitude  $A$  of the tip, the harmonic  $n$  and the illumination wavelength. With increasing demodulation order  $n$  and/or decreasing tip oscillation amplitude  $A$ , the background suppression improves. For example, at visible to IR wavelengths, when the amplitude  $A$  exceeds 40 nm, background-free measurements typically require  $n \geq 3$ . The absence of background can be verified by measuring  $|S_{s,n}|$  and  $|S_{\text{ref},n}|$  as a function of tip-sample distance  $h$  and confirming that these signals rapidly and monotonically decay to the noise floor within distances comparable to the tip radius<sup>16,59,60</sup>. Interestingly, near-field material contrasts<sup>15,16,37,61,62</sup>

and spatial resolution<sup>15,30,61,63–67</sup> increase with increasing  $n$ , the later effect sometimes referred to as effective or virtual tip sharpening<sup>15,68</sup>. For near-field transparent samples, in which subsurface near-field imaging with a probing depth up to a few tip radii is possible<sup>51,59,69–73</sup>, the probing depth decreases as  $n$  or  $A$  increases<sup>30,64,74,75</sup> (Fig. 2e). This effect can be applied for reconstructing the vertical sample composition and for developing near-field optical nanotomography of the sample volume below the sample surface<sup>30,74,76–78</sup>. By contrast, the signal-to-noise (S/N) ratio decreases. For typical tip oscillation amplitudes (midpoint to maximum) between 30 nm and 100 nm, background-free imaging with a sufficiently large S/N ratio can be typically achieved for  $n = 3$  and 4.

## Substrate-enhanced near-field probing

For thin layers and small objects, the near-field amplitude signals, and thus the S/N ratio, can be enhanced by up to an order of magnitude by placing them on highly reflective substrates, such as Si or Au, instead of on low-refractive-index substrates such as CaF<sub>2</sub>. This improvement can be explained by increased tip illumination and scattering via the substrate, along with enhancement of the near fields beneath the tip apex owing to stronger tip-substrate near-field interaction<sup>48,49,73,79,80</sup>. By exploiting polariton-resonant tip-substrate near-field interaction (see the section 'Near-field spectroscopic material response'), an additional signal enhancement can be achieved<sup>148,49,79</sup>.

## Instrumentation

### Basic setup

s-SNOM is typically based on a tapping mode AFM, in which a cantilevered tip is oscillated perpendicular to the sample surface at the resonance frequency  $\Omega$  of the cantilever. A parabolic mirror is typically used for both illumination of the tip and collection of the radiation elastically scattered at the tip (Fig. 3a, middle). For imaging, the sample is scanned beneath the laterally stationary tip, ensuring that the tip remains precisely aligned with the focus of the incident beam.

At visible-to-mid-IR frequencies, standard metal-coated AFM tips with a length of 10–20  $\mu\text{m}$  and a tip apex radius of 20–50 nm are typically used. Although these tips are not optimized for their near-field probing performance, they often provide a sufficiently large S/N ratio and a spatial resolution on the order of the tip radius. However, particularly at THz frequencies, where wavelengths are much longer than the tip lengths, the lightning-rod or antenna effect of standard AFM tips is considerably weaker than at IR frequencies. For this reason, longer tips<sup>81–83</sup> or larger tip apex radii<sup>68,81,84,85</sup> are beneficial, as they yield larger THz near-field signals. It has also been demonstrated that the engineering of geometric antenna resonances can further enhance THz and IR near-field signals<sup>68,83,86</sup>.

### s-SNOM employing monochromatic illumination

s-SNOM is mostly used for nanoimaging with monochromatic light sources. In this case, amplitude-resolved and phase-resolved detection of the tip-scattered radiation is performed with a Michelson-type interferometer combined with higher-harmonic signal demodulation. To this end, the tip-scattered radiation is interfered at the detector with a reference beam reflected at a planar reference mirror (Fig. 3a, left). Complete background suppression requires the reference beam to be either frequency-shifted (heterodyning interferometry)<sup>16,34</sup>, phase-modulated<sup>32</sup>, phase-shifted<sup>87,88</sup> or amplitude-modulated<sup>89</sup>. Both amplitude and phase modulation of the reference beam yield near-field amplitude and phase signals within milliseconds and can be implemented in the whole visible to sub-THz spectral ranges. Typically, phase

modulation of the reference beam and higher-harmonic sideband demodulation are employed (Fig. 3b), a technique known as pseudo-heterodyne detection<sup>32</sup>. Amplitude and phase images are obtained by recording  $|S_n|$  and  $\text{Arg}(S_n)$  while the sample is scanned (Fig. 3c), simultaneously with an AFM topography image (Fig. 3d). The spatial resolution is determined by the size of the near-field spot at the tip apex, which is on the scale of the apex radius.

In the visible-to-near-IR spectral range, the radiation from diode or Ti:Sapphire lasers is often used for tip illumination, whereas quantum cascade lasers (QCLs) are the major light source in the mid-IR spectral range. At THz frequencies, tunable gas lasers can be used<sup>90,91</sup>, but they are expensive and bulky. The emergence of THz-QCLs and self-detection schemes could be a promising compact alternative<sup>92,93</sup>. Even electronically generated and detected sub-THz radiation can be employed for imaging with 50 nm spatial resolution<sup>62,94</sup>. The narrow-band radiation from free-electron lasers can be used as well. As it can be tuned from IR to THz frequencies, it enables s-SNOM applications in the far-infrared spectral range<sup>95–97</sup>. Tunable optical parametric oscillators (OPOs) with linewidth down to a few wavenumbers are emerging sources for s-SNOM imaging from near-IR to mid-IR frequencies<sup>50,98,99</sup>. Pseudo-monochromatic imaging can also be achieved by combining broadband sources with grating monochromators<sup>100–102</sup>.

By repeatedly imaging the sample at various frequencies with a tunable monochromatic source, local spectroscopic information can be extracted from the set of s-SNOM images. This has been demonstrated at THz (refs. 96,103–106), IR<sup>38,46,50,107</sup> and visible frequencies<sup>108</sup>. An alternative and emerging method for obtaining local spectroscopic information is to sweep the frequency of a QCL<sup>109</sup> or narrow-band OPO<sup>110</sup> while keeping the sample position fixed.

### s-SNOM employing broadband illumination

s-SNOM can also be operated with broadband light sources. In its earliest implementation, the tip was illuminated with broadband mid-IR radiation generated by difference-frequency generation and the tip-scattered field was recorded using dual-comb spectroscopy combined with higher-harmonic signal demodulation<sup>111</sup>. To date, the most common implementation uses a Michelson-type interferometer, operated as an asymmetric Fourier transform (FT) spectrometer<sup>37,44,112–116</sup> (Fig. 3a, right, and Fig. 3e). In this setup, the tip and sample are placed in one arm of the interferometer, similar to configurations used with monochromatic illumination. Unlike conventional FT spectroscopy, this arrangement enables the acquisition of both amplitude and phase spectra (Fig. 3f). Combined with higher-harmonic signal demodulation, it thus provides background suppression equivalent to pseudo-heterodyne detection with monochromatic light. However, the lower power of broadband sources often reduces the S/N ratio, requiring signal demodulation at lower harmonics where background suppression is less effective. Originally demonstrated with IR illumination and standard detectors, the technique was termed nanoscale Fourier transform infrared (nano-FTIR) spectroscopy<sup>114</sup>, although it can be also implemented with visible, far-IR<sup>19</sup> and THz radiation<sup>117</sup>.

Nano-FTIR spectroscopy typically employs broadband IR laser<sup>37,44,112,113</sup> or synchrotron radiation<sup>19,21,39,117–119</sup>. In the case of the latter, the technique is often referred to as synchrotron IR nanospectroscopy. Furthermore, argon arc<sup>86,120</sup> or laser-driven<sup>121</sup> plasma sources can be used. The latter may offer a rather compact and economical solution for ultra-broadband spectroscopy, although they significantly lag behind synchrotron radiation in terms of spectral power density and brilliance<sup>122</sup>.

Acquisition times for nano-FTIR spectra can range from several seconds to many minutes. Consequently, spectra are often recorded only at specific sample positions. However, hyperspectral nanoimaging can be achieved by recording nano-FTIR spectra at each pixel of a 2D array across the sample surface<sup>123</sup>. From the resulting hyperspectral data cubes, local spectra or monochromatic images can be extracted. As hyperspectral nanoimaging is slow, sparse sampling techniques are increasingly used to reduce acquisition times<sup>124–128</sup>.

s-SNOM can be also combined with time-domain spectroscopy<sup>129</sup>. In this technique, single-cycle or few-cycle IR or THz pulses are used for tip illumination. The waveforms of the tip-scattered pulses are measured as a function of time by coherent electro-optic or photo-conductive sampling<sup>130</sup>. Subsequent higher-harmonic signal demodulation allows for background-free amplitude-resolved and phase-resolved near-field spectroscopy<sup>71,78,81,131</sup> and hyperspectral nanoimaging<sup>132,133</sup>.

### Near-field probing mechanisms

The electro-dynamics of the tip-sample near-field interaction is multifaceted, but two primary roles of the tip can be discerned (Fig. 4). The enhanced electric near field at the apex, typically of a metal tip, can be harnessed for probing material properties and eventually for launching and detecting EM modes (Fig. 4a–c). In other experiments, the tip is employed for scattering the EM modes that are predominantly excited by the sample itself, for example, by plasmonic antennas (Fig. 4d–f).

### Near-field probing of material properties

Figure 4a illustrates the most basic s-SNOM experiment, with the underlying near-field probing mechanism detailed in Fig. 2a. In the case of monochromatic tip illumination, amplitude and phase images reveal spatial variations of the permittivity of the sample  $\epsilon$ . As a simple example, we show in Fig. 4a a mid-IR near-field amplitude image of SiO<sub>2</sub> patches on an Si surface<sup>134</sup>. The SiO<sub>2</sub> patches appear as dark squares with smaller near-field amplitude than the brighter Si substrate, primarily because SiO<sub>2</sub> has a smaller permittivity than Si at the imaging frequency. By performing amplitude-resolved and phase-resolved spectroscopy using broadband sources or tunable lasers, the local dielectric function,  $\epsilon(\omega)$ , can be determined through theoretical modelling or reconstruction. Having determined  $\epsilon(\omega)$ , various sample properties can be derived, such as chemical composition and structure, crystal properties and mobile carrier concentration, as discussed later.

### Interferometry of propagating EM modes excited by the near field of the tip

When thin layers or nanowires can support strongly confined propagating EM waves, the momentum of the concentrated near field at the tip apex may be large enough to efficiently excite them. These waves (Fig. 4b, red circles) include IR and THz plasmon polaritons in graphene<sup>135,136</sup>, carbon nanotubes<sup>137</sup>, semiconductor nanowires<sup>138</sup> and platelets<sup>106</sup>. Furthermore, the near field of the tip can excite IR and THz phonon polaritons in h-BN flakes<sup>139,140</sup>, BN nanotubes<sup>141</sup>, SiC layers<sup>142</sup>, dielectric-loaded quartz<sup>143</sup> and MoO<sub>3</sub> flakes<sup>96,144,145</sup>. At visible and near-IR frequencies, exciton polaritons<sup>146</sup> and dielectric waveguide modes<sup>146,147</sup> in transition metal dichalcogenide layers can be launched, as well as surface plasmon polaritons (SPPs) on thin gold layers<sup>148,149</sup>. On extended homogeneous surfaces or nanowires, as well as on edges<sup>150–152</sup>, the waves propagate away from the tip without manifesting visually in the near-field images. However, when these EM waves reflect back at discontinuities, such as edges<sup>135,136</sup>, defects<sup>153</sup>, grain boundaries<sup>154,155</sup> or

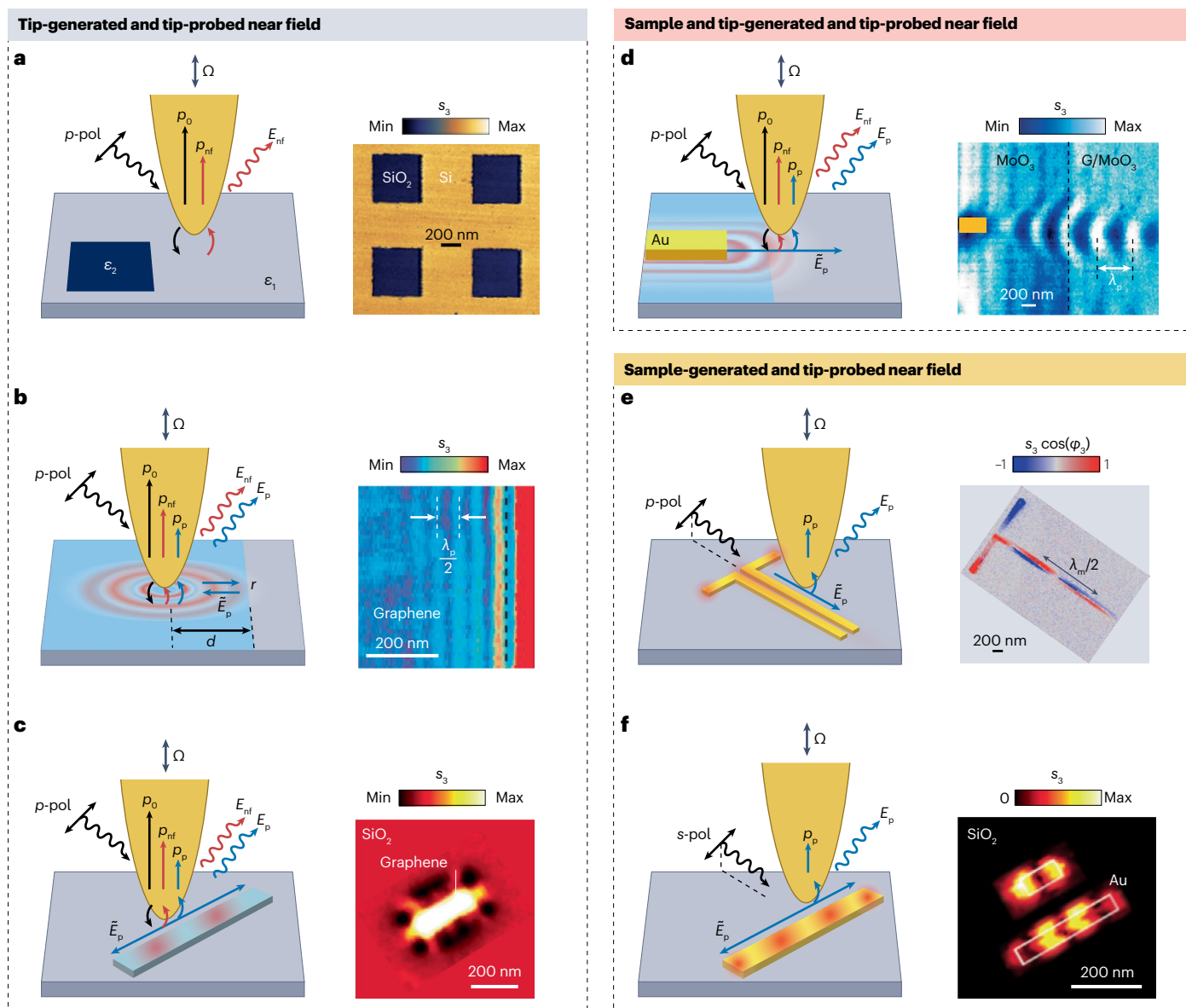


**Fig. 4 | Comparison of near-field probing mechanisms.** **a**, Near-infrared near-field material contrast between Si (larger permittivity ( $\epsilon_1$ )) and  $\text{SiO}_2$  (smaller permittivity ( $\epsilon_2$ )) at  $6,452\text{ cm}^{-1}$ .  $s_3$  is the near-field amplitude. **b**, The near field at the tip apex can additionally excite propagating electromagnetic (EM) waves on the sample. When these waves are reflected at sample discontinuities, they are scattered by the tip and imaged. The example shows an infrared s-SNOM image of graphene plasmon polaritons at  $943\text{ cm}^{-1}$ , manifesting as periodic fringes parallel to the graphene edge. **c**, If the sample is nanostructured, it can act as a resonator structure for the tip-launched waves. The example shows an infrared s-SNOM image of a rectangular graphene plasmon polariton nanoresonator at  $884\text{ cm}^{-1}$ , where the interference of multiple Fabry–Perot modes yields a complex near-field pattern. **d**, Propagating EM waves can be launched at discontinuities or antenna structures on the surface of the sample. The waves are scattered by the tip, allowing to map their wavefronts. The example image at  $893\text{ cm}^{-1}$  shows how phonon polaritons on  $\text{MoO}_3$  (left, launched by an Au antenna) experience negative refraction when they enter the region where the  $\text{MoO}_3$  is covered by graphene (right).

**e**, Applying s-polarized illumination and appropriate sample orientation allows for efficient excitation of EM modes on the sample, whereas the optical excitation of the tip is minimized. The example image shows the antisymmetric propagating mode of a two-wire IR transmission line coupled to a dipole antenna. It was obtained by recording the real part of the p-polarized tip-scattered light at  $1,020\text{ cm}^{-1}$ . **f**, Near-field probing of antenna and nanoresonator modes, with a configuration similar to that in panel **c**, but using an s-polarized illuminating field. The example shows a near-field amplitude image of the first-order and third-order dipolar resonance of Au nanorods at  $10,616\text{ cm}^{-1}$ .  $p_0$ ,  $p_{\text{nf}}$  and  $p_p$  are the dipoles induced, respectively, by the incident field, by the tip's near field reflected at the sample surface and by the electric field generated by the back-reflected EM waves.  $E_{\text{nf}}$  and  $E_p$  indicate the light radiated by the dipoles  $p_{\text{nf}}$  and  $p_p$ , respectively. The light scattered by  $p_0$  is not indicated, as it is not measured.  $\tilde{E}_p$  indicates EM surface waves and  $\lambda_p$  their wavelength. Panel **a** adapted with permission from ref. 134, Elsevier. Panel **b** adapted from ref. 158, Springer Nature Limited. Panel **c** adapted from ref. 150, Springer Nature Limited. Panel **d** adapted with permission from ref. 171, AAAS. Panel **e** adapted with permission from ref. 180, American Chemical Society. Panel **f** adapted with permission from ref. 183, American Chemical Society.



domain walls<sup>156,157</sup>, their electric field  $\tilde{E}_p$  induces an additional polarization (represented by the dipole  $p_p$ ) in the tip, yielding a scattered field  $E_p$  depicted by a blue sine wave. The interference between the radiated fields  $E_{\text{nf}}$  and  $E_p \propto p_p \propto \tilde{E}_p$  subsequently yields interference fringes in both the near-field amplitude  $s_n$  and phase  $\varphi_n$  images. The fringe spacing corresponds to  $\lambda_p/2$ , in which  $\lambda_p = 2\pi/k_p$  is the wavelength of the propagating EM wave. Figure 4b shows as an example the interference fringes of IR plasmon polaritons on high-quality graphene<sup>158</sup>. By measuring the periodicity and decay of the fringes, the dispersion and losses can be determined. Furthermore, various material properties of the sample can be accessed, including isotropic and anisotropic permittivities<sup>147,159</sup>, local optical conductivity<sup>154</sup>, strain<sup>160</sup> and anisotropic electron masses<sup>106</sup>. However, as the tip simultaneously launches and detects the propagating waves, this method does not allow for the direct mapping of the wavefront evolution. For instance, it is not possible to image how the waves propagate across an interface or undergo focusing. This problem can be circumvented when the tip scatters the field of a wave that is launched by structures on the sample rather than by the tip (Fig. 4d).

## Interferometry of localized EM modes excited by the near field of the tip

When the thin layers discussed in the previous section are nanostructured, they can act as resonant cavities for tip-launched waves  $\tilde{E}_p$  (Fig. 4c). The near-field amplitude  $s_n$  and phase  $\varphi_n$  images thus exhibit patterns that can be associated with plasmonic<sup>135,150,151,157</sup> or phononic<sup>161–165</sup> cavity modes. Intriguingly, unlike far-field measurements, s-SNOM can probe not only bright but also dark modes, owing to local mode excitation by the strongly confined near fields at the tip apex. However, the near-field images often do not directly reveal the intrinsic mode profiles. This is because a complex near-field pattern is mapped, which is caused by the interference of the fields  $E_{\text{nf}}$  and  $E_p \propto \tilde{E}_p$  scattered by the dipoles  $p_{\text{nf}}$  and  $p_p$  (refs. 150,155). Furthermore,  $p_p$  may be induced not by the near field of a single cavity mode but by the near field arising from the interference of spatially and spectrally overlapping cavity modes<sup>150</sup>. Reliable mode identification thus requires a careful analysis of the near-field patterns, for example, by comparing them with simulated mode profiles of the cavities under study. Figure 4c shows, as an example, the mid-IR near-field amplitude image of a rectangular graphene cavity. The destructive and constructive interference of the various Fabry–Perot plasmon modes with the near fields below the tip apex yields dark and bright spots relative to the bare SiO<sub>2</sub> substrate, as a consequence of destructive and constructive mode interferences, respectively<sup>150</sup>.

## Interferometry of propagating EM modes excited by near fields of the sample

EM waves can be also excited at the edges of the layers supporting them<sup>148,149,158,166</sup>, as well as by the strongly enhanced near fields generated at the edges of metal layers<sup>167–169</sup> or by antennas<sup>166,170,171</sup> located on the sample. As these near fields can assume much lower momenta than the ones generated at the tip apex of radius  $a$ , EM waves with wavelength much larger than  $a$  can be efficiently launched<sup>168,172</sup>. Figure 4d illustrates the launching of an EM wave by a gold nanorod when  $p$ -polarized illumination is used. The wave of field  $\tilde{E}_p$  propagates away from the launcher and polarizes the tip, represented by the dipole  $p_p$ . This polarization is additional to the one induced in the tip by the tip–sample near-field interaction, represented by the dipole  $p_{\text{nf}}$ . Analogue to the situation in Fig. 4b, interference of the fields  $E_{\text{nf}} \propto p_{\text{nf}}$

and  $E_p \propto p_p$  occurs. However, the interference fringe spacing is now  $\lambda_p$  as long as  $\lambda_p$  is much smaller than the photon wavelength. More importantly, the near-field amplitude  $s_n$  and phase  $\varphi_n$  images reveal the wavefronts and their evolution, which cannot be accomplished when the tip launches the EM wave. This method was applied to visualize the concave wavefronts of a diverging phonon polariton beam on an h-BN metasurface<sup>170</sup> and on in-plane anisotropic MoO<sub>3</sub> flakes<sup>173</sup>. Even the wavefronts of hyperbolic shear phonon polaritons on low-symmetry CdWO<sub>4</sub> crystals could be mapped<sup>174</sup>, as well as the negative refraction and focusing of a diverging in-plane anisotropic phonon polariton beam crossing the straight interface between bare and graphene-covered MoO<sub>3</sub> (ref. 171) (Fig. 4d).

We note that in such experiments the tip can launch EM waves as well. In many cases, the reflection of these waves from the launcher can be neglected and thus does not disturb the wavefront patterns. However, when the tip-launched EM waves reflect efficiently at the launcher or other sample discontinuities back to the tip (Fig. 4b), the additional interference yields fringes with spacing  $\lambda_p/2$  and needs to be considered<sup>158,166</sup>. In some cases, the interference fringes due to tip-launched polaritons might be removed by Fourier filtering the near-field images<sup>175</sup>.

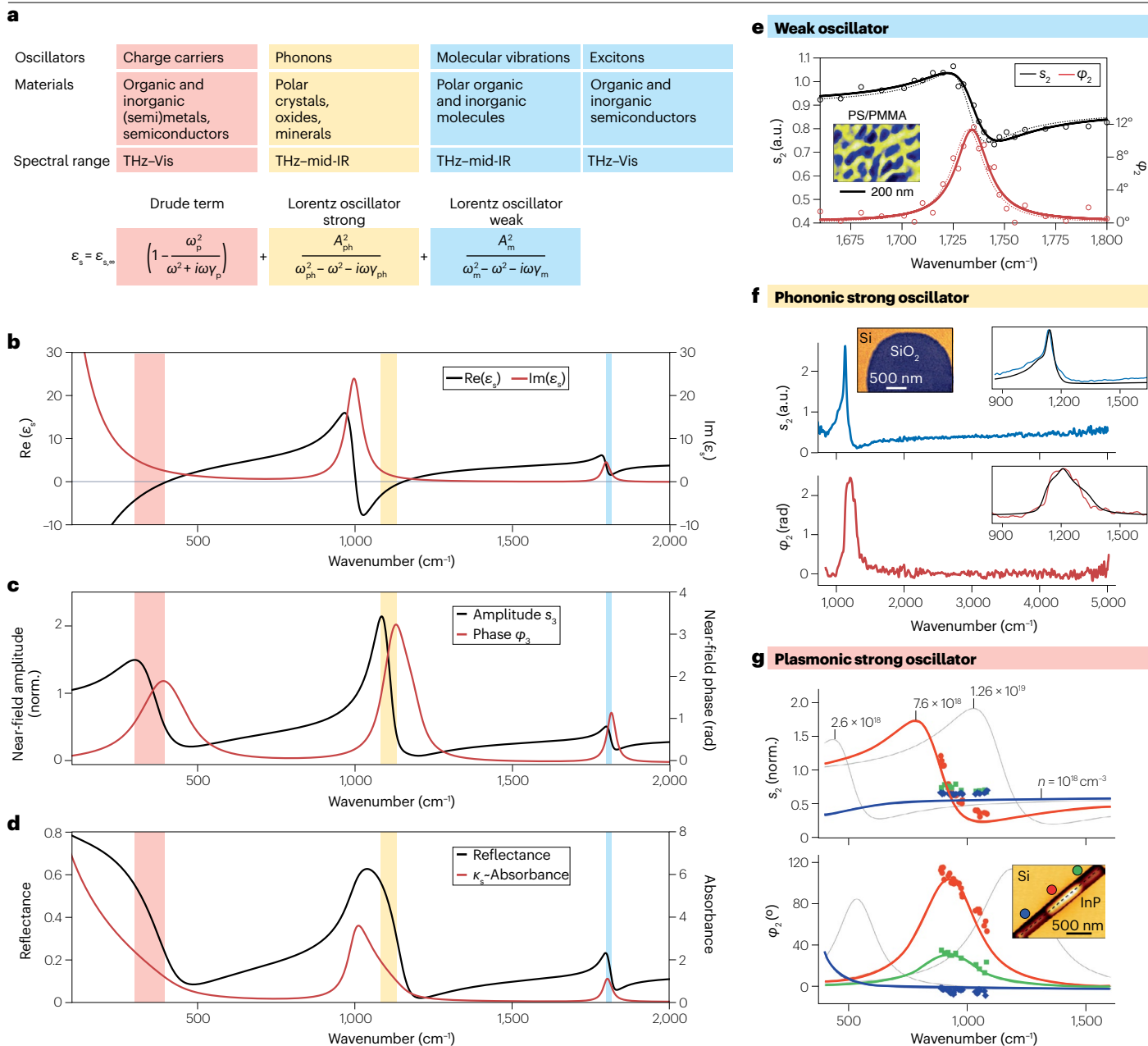
## Mapping the near-field distribution of propagating EM modes

$s$ -polarized far-field illumination can efficiently excite propagating EM modes on the sample, for example, on a metal two-wire transmission line (TL) coupled to a dipole antenna, whereas the direct excitation of the tip is minimized<sup>176–179</sup> (Fig. 4e). Thus, it is essentially the propagating mode that polarizes the tip, as illustrated by the dipole  $p_p$ . Recording the  $p$ -polarized tip-scattered field  $E_p \propto p_p$  thus yields images of the spatial distribution of the vertical near-field component  $E_z$  of the mode, in contrast to the case illustrated in Fig. 4d, in which the interference between  $E_p \propto p_p$  and  $E_{\text{nf}} \propto p_{\text{nf}}$  is mapped. The tip can be illuminated from the side, as shown in the schematic, or from below through a transparent substrate, as in the example experiment, showing a near-field image of a mid-IR mode propagating along the TL. By plotting the real part of the near-field signal,  $s_n \cos(\varphi_n)$ , one can see the periodically changing polarity of the field along the TL. It reveals not only the wavelength of the mode but also that the antisymmetric TL mode is excited, as recognized by the opposite polarity of the field on the two wires<sup>180</sup>. This imaging modality was also applied for visualizing the compression of an IR mode propagating along a tapered TL<sup>176</sup>, near-IR plasmons on tapered gold stripes<sup>177</sup> and slot waveguides<sup>179,181</sup> and optical skyrmion lattices formed by SPPs<sup>182</sup>. Employing side illumination, it was possible to map the refraction of antenna-launched IR graphene plasmons passing through a prism-shaped graphene bilayer<sup>178</sup>.

## Mapping the near-field distribution of resonator EM modes

$s$ -polarized illumination can also be applied for near-field imaging of antenna and nanoresonator modes<sup>41,42</sup> (Fig. 4f). The far-field excited localized modes polarize the tip and induce the dipole  $p_p$  and subsequent far-field scattering  $E_p \propto p_p$ . Owing to the elongation of the tip, out-of-plane near-field components are scattered more efficiently than in-plane near-field components and thus are typically mapped when the  $p$ -polarized tip-scattered field is recorded. This technique offers the advantage of efficiently exciting resonator modes while minimizing the near-field coupling between the tip and the antenna. Furthermore, the images yield the spatial distribution of the vertical near-field component  $E_z$  of the mode, as in the configuration shown in Fig. 4e, in contrast to Fig. 4c, in which the interference between  $E_p \propto p_p$  and  $E_{\text{nf}} \propto p_{\text{nf}}$  is

# Review article



mapped. As an example, Fig. 4f shows a near-field amplitude image of gold nanorods acting as antennas for visible light. It reveals the strong out-of-plane near fields, indicating the first-order and third-order dipolar antenna (nanoresonator) mode<sup>183</sup>. Applications of this imaging modality include the identification of resonator modes<sup>41,42,183–185</sup>. When the  $s$ -polarized tip-scattered field is measured, the nanoscale hot spots in narrow nanoantenna gaps can be mapped<sup>186–188</sup>. However, the interpretation of the near-field images may be more complicated, as the near-field signal generally does not reveal an individual near-field component<sup>189</sup>.

## Near-field spectroscopic material response

In this section, we describe in more detail the near-field material contrast discussed in Figs. 2a and 4a. The reflection of the near field of the

tip at the sample and the associated scattering of the dipole  $p_{\text{nf}}$  are highly sensitive to the complex-valued local dielectric function  $\epsilon_s(\omega)$  of the sample. Recording the tip-scattered field thus allows us to probe various material excitations (Fig. 5a), including collective mobile charge carrier oscillations (plasmons), lattice (phonons) and molecular vibrations and electron–hole pairing (excitons). Plasmons can occur in metallic and semiconducting materials within a wide spectral region, ranging from sub-THz to visible frequencies, and can be often well described by the Drude term. Phonons can be found in polar crystals in the mid-IR to THz spectral range and can be well described by Lorentz oscillators with large oscillator strength. Molecular vibrations and excitons are adequately accounted for by Lorentz oscillators with weaker oscillator strengths. To demonstrate how these distinct contributions manifest

**Fig. 5 | Near-field spectroscopic material contrast.** **a**, Basic optical material excitations. **b**, Dielectric function of an artificial sample material including a Drude term ( $\omega_p = 500 \text{ cm}^{-1}$ ,  $\gamma_p = 150 \text{ cm}^{-1}$  and  $\epsilon_{s,\infty} = 5$ ), a strong Lorentz oscillator ( $A_{ph} = 1,200 \text{ cm}^{-1}$ ,  $\omega_{ph} = 1,000 \text{ cm}^{-1}$  and  $\gamma_{ph} = 60 \text{ cm}^{-1}$ ) and a weak Lorentz oscillator ( $A_m = 500 \text{ cm}^{-1}$ ,  $\omega_m = 1,800 \text{ cm}^{-1}$  and  $\gamma_m = 30 \text{ cm}^{-1}$ ). It is used for calculating the near-field spectra shown in panels **c** and **d**. **c**, Calculated near-field amplitude and phase spectra,  $s_3(\omega)$  and  $\varphi_3(\omega)$ , of a semi-infinite bulk sample (normalized to a bulk Au sample) described by the dielectric function of panel **b**. We use the finite dipole model<sup>31</sup>, assuming a tip with semi-major axis length of 350 nm, apex radius of 20 nm, tapping amplitude of 50 nm, model parameter  $g = 0.7e^{i0.06}$ , and that far-field reflection at the sample and reference are the same. **d**, Normal incidence far-field reflectance spectrum  $R_s(\omega)$  and absorption coefficient  $\kappa_s(\omega)$  of a sample described by  $\epsilon_s(\omega)$  of panel **b**.  $R$  is calculated for a semi-infinite sample using the standard Fresnel reflection equation. Shaded areas mark the frequency ranges between near-field amplitude and phase peaks. **e**, Scattering-type scanning near-field optical microscopy (s-SNOM) amplitude (black circles) and phase (red circles) spectra taken on PMMA, normalized to a spectrum obtained on PS. The solid lines represent Lorentzian fits. The dotted

lines show the refractive index ( $n_s$ , black) and absorption coefficient ( $\kappa_s$ , red) of PMMA. The inset shows an s-SNOM image ( $1,735 \text{ cm}^{-1}$ ) of the PMMA–PS block copolymer (blue and yellow regions, respectively). **f**, Nanoscale Fourier transform infrared (nano-FTIR) spectroscopy amplitude (blue) and phase (red) spectra of an  $\text{SiO}_2$  disk normalized to the Si substrate. The inset shows an s-SNOM image of the  $\text{SiO}_2$  disk at  $1,130 \text{ cm}^{-1}$ . The zoomed-in spectra compare experimental spectra with calculated near-field spectra (black), highlighting the near-field-induced  $\text{SiO}_2$  surface phonon polariton resonance. **g**, Normalized experimental (symbols) and theoretical (lines) amplitude and phase spectra of a single InP nanowire taken at positions with different carrier concentrations, marked on the s-SNOM image at  $893 \text{ cm}^{-1}$ . The grey curves are calculated spectra, which reveal that a 50% change in free-carrier concentration can cause significant spectral changes, resulting in spectral shifts of several  $100 \text{ cm}^{-1}$ . The numbers indicated next to the amplitude spectra represent the free-carrier concentration used for the calculations. PE, polyethylene; PMMA, polymethyl methacrylate; PS, polystyrene. Panel **e** adapted from ref. 38, Springer Nature Limited. Panel **f** adapted with permission from ref. 39, PNAS. Panel **g** adapted with permission from ref. 35, American Chemical Society.

in spectroscopic s-SNOM data, we constructed an artificial dielectric function using the Drude–Lorentz model, which incorporates both the Drude terms and Lorentz oscillators described earlier (Fig. 5b).

In Fig. 5c, we present the calculated near-field amplitude and phase spectra,  $s_3(\omega)$  and  $\varphi_3(\omega)$ , of a corresponding semi-infinite isotropic bulk sample. To appreciate similarities and differences compared with typical far-field spectra, we show in Fig. 5d the calculated normal incidence far-field reflectance spectrum,  $R_s(\omega)$ , of the semi-infinite bulk sample and the absorption coefficient  $\kappa_s(\omega)$ , which is the imaginary part of the complex-valued refractive index  $\tilde{n}_s = n_s + i\kappa_s = \sqrt{\epsilon_s}$ . We show  $\kappa_s$ , because the absorbance  $A_s \propto \kappa_s d$  scales linearly with  $\kappa_s$  but diverges for semi-infinite samples of infinite thickness  $d$ .

## Weak oscillator samples

For weak oscillators (Fig. 5c,d, blue-shaded area),  $s_3(\omega)$  compares qualitatively well to  $\text{Re}[\epsilon_s(\omega)]$  and  $R_s(\omega)$ , whereas  $\varphi_3(\omega)$  resembles  $\text{Im}[\epsilon_s(\omega)]$  and  $\kappa_s(\omega)$  (refs. 38,43,69,74,113,190). For this reason, near-field phase spectra of molecular vibrations can be compared with far-field absorbance spectra from databases for chemical identification, without the need for modelling<sup>44,54,191,192</sup>. As an example, we show in Fig. 5e s-SNOM amplitude and phase spectra taken for a nanoscale region of PMMA of a PMMA–PS block copolymer sample<sup>38</sup>. The experimental s-SNOM amplitude and phase spectra (open circles) and their fit by a Lorentzian oscillator (solid lines) agree well with  $n_s(\omega)$  and  $\kappa_s(\omega)$  obtained from ellipsometry (dashed lines). Owing to the near-field interaction between tip and sample, however, small deviations between near-field and far-field spectra exist<sup>43,54,74</sup>. For example, for thin layers, the height and spectral position of amplitude and phase peaks depend on the layer thickness and the dielectric function of the substrate<sup>51,54,70,193</sup>, which necessitates the modelling of s-SNOM spectra (see the next section) when an accurate quantitative analysis of the local oscillator resonances is required. We note that  $a_n = \text{Im}[\sigma_n]$ , referred to as nano-FTIR absorption, has been introduced as an alternative for comparing near-field with far-field spectra<sup>44,190</sup>, since the peak positions in nano-FTIR absorption spectra of samples thicker than the near-field probing depth correspond to those in far-field absorbance spectra obtained by transmission FTIR spectroscopy.

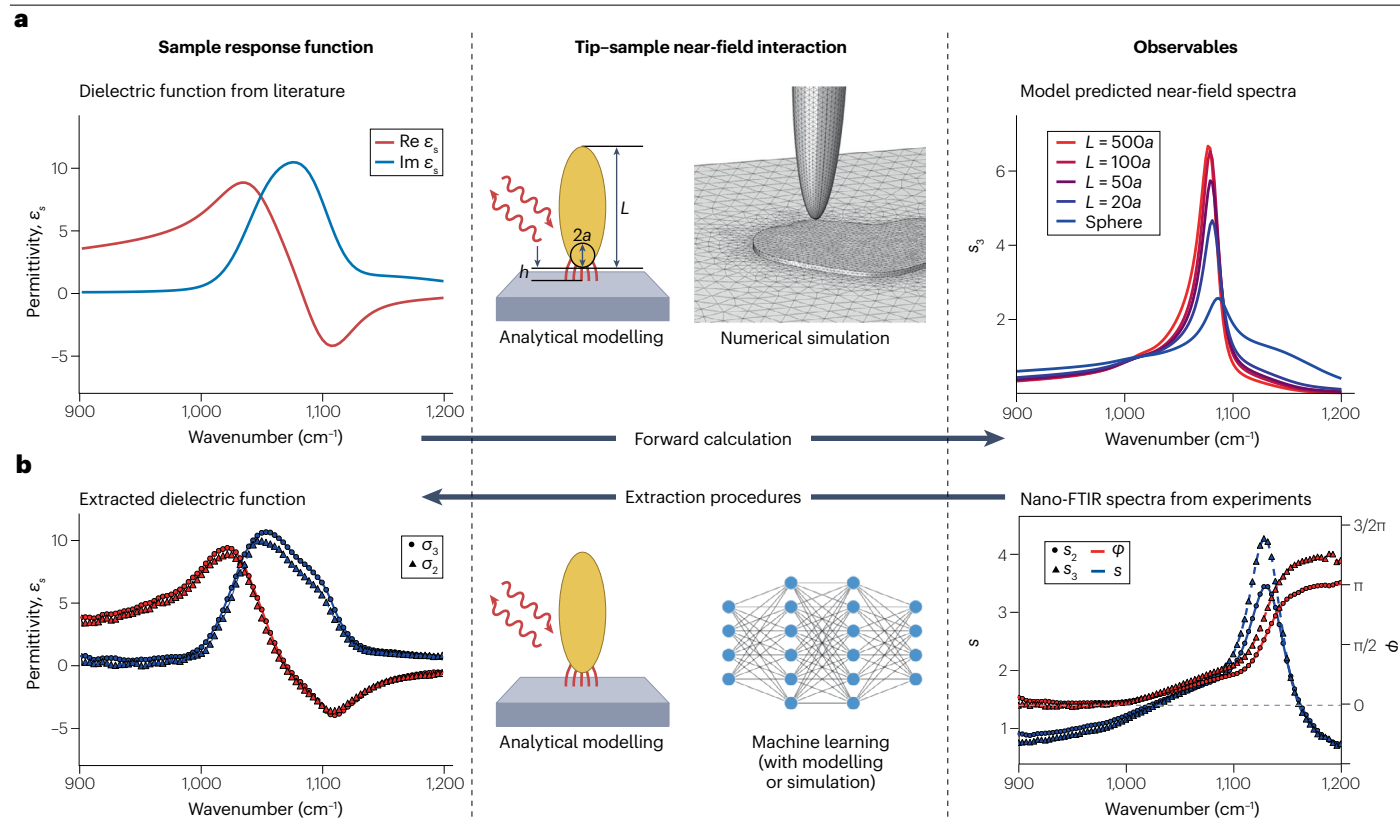
## Strong oscillator samples

In stark contrast to weak oscillators, we find a significantly different behaviour of near-field spectra when strong Lorentz oscillators

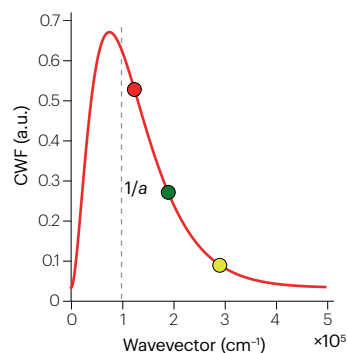
or Drude materials are probed, or more generally, when  $\text{Re}[\epsilon_s(\omega)]$  assumes negative values (Fig. 5b, yellow-shaded and red-shaded areas). The peaks observed in the  $s_3(\omega)$  and  $\varphi_3(\omega)$  spectra are significantly blue-shifted compared with those of  $\text{Re}[\epsilon_s(\omega)]$  and  $\text{Im}[\epsilon_s(\omega)]$ . Moreover, the near-field spectra do not match far-field spectra, where regions with  $\text{Re}[\epsilon_s(\omega)] < 0$  give rise to broad spectral reflection and absorption features known as Reststrahlen bands. Remarkably, the near-field amplitude signals can exceed that of a gold sample, such that  $s_3(\omega) > 1$ . This intriguing phenomenon can be explained by the near-field reflection coefficient (that is, Fresnel reflection coefficient at momenta much larger than that of the free-space photon), which in the electrostatic limit is given by  $\beta_s = (\epsilon_s - 1)/(\epsilon_s + 1)$  (ref. 45). The divergence of  $\beta_s$  near  $\epsilon_s = -1$  yields an exceptionally strong reflection of the tip's near field at the sample surface and subsequently a strong near-field interaction and scattering. The physical origin of this divergence can be attributed to a resonant near-field excitation of localized SPPs in the Drude material<sup>135,78,90,194–196</sup> and localized surface phonon polaritons (SPhPs) in the strong Lorentz oscillator sample<sup>37,39,45,104,197,198</sup>. Importantly, the near fields at the tip apex may excite propagating SPPs and SPhPs when  $\epsilon_s < -1$ , leading to polariton interference fringes near sample edges<sup>142,143,168,172,199</sup> (Fig. 4b,c). Although the appearance of these fringes provides valuable information about the polaritons, they may disturb the pure material contrast and need to be considered when the local dielectric function is to be determined.

## Phononic strong oscillator samples

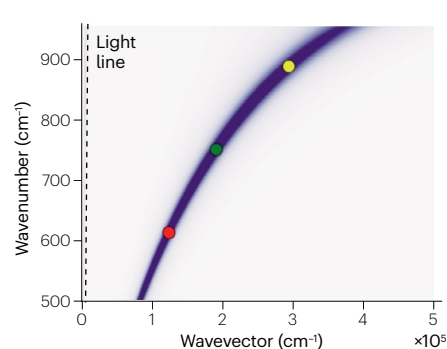
In Fig. 5f, we show the measured nano-FTIR spectrum of  $\text{SiO}_2$ , a typical example of a sample in which an SPhP-resonant near-field interaction leads to exceptionally strong and narrow peaks in both near-field amplitude and phase spectra<sup>39</sup>. We also observe a significant blue shift of the amplitude peak ( $1,130 \text{ cm}^{-1}$ ) relative to the transverse optical phonon of  $\text{SiO}_2$  ( $1,074 \text{ cm}^{-1}$ ), analogue to the calculated near-field spectrum of the artificial strong phonon oscillator in Fig. 5b–d. Generally, the spectrally sharp and strong phonon polariton peak allows for highly sensitive characterization of the local chemical composition of polar crystals. Examples include the identification of calcite and phosphate bands in biominerals and human teeth<sup>200</sup>, as well as of minerals in meteorites and cometary dust grains<sup>201</sup>. Structural properties can be mapped as well, as the optical phonon frequencies are highly sensitive to the crystal lattice parameters and thus to polytypes<sup>202</sup>, crystal quality and



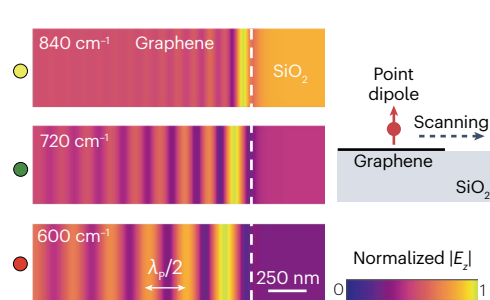
## c Coupling weight function



## d Plasmon dispersion



## e Simulated real-space images



defects<sup>153,203</sup> and strain<sup>204,205</sup>. In the presence of mobile charge carriers in doped semiconductors or heterostructures, carrier-phonon coupling can modify the spectral position and width of the SPP-phonon resonant near-field interaction, allowing for sensitive local measurements of low carrier concentrations<sup>156,197,202,206,207</sup>.

## Plasmonic strong oscillator samples

Figure 5g illustrates an example of an SPP-resonant near-field interaction, showing both calculated (lines) and measured (symbols) near-field amplitude and phase spectra of an InP nanowire<sup>35</sup>. The bright and dark areas in the near-field amplitude image correspond to doped and undoped regions. The peaks in the amplitude and phase spectra of the doped area (red) stem from the SPP-resonant near-field interaction.

Their position strongly depends on the mobile carrier concentration  $n$ . Generally, via modelling of the near-field spectra (see the next section),  $n$  can be quantified with nanoscale spatial resolution not only in semiconductor nanowires but also in doped wafers, organic semiconductors and nanoelectronic devices<sup>78,90,121,196,208</sup>.

## Remarks

The interpretation of polariton resonances in near-field spectra of strong oscillators requires a careful analysis by modelling, as a direct comparison with far-field spectra from databases is typically not possible. Furthermore, the description of the near-field optical material contrasts given in this section and in Fig. 5 is valid for isotropic bulk materials and, generally, cannot be directly applied to anisotropic



**Fig. 6 | Analysing near-field optical data by analytical modelling, numerical simulations and data-driven machine learning.** **a**, Forward calculations. Real (red) and imaginary (blue) parts of the dielectric functions of SiO<sub>2</sub> (left). Methods for the forward calculation of experimental near-field data are based on known sample response functions, such as permittivity, and can use analytical models (point dipole model<sup>10,15,16,45</sup>, finite-dipole model<sup>31,70,74,209</sup> – left side of the middle panel – or lightning-rod model<sup>198</sup>), or numerical simulations (such as finite element method, method of moments – right side of the middle panel – and so on). Near-field amplitude spectra of a 300 nm thick SiO<sub>2</sub> film on an Si substrate calculated with the lightning-rod model using different tip shank lengths  $L$ .  $a$  is the tip radius (right). **b**, Backward calculations. SiO<sub>2</sub> dielectric function (left) extracted from the experimental amplitude and phase spectra,  $s_n(\omega)$  and  $\varphi_n(\omega)$ , of a 300 nm SiO<sub>2</sub> film on an Si substrate for  $n = 2$  and 3 (right). The extraction was performed using the lightning-rod model<sup>209</sup>. Methods for the backward extraction of the sample response function from experimental near-field data using analytical modelling or machine learning (such as neural networks) are shown in the middle panel. **c**, Time-averaged coupling weight function (CWF)

for a tip with  $a = 100$  nm radius, modelled as a point dipole, oscillating with an amplitude of  $A = 50$  nm. **d**, Calculated imaginary part of the Fresnel reflection coefficient  $r_p$  for graphene (Fermi energy  $\mu_i = 2,500$  cm<sup>-1</sup>, scattering rate  $\gamma = 10$  cm<sup>-1</sup> and temperature  $T = 300$  K) on SiO<sub>2</sub>, revealing the graphene plasmon polariton dispersion. **e**, Simulated images at 600, 720 and 840 cm<sup>-1</sup> (marked by red, green and yellow dots in panels **c** and **d**), normalized to the maximum of the first fringe below the graphene edge (dashed white line). They were obtained by scanning a point dipole at a 150 nm height across graphene (as shown in the schematic) and plotting the norm of the vertical electric field component 100 nm below the dipole as a function of the lateral dipole position. The fringes reveal graphene plasmons, launched by the dipole and reflected at the graphene edge, analogue to the experiment described in Fig. 4b. Consequently, the fringe spacing corresponds to half the plasmon wavelength,  $\lambda_p/2$ . With increasing wavenumber,  $\lambda_p$  decreases, revealing in real space the plasmon dispersion shown in panel **d**. FTIR, Fourier transform infrared (spectroscopy). Panels **a** and **b** adapted with permission from ref. 198, APS.

materials. For example, the tip-induced SPP and SPhP resonances are not observed on uniaxial materials with optical axis perpendicular to the surface, where the amplitude peak occurs near the transverse optical frequency<sup>140,144</sup>. This finding may be explained by the fact that the polaritons in such materials are volume polaritons rather than surface polaritons.

## Modelling of near-field images and spectra

Permittivity determination is well established in far-field optics using techniques such as ellipsometry and FTIR spectroscopy, but it remains challenging in s-SNOM and nano-FTIR spectroscopy. Efforts to model near-field interactions in s-SNOM have been ongoing since the early 2000s<sup>10,15,16,45</sup>, following the original dipole model of apertureless SNOM<sup>9</sup>. The complex tip-sample near-field interaction and irregular probe and sample geometries make it difficult to establish an accurate mathematical relationship between the local permittivity of the sample,  $\epsilon_s$ , and experimentally measured near-field signals  $\sigma_n$  (equation (1)). Consequently, simplifications and approximations are necessary for simulating s-SNOM and nano-FTIR data using known or assumed sample dielectric functions. The role of approximations becomes increasingly pertinent when attempting to reconstruct the dielectric function from near-field data – a notably challenging task that is still in rather early stages of development.

## Modelling of material contrasts

In a rudimentary analytical approach, the AFM tip is modelled as a point dipole located inside the tip apex. The near-field interaction between this dipole and a semi-infinite sample can be described using the quasistatic approximation<sup>10,15,16</sup>, which yields an effective dipole polarizability  $\alpha_{\text{eff}}(\epsilon_s, h)$  that depends on the permittivity  $\epsilon_s$  of the region of interest of the sample and the tip-sample distance  $h$ . When far-field reflections at the sample surface are negligible, the scattering coefficient (see the section ‘Near-field signal detection and normalization’) can be expressed as  $\sigma_s \propto \alpha_{\text{eff}}(\epsilon_s, h)$ . By considering a sinusoidal tip oscillation,  $h = h(t)$ , one obtains  $\alpha_{\text{eff}}(\epsilon_s, t)$ , whose Fourier decomposition yields the Fourier coefficients  $\alpha_{\text{eff},n}(\epsilon_s)$ . By normalizing these Fourier coefficients to those of a reference sample, one obtains  $\sigma_n = \alpha_{\text{eff},n}(\epsilon_s)/\alpha_{\text{eff},n}(\epsilon_{\text{ref}})$ . This ratio allows for a direct comparison with normalized experimental near-field signals (equation (1)). Later, this point dipole model (PDM) was expanded by fully retarded calculations for layered samples<sup>48</sup>. Although the PDM omits the elongated tip shank,

whose length is often comparable to or larger than the wavelength of visible or IR illumination, it can qualitatively describe the experimentally observed near-field material contrasts for all three types of sample excitations<sup>10,45,46,194,196</sup> described in Fig. 5. The PDM, however, fails to quantitatively describe material contrasts when polariton-resonant tip-sample near-field interactions occur<sup>45</sup>, such as the ones described in Fig. 5f,g. For example, the model does not correctly describe the position, width and magnitude of the spectral peaks<sup>31</sup>. For improved quantitative modelling, more sophisticated models beyond the PDM were thus developed, such as the finite-dipole model (FDM) for bulk samples<sup>31</sup>. The FDM phenomenologically approximates the tip by a spheroid with several point charges placed along its major axis, yielding a more accurate expression of the effective tip polarizability. This model agrees well with experimental material contrasts and is widely used. Several extensions of the FDM were made for layered samples<sup>70,74,209</sup>. We note that the dipole models are inherently simple but involve various parameters that are often insufficiently described in the literature. To facilitate the use of these models, clarify their parameters and ensure consistency, a Python package with a detailed discussion of these parameters has been developed<sup>210</sup>. More rigorous, although complicated, approaches to modelling near-field contrasts can be achieved through theoretical and numerical calculations that treat the tip as an elongated spheroid<sup>198,211</sup> or cone<sup>30,61,68,212,213</sup> (Fig. 6a, middle).

## Reconstruction of sample properties by inversion of normalized near-field signals

Several of the s-SNOM models can be inverted and have been applied to determine the local sample properties from s-SNOM and nano-FTIR data. The accuracy and consistency of the reconstructions can be tested with well-known sample materials. To this end, the permittivity results obtained from the inversion of normalized near-field amplitude and phase data,  $s_n(\omega)$  and  $\varphi_n(\omega)$ , for different signal demodulation orders  $n$  or tip-oscillation amplitudes (Fig. 3) should be consistent and should match literature data. Reconstruction of the dielectric function of thin layers of the well-known polymer PMMA<sup>43,74</sup> and SiO<sub>2</sub> (ref. 198) were successfully demonstrated with the FDM<sup>74</sup> and the lightning-rod model (LRM)<sup>198,211</sup>, respectively. The LRM rigorously accounts for the electromagnetic interaction between the tip and the sample and can accommodate arbitrary tip geometries, diverse sample configurations and electrodynamic effects. The LRM was later applied to measure mid-IR

in-plane and out-of-plane permittivities of the van der Waals material 2H-WSe<sub>2</sub> (ref. 214). The reconstruction of the permittivity of complex multilayer materials has been achieved using the FDM for layered samples, for example, of topological insulators at THz (refs. 78,105) and mid-IR frequencies<sup>76</sup>. In the latter study, the reconstructed permittivity revealed an intersubband transition within the massive 2D electron gas, whereas an additional broadband absorption background potentially indicated the presence of a topological surface state. By contrast, these models have not been extensively verified with well-known materials in terms of their capability to fit experimental near-field data at several  $n$  simultaneously.

## Modelling and reconstruction example

We now discuss an example of modelling s-SNOM material contrasts<sup>198</sup>. The left panel of Fig. 6a depicts the mid-IR permittivity of SiO<sub>2</sub>. The IR-active phonon leads to the typical Lorentzian line shape. Using this permittivity, near-field amplitude and phase spectra of thin SiO<sub>2</sub> layers were calculated using the LRM<sup>198</sup> (middle panel). The right panel of Fig. 6a shows the third harmonic near-field amplitude spectra,  $s_3(\omega)$  of a 300 nm-thick SiO<sub>2</sub> film on an Si substrate for different tip lengths. The results show that the spectral peak position and height of the near-field phonon polariton resonance are sensitive to the tip length, likely due to the lightning-rod effect. For comparison, the right panel of Fig. 6b shows the experimentally measured second and third harmonic near-field amplitude and phase spectra,  $s_n(\omega)$  and  $\varphi_n(\omega)$ , of a 300 nm SiO<sub>2</sub> film on Si substrate, showing good agreement with the lightning-rod model calculations.

The left panel of Fig. 6b shows the dielectric function of SiO<sub>2</sub> as reconstructed from the experimental s-SNOM via the LRM. In this optimization problem, a continuous path  $\varepsilon_s(\omega)$  in the complex  $\varepsilon$  space is systematically varied, such that the near-field signal calculated from  $\varepsilon_s(\omega)$  matches the experimental complex-valued nano-FTIR spectra  $\sigma_n(\omega)$  the best. Additional numerical techniques can be applied to enhance the robustness of the inversion and ensure the uniqueness and smoothness of  $\varepsilon_s(\omega)$  (ref. 198). The results shown in the left panel of Fig. 6b are the best estimation of the sample permittivity. It matches well the permittivity obtained from far-field ellipsometry measurements (Fig. 6a, left).

## Modelling and simulation of images resulting from tip-launched polaritons

Modelling does not only allow for describing s-SNOM material contrasts but also provides basic insights into the various other probing mechanisms described in Fig. 4. For instance, it is well established that the momentum distribution of the near-field interaction within the PDM follows a coupling weight function of  $q^2 e^{-2qz}$  (Fig. 6c), in which  $q$  is the in-plane momentum and  $z = a + h(t)$  the distance between the dipole and the sample surface<sup>48,107,209</sup>. Although the tip height  $h$  and, consequently, the weight function vary over time, the dominant momenta in the near-field interaction, where the weight function peaks, are around  $1/a$ , with  $a$  being the tip radius. These momenta are sufficiently large to match those of ultra-confined polaritons, as illustrated in Fig. 6d, in which we show an example dispersion for mid-IR graphene plasmons. This explains why the near fields at the tip apex can effectively launch ultra-confined polaritons in 2D materials<sup>28,107,135,136</sup> (Fig. 4b–d). The experimental near-field images of these modes can be thus well reproduced by modelling the tip as a point-dipole source or finite dipole and plotting the near field of the dipole as a function of position<sup>150,154,155</sup> (Fig. 6e). Beyond the verification of experimental polariton images, fitting of the experimental data allows for extracting

polariton properties and related material properties on complex samples<sup>103,144,213</sup>, such as conductivity variations around graphene grain boundaries<sup>154</sup>. Furthermore, it is possible to identify and disentangle individual plasmonic and phononic eigenmodes from the complex interference patterns observed in s-SNOM images of graphene (Fig. 4c) and h-BN nanoresonators<sup>150,161</sup>.

## Advanced numerical simulations

Despite significant advancements, the analytical modelling of material contrasts continues to be encumbered by certain limitations. For instance, analytical models typically require the sample to be flat and homogeneous, a condition that frequently deviates from experimental reality. By contrast, full numerical simulations offer a viable platform for examining the intricate interplay between light, finite-size probes and laterally heterogeneous samples<sup>61,213,215,216</sup> (Fig. 6a, middle). Moreover, it has been shown that simulating the actual tip geometry based on scanning electron micrographs, even incorporating the cantilever, is computationally feasible<sup>217</sup>.

Although numerical simulations can accurately account for tip and sample geometries, they are computationally intensive and therefore are difficult to use for backward extraction of the sample properties using experimental data. A predominantly data-driven approach utilizing machine learning has recently been demonstrated as another feasible backward extraction method<sup>218–220</sup> (Fig. 6b, middle). In this approach, a neural network can link sample permittivity with near-field data from experimental or simulated data sets. With the increasing availability of near-field instruments, a large amount of data is generated daily. Applying advanced machine learning and other AI techniques to big data has the potential to unveil valuable insights and uncover complex physics.

## s-SNOM with distinct sample environments

s-SNOM exhibits great versatility in its ability to operate in a broad range of environmental conditions (Fig. 7).

### Elevated temperatures

s-SNOM-based nanoimaging and spectroscopy can be performed at elevated temperatures up to 400 K (refs. 131,221–226), via either a heating stage or laser illumination (Fig. 7a). This enables, for example, studies of phase transitions, as demonstrated in Fig. 7b, in which nanoscale-resolved IR imaging reveals the coexistence of metallic (white) and insulating (blue) stripes in a vanadium dioxide microbeam at -345 K (ref. 223). Similar reversible phase transitions in VO<sub>2</sub> thin films can be triggered by increasing the incident light power to 10–20 mW using a pulsed IR laser, heating the entire illuminated region<sup>224</sup>. Laser heating has also been employed to induce irreversible changes of sample properties, which can be conveniently probed through consecutive s-SNOM imaging. Figure 7c shows that local heating through enhanced optical near fields below the tip apex can be utilized for nanolithography of proteins. The top image shows the heat-induced local topography change in a silk film, which is accompanied by an increased local IR absorption (bottom image), revealing a conformational change of the silk protein<sup>227</sup>.

### Cryogenic temperatures

Cryogenic s-SNOM (cryo-SNOM) is an essential tool for studying materials at low temperatures, offering unique insights into phenomena that are not accessible at ambient conditions (Fig. 7d). Typically, cryo-SNOM systems incorporate a sample-scanning AFM coupled to a motorized focusing mirror housed in a high vacuum, or preferably, ultra-high

vacuum chamber equipped with anti-vibration stages<sup>169</sup>. They operate using either continuous flow<sup>169</sup> or closed-cycle cryo-systems<sup>228</sup>, reaching sample temperatures below 20 K (refs. 169,228–232). Recent advancements in cryo-SNOM have led to the development of various types of tabletop systems and expanded their application to large-scale beamline facilities such as tunable free-electron lasers<sup>231</sup>. Conducting nano-imaging and nano-spectroscopy at cryogenic temperatures has facilitated the study of quantum phase transitions in correlated electron materials<sup>229,233</sup>, 2D electron gases at oxide interfaces<sup>228</sup> and the reduced damping of polaritons at low temperatures<sup>169,234,235</sup>.

For example, Fig. 7e shows the nanotextured phase separation in a  $V_2O_3$  thin film that is revealed during the metal-to-insulator transition at 169 K (ref. 226). The bi-directional ‘tweed’ texture of the metallic (red areas) and insulating (blue areas) states demonstrates a substrate-strain-induced symmetry breaking of  $V_2O_3$  thin films during the transition. Figure 7f shows that at cryogenic temperature down to 60 K, the propagation distance of plasmon polaritons in graphene is greatly extended compared with room temperature, exceeding 10  $\mu\text{m}$ , or 50 plasmonic wavelengths<sup>169</sup>.

Future developments in cryo-SNOM may include minimizing cryogen usage in ultra-high vacuum environments while managing sample vibration, surface icing and optimizing tip control for best AFM performance. Additionally, improving the S/N ratio of interferometric measurements without excessive laser heating will require innovative solutions for detection optics. For instance, employing a parabolic mirror with a high numerical aperture in combination with an in-chamber reference arm can effectively mitigate the noises generated in the different paths of the asymmetric interferometer by mechanical vibrations owing to the cryogen flow.

## Ultrafast optical excitation

s-SNOM experiments can also be performed in an ultrafast pump–probe scheme, combining high spatial, temporal and energy resolution<sup>78,195</sup>. As illustrated in Fig. 7g, a fs-pump pulse (blue sine wave) is focused onto the tip and photoexcites the sample in the vicinity of the tip. Subsequently, a fs-probe pulse (red sine wave) is focused onto the tip with a controlled time delay relative to the pump pulse. Detecting the tip-scattered probe pulse by either nano-FTIR spectroscopy<sup>195,236–238</sup> or electrooptic sampling<sup>78,239</sup> combined with higher-harmonic signal demodulation as a function of the time delay  $t_{pp}$  between the probe and pump pulses allows for ultrafast time-resolved near-field measurements of the transiently altered local sample properties. So far, mostly visible-to-near-IR pulses have been used for pumping, whereas probing has been typically performed with IR<sup>78,195,223,236,237,240</sup> and THz (refs. 241–243) pulses, and in few cases with visible<sup>244</sup> pulses. The technique has been applied for studying photoinduced metal–insulator phase transitions<sup>236,240,245,246</sup>, ultrafast carrier dynamics in semiconductors and graphene<sup>78,195,239,247,248</sup> and for the ultrafast control of plasmon and phonon polariton propagation<sup>244,249–252</sup>. In these studies, the pump pulses mostly triggered electronic interband and intraband transitions or heating.

For instance, the ultrafast dynamics of a photoexcited InAs semiconductor nanowire was investigated using 1.56  $\mu\text{m}$  pump and -10  $\mu\text{m}$  probe pulses<sup>78</sup>. Figure 7h shows the IR near-field images at a delay time of -2 ps (before excitation) and +50 fs (after excitation). The increased near-field signal at +50 fs stems from the increased carrier density after photoexcitation. Analysing the transient near-field spectra as a function of the time delay revealed the ultrafast carrier dynamics, including the ultrafast formation of a depletion layer. In another example<sup>249</sup>,

near-IR pulses were used to generate transient electron–hole pairs in a thin  $\text{WSe}_2$  flake, and nano-FTIR spectroscopy was employed to visualize the resulting hyperbolic polariton rays travelling inside the crystal along conical trajectories (Fig. 7i). The transient polaritons manifest as circular features in the near-field image at  $t_{pp} = +2$  ps after pumping due to the excessive exciton pairs induced by the pump excitation. In the future, IR/THz pumping and visible/IR probing could be promising variations for optical doping at the technologically important low photon energy range<sup>253</sup>.

## Electric and magnetic fields

s-SNOM can also address field or current switching (Fig. 7j). Electric switching can be induced through predeposited electrodes on the sample surface, by applying either an electric field or current. For example, it was observed that the plasmon wavelength in graphene depends on the direction of the applied electric current. This phenomenon is related to the nonlinear electrodynamics of Dirac electrons in graphene and is known as the ‘Fizeau drag’<sup>254,255</sup> (Fig. 7k). It was also shown that electric currents can induce an insulator–metal phase transition in the 4d transition metal oxide  $\text{Ca}_2\text{RuO}_4$ , as can be recognized by clear phase boundaries between metallic and insulating states<sup>256</sup>.

The recent introduction of s-SNOM operating under high magnetic fields (also known as m-SNOM), reaching up to 7 T, has the potential to map nanoscale phenomena associated with the breaking of time-reversal symmetry. Still in its early stages, the m-SNOM setup integrates a strong magnet, often a superconducting one, with a cryogenic system to ensure a stable temperature and magnetic field environment<sup>232,257</sup>. Owing to the small bore size of the superconducting magnet, the system usually requires a miniaturized AFM and compact optics to accommodate everything within a limited space<sup>257</sup>.

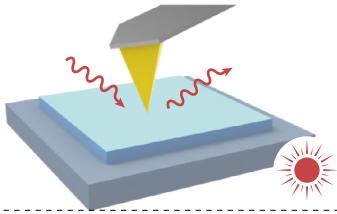
The development of m-SNOM opens up exciting possibilities for exploring correlated electron systems and low-dimensional materials under magnetic excitations. One promising application is nanoscale Landau level spectroscopy, in which the presence of Landau levels modifies the optical conductivity, revealing the magneto-optical properties of the material at the nanoscale. At IR frequencies, this provides valuable insights into controlling polaritonic excitations and allows for uncovering many-body physics related to Landau level excitations in graphene<sup>257</sup> (Fig. 7l). In the THz frequency range, magneto-nanoscopy could be used for investigating magnetic excitations, charge order dynamics and quasiparticle energy gaps in phase-separated microcrystals, in which the energy scale aligns with low-energy photons. One preliminary example demonstrates the potential of THz s-SNOM operating at ultra-low temperatures and magnetic fields up to 5 T were used to detect magnetic field-induced electromagnetic responses in superconductors and Weyl semimetals<sup>232</sup>.

## Strain

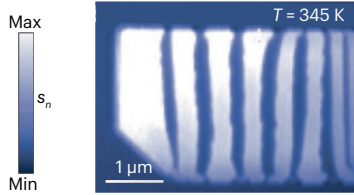
s-SNOM can be also applied for the mapping of strain and strain-induced physical and chemical properties, either ex situ (Fig. 7m) or in situ<sup>52,153,160,204,205,258</sup>. The strain field can be applied through epitaxial strain<sup>226</sup>, nanoindentation<sup>204,205</sup> or dynamically tuned using piezo strain stages<sup>52</sup>. For example, strain was created in an SiC crystal by nanoindentation before s-SNOM imaging. By using an IR wavelength near the optical phonon frequencies of SiC, it was possible to highlight compressive and tensile strain (bright and dark areas) due to strain-induced spectral phonon shifts<sup>204</sup> (Fig. 7n). Compressive and tensile strain can be also applied while the sample is imaged, for example, by bending or stretching the sample employing piezoelectric actuators. The latter



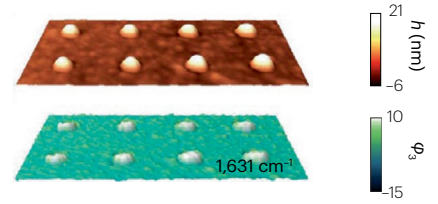
## a Elevated temperature



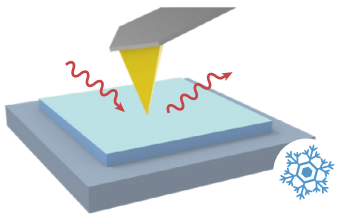
## b $\text{VO}_2$



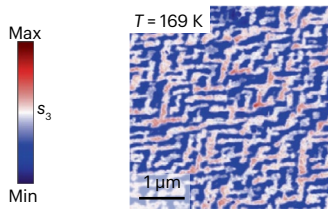
## c Silk



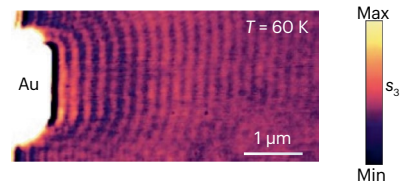
## d Cryogenic temperature



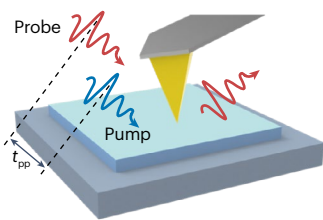
## e $\text{V}_2\text{O}_3$



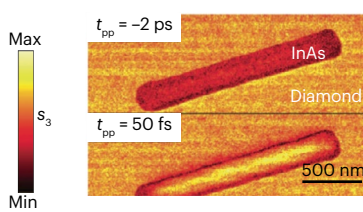
## f Graphene



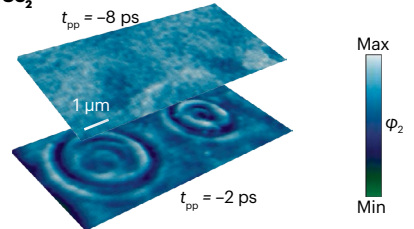
## g Optical excitation



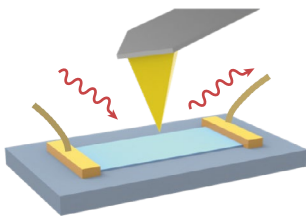
## h InAs



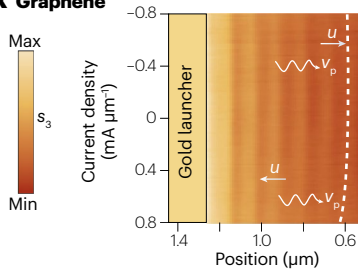
## i $\text{WSe}_2$



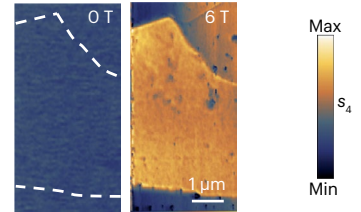
## j Electric or magnetic field, current



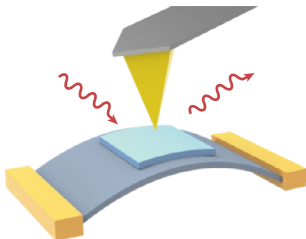
## k Graphene



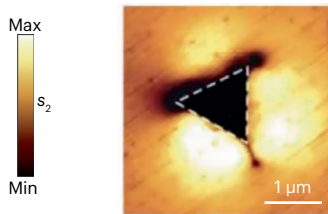
## l Graphene



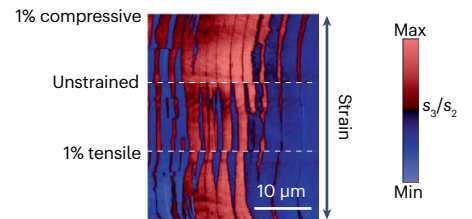
## m Strain



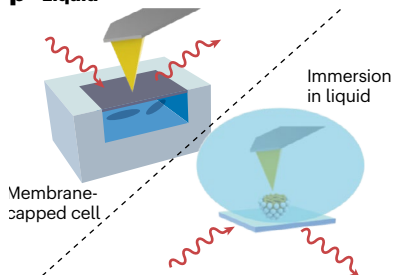
## n SiC



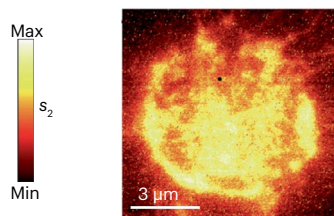
## o $\text{Ca}_3(\text{Ti}_{0.1}\text{Ru}_{0.9})_2\text{O}_7$



## p Liquid



## q Living cancer cells



## r Biomembranes

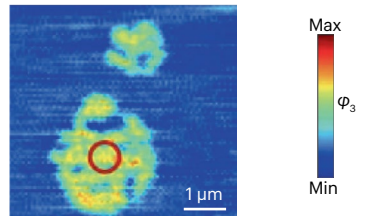




## Fig. 7 | Scattering-type scanning near-field optical microscopy setup with distinct sample environments.

**a**, Schematic illustration of a setup for measurements at elevated temperatures. **b**, Infrared ( $926\text{ cm}^{-1}$ ) image of a  $\text{VO}_2$  microcrystal at 345 K, showing metallic (white) and insulating (blue) domains. **c**, Heating through the near fields at the tip apex. The topography of a silk layer with heat-induced protrusions (top) is shown together with an infrared ( $1,631\text{ cm}^{-1}$ ) phase image showing stronger infrared absorption at the protrusions. **d**, Schematic illustration of a setup for measurements at cryogenic temperatures. **e**, Infrared ( $920\text{ cm}^{-1}$ ) amplitude image of a  $\text{V}_2\text{O}_3$  film at 169 K, showing metallic (red) and insulating (blue) domains. **f**, Infrared ( $886\text{ cm}^{-1}$ ) amplitude image of long-lived plasmons on back-gated graphene at 60 K. **g**, Schematic illustration of a setup for ultrafast pump–probe nano-spectroscopy.  $t_{\text{pp}}$ , time delay between pump and probe pulses. **h**, Infrared ( $2,000\text{ cm}^{-1}$ ) amplitude images of an InAs nanowire recorded for different pump–probe delay times. At  $t_{\text{pp}} = +50\text{ fs}$ , the nanowire appears brighter due to pump-induced mobile charge carriers. **i**, Time-resolved infrared ( $910\text{ cm}^{-1}$ ) near-field phase images of a  $\text{WSe}_2$  slab on top of a metal disk. At  $t_{\text{pp}} = +2\text{ ps}$ , circular fringes reveal pump-induced hyperbolic Rydberg polaritons in  $\text{WSe}_2$ . **j**, Schematic illustration of a setup for measurements with electric or magnetic fields. **k**, Infrared amplitude ( $890\text{ cm}^{-1}$ ) signal of graphene as a function of position relative to gold launcher and current density, showing that the plasmon wavelength (horizontal fringe periodicity) varies with current density, as indicated by the white dotted line ('Fizeau drag'). The arrows labelled  $u_p$  indicate

the direction of plasmon propagation, the arrows labelled  $u$  the direction of the electron flow. **l**, Infrared ( $900\text{ cm}^{-1}$ ) amplitude images of graphene (outlined by dashed lines) at 0 T and 7 T, revealing enhanced optical conductivity at 7 T owing to Landau level transitions. **m**, Schematic illustration of a setup for measuring while strain is applied. **n**, Infrared ( $937\text{ cm}^{-1}$ ) amplitude image of a nanoindent in an SiC crystal, revealing areas of tensile (dark) and compressive (bright) strain. **o**, Infrared ( $-1,000\text{ cm}^{-1}$ ) amplitude signal of a  $\text{Ca}_{n+1}\text{Ru}_n\text{O}_{3n+1}$  single crystal, showing the evolution of metallic (red) and insulating (blue) domains as strain is applied (vertical axis). **p**, Schematic illustration of a setup for measuring in liquid environments. **q**, Broadband infrared amplitude image of a living A549 cancer cell in water underneath a 10-nm SiN membrane. **r**, Infrared ( $1,660\text{ cm}^{-1}$ ) phase image of a native biomembrane (fragments of archaeon *Halobacterium salinarum*) immersed in a bulk aqueous solution. Panel **b** adapted from ref. 223, Springer Nature Limited. Panel **c** adapted from ref. 227, Springer Nature Limited. Panel **e** adapted from ref. 226, Springer Nature Limited. Panel **f** adapted from ref. 169, Springer Nature Limited. Panel **h** adapted from ref. 78, Springer Nature. Panel **i** adapted with permission from ref. 249, AAAS. Panel **k** adapted from ref. 254, Springer Nature Limited. Panel **l** adapted from ref. 257, Springer Nature Limited. Panel **n** adapted from ref. 204, Springer Nature Limited. Panel **o** adapted from ref. 52, Springer Nature Limited. Panel **q** adapted with permission from ref. 51, Springer Nature Limited. Panel **r** adapted with permission from ref. 55, American Chemical Society.

method was applied to image the strain-induced anisotropic nucleation and growth of coexisting insulating (blue) and metallic (red) domains in single crystals of the bilayer ruthenate  $\text{Ca}_3(\text{Ti}_x\text{Ru}_{1-x})_2\text{O}_7$  across its first-order Mott transition at  $T \approx 95\text{ K}$  (ref. 52) (Fig. 7o). Future experiments might include the use of stretchable or bendable substrates to induce even larger strain for thin-film studies.

## Liquid and gaseous environments

For the study of biological samples or bio-chemical and electro-chemical reactions, it is often required that the sample is immersed in a liquid. To address this need, two different approaches have been developed (Fig. 7p). In the first approach, s-SNOM imaging of a wet sample is achieved by covering the biological object – a wet Tabaco mosaic virus in the first implementation – with graphene and scanning the graphene-covered object<sup>259</sup>. This method offers the advantage that neither the tip nor the IR beam needs to be immersed in the liquid, thus avoiding tip contamination and IR absorption by the liquid. The idea was further developed, leading to membrane-capped liquid cells (Fig. 7p) that allow for IR spectroscopic studies of biomolecules in water or buffer solution<sup>260,261</sup>, electrochemical processes in electrolytes<sup>262,263</sup> and even larger objects including living cells<sup>51,102,264</sup> (Fig. 7q) with nanoscale spatial resolution. In the second approach, both the sample and the tip are immersed in the liquid, analogous to typical AFM operation in liquids. To avoid IR absorption by the liquid, the tip is illuminated from below through an IR-transparent substrate<sup>55,265,266</sup> (Fig. 7p). The technique has been applied for chemical identification and structural analysis of biomembrane fragments of the archaeon *H. salinarum* (purple membrane)<sup>55</sup> (Fig. 7r), catalase nanocrystals and biomimetic peptoid sheets<sup>265</sup> as well as for studying the influence of water on the dispersion of phonon polaritons on hexagonal boron nitride<sup>266</sup>. When the sample has to be studied in inert gases, the whole s-SNOM setup can be placed into environmental chambers, including gloveboxes<sup>133,267,268</sup>.

## Applications

Several review articles discuss s-SNOM and nano-FTIR applications in soft matter and solid-state materials<sup>18,24</sup>, energy materials<sup>269</sup>,

corrosion<sup>270</sup> and biological sciences<sup>23,271,272</sup>. Here, we organize the applications into three categories: the mapping of material properties, the characterization of structures and devices and the study of phenomena.

## Mapping of local material properties

s-SNOM and nano-FTIR have been widely applied for the nanoscale mapping of the chemical composition of polymers<sup>38,46,73,123,192,273–276</sup>, biological matter such as proteins<sup>36,89,191,227,261,277,278</sup> and phospholipids<sup>279,280</sup>, biominerals<sup>200,281,282</sup> and inorganic crystals<sup>45,201,231,283</sup>. Furthermore, structural properties can be mapped, which allows for distinguishing crystallinity and crystal orientation<sup>95,202,203,274,284,285</sup>, strain<sup>160,204,205,233,258</sup> or the secondary structure of proteins and other macromolecules<sup>190,191,277,278,286,287</sup>. For materials such as semiconductors<sup>35,78,94,133,194–196</sup>, Mott insulators<sup>221,225</sup>, topological insulators<sup>76,105</sup> and perovskites<sup>236,268,288–292</sup>, one of the major applications is the discrimination between weakly insulating and highly conducting domains, as well as the quantitative mapping of the mobile carrier concentration and mobility.

For example, in block copolymer samples, the phase-separated components can be distinguished and identified based on their molecular vibrational fingerprint<sup>273</sup> (Fig. 8a). In  $\text{Li}_x\text{FePO}_4$  microcrystals, which are used in electrode materials for Li-ion batteries, IR s-SNOM images provide direct evidence of coexisting  $\text{LiFePO}_4$  and  $\text{FePO}_4$  phases<sup>293</sup> (Fig. 8b). This image highlights the remarkable potential of s-SNOM for characterizing electrochemical materials and interfaces. Furthermore, the secondary structure of proteins can be mapped at the level of single aggregates and fibres<sup>191</sup> (Fig. 8c), which is crucial for studying protein aggregation and amyloid fibrils related to neurodegenerative diseases.

## Characterization of structures and devices

Imaging and characterizing nanoscale structures are crucial for understanding their composition and function, optimizing their performance and advancing new technologies. s-SNOM and nano-FTIR have been applied to study the chemical composition and structural properties of various samples, including individual viruses<sup>36,191,294</sup>,

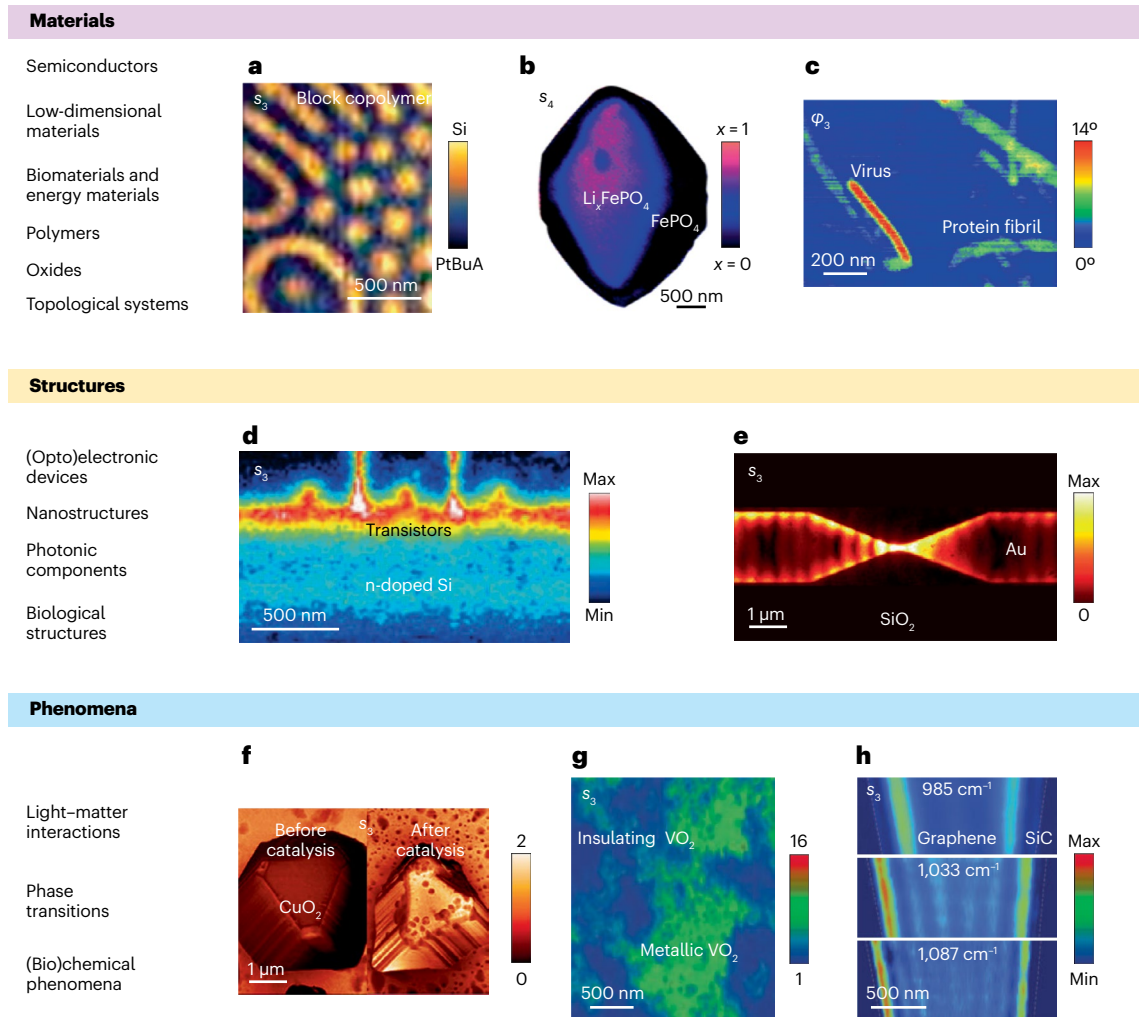


**Fig. 8 | Overview of s-SNOM applications.** **a**, Infrared (1,728 cm<sup>-1</sup>) amplitude image of a block copolymer, visualizing absorption based on the vibrations of the carbonyl bond in the PtBuA block. **b**, Infrared (1,042 cm<sup>-1</sup>) amplitude image of phase distribution of lithiated Li<sub>x</sub>FePO<sub>4</sub> (LFP) and delithiated FePO<sub>4</sub> (FP), showing an outer FP-rich region and an inner LFP-core. **c**, Infrared (1,660 cm<sup>-1</sup>) phase image distinguishing a virus (dominantly α-helical protein structure) from insulin fibrils (dominantly β-sheet protein structure). **d**, Terahertz (84.7 cm<sup>-1</sup>) amplitude image of a polished cut through a multiple-transistor device structure, revealing materials and carrier concentration. **e**, Near-infrared (7,017.5 cm<sup>-1</sup>) amplitude image of surface plasmon polaritons (SPPs) on a tapered metal stripe, showing SPP focusing and interference of forward propagating (from left to right) and back-reflected SPPs. **f**, Infrared (905 cm<sup>-1</sup>)

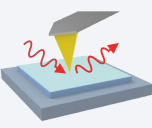
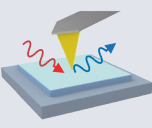
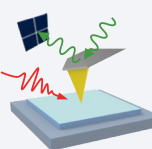
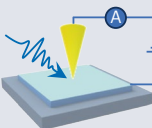
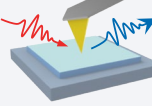
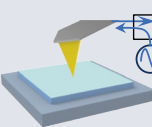
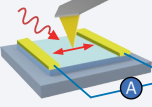
amplitude image of CuO<sub>2</sub> nanocrystals before and after the electrochemical reduction of CO<sub>2</sub>. **g**, Infrared (930 cm<sup>-1</sup>) amplitude image revealing the spatially inhomogeneous insulator-to-metal transition of VO<sub>2</sub> at 343 K. **h**, Infrared amplitude images of plasmon polaritons on graphene, which manifest as fringes parallel to the graphene edges. Panel **a** adapted with permission from ref. 273, American Chemical Society. Panel **b** adapted with permission from ref. 293, American Chemical Society. Panel **c** adapted from ref. 191, CC BY 4.0. Panel **d** adapted with permission from ref. 90, American Chemical Society. Panel **e** adapted with permission from ref. 177, American Chemical Society. Panel **f** adapted with permission from ref. 376, American Chemical Society. Panel **g** adapted with permission from ref. 221, AAAS. Panel **h** adapted from ref. 135, Springer Nature Limited.

fibrils and fibres<sup>190,191,277,295</sup>, membranes<sup>55,89,123,265</sup>, cells<sup>51,296–298</sup>, bones<sup>281</sup>, teeth<sup>102</sup> and core-shell polymer<sup>299</sup> and metal-organic framework<sup>56</sup> particles. Furthermore, semiconductor nanowires<sup>35,138,208</sup>, 2D electron gases at interfaces<sup>206,207,228,300</sup> and moiré superlattices in twisted 2D materials<sup>156,157,301</sup> have been explored, often in terms of their local conductivity and optical excitations. Electronic and optoelectronic building blocks and devices can be characterized as well, such as transistors<sup>90,196</sup> or static random-access memory samples<sup>94,133</sup>, graphene-based IR and THz photodetectors<sup>302–304</sup> and solar cells<sup>305</sup>.

For instance, the THz image of the cross-section of an industrial transistor device (Fig. 8d) allows for distinguishing the different materials and, more importantly, to measure the local carrier concentration<sup>90</sup>.

Moreover, the function of the studied structure or device can be tested and verified. In this regard, s-SNOM has been widely used for visualizing the localization, guiding or focusing of electromagnetic fields with nanophotonic elements<sup>306</sup>, including linear plasmonic and phononic waveguides<sup>177,307</sup>, dielectric<sup>308</sup>, plasmonic<sup>41,91,150,183,186,188,189</sup> and phononic resonators<sup>161,163,164,185</sup>, polaritonic crystals<sup>157,309–312</sup>, twisted

**Table 1 | Comparison of light-assisted scanning probe microscopy techniques**

Technique	Basis and resolution	Illumination	Measured quantity	Accessible properties and effects	Environmental conditions	Samples
 <p>s-SNOM</p>	AFM 10–100 nm	CW fs to ps pulses Vis to sub-THz	Amplitude and phase of elastically tip-scattered light	Complex-valued dielectric function and related materials properties such as chemical composition, structure and conductivity as well as near-field distributions of EM modes	Air Vacuum Liquid Gas Low-T to RT	Insulators Conductors Bulk Thin layers
 <p>TERS<sup>23,365–368</sup>/TEPL<sup>367</sup></p>	AFM, STM 1–100 nm	CW fs to ps pulses UV to near-IR	Intensity of inelastically tip-scattered light (Raman, PL)	TERS: molecule and lattice vibrations, yielding information, for example, on chemical composition and structural properties TEPL: electronic transitions, yielding information on bandgaps, binding energies, carrier recombination, radiative emission rates	Air Vacuum Liquid Gas Low-T to RT	Insulators Conductors Thin layers, often on Au substrate
 <p>AFM-IR<sup>365,369</sup>/PiFM<sup>370</sup></p>	AFM 10–100 nm	ps to ms pulses Vis to IR	Cantilever response due to sample expansion (AFM-IR) or optical forces (PiFM)	AFM-IR: absorption, yielding information on chemical composition and structure PiFM: dielectric properties, yielding chemical composition and structural properties, as well as near-field distributions of EM modes	Air Liquid Gas RT	Insulators Conductors Bulk Thin layers
 <p>THz-STM<sup>22</sup></p>	STM <1 nm	Subcycle THz pulses	Tunnel currents induced by strong THz near fields	Transient occupation of density of states and related ultrafast dynamics	Air Vacuum Low-T to RT	Thin layers on conducting substrate
 <p>LTEN<sup>371,372</sup></p>	AFM 10–100 nm	fs pulses Vis and THz	Amplitude and phase of optically induced THz emission scattered by the tip	Mobile carrier properties	Air Vacuum RT	Insulators Conductors Bulk Thin layers
 <p>MIM<sup>373</sup></p>	AFM 10–100 nm	Microwaves	Amplitude and phase of reflected microwaves	Complex-valued dielectric function and related materials properties such as microwave conductivity	Air Vacuum Liquid Gas Low-T to RT	Insulators Conductors Bulk Thin layers
 <p>PCN<sup>374,375</sup></p>	AFM 10–100 nm	CW UV to THz	Photocurrent-induced near fields at tip apex	Optoelectronic, thermoelectric and thermal properties	Air Vacuum Low-T to RT	Conductors

AFM-IR, atomic force microscopy-based infrared spectroscopy; CW, continuous wave; EM, electromagnetic; IR, infrared; LTEN, laser THz emission nanoscopy; MIM, microwave impedance spectroscopy; PCN, near-field photocurrent nanoscopy; PiFM, photo-induced force microscopy; PL, photoluminescence; RT, room temperature; s-SNOM, scattering-type scanning near-field optical microscopy; TEPL, tip-enhanced photoluminescence spectroscopy; TERS, tip-enhanced Raman scattering spectroscopy; THz, terahertz; THz-STM, THz-scanning tunnelling microscopy; UV, ultraviolet; Vis, visible.

polaritonic slabs<sup>313,314</sup> and polaritonic metasurfaces<sup>170,315</sup>. For example, the s-SNOM image of a metal waveguide structure (Fig. 8e) could verify the efficient compression (focusing) of near-IR plasmon polaritons propagating through a tapered waveguide section<sup>177</sup>. The specific probing mechanisms related to mapping localized and propagating electromagnetic fields are illustrated in Fig. 5b–f.

## Exploring phenomena

s-SNOM and nano-FTIR offer nanoscale spatial resolution and high chemical sensitivity for exploring chemical and biological phenomena, all while being largely non-invasive. For example, heterogeneous catalytic and enzymatic processes can be studied on individual nanoparticles<sup>56,316,317</sup> (Fig. 8f). Further applications include the local characterization of corrosion and material degradation<sup>318–320</sup>, electrochemical processes<sup>262,263,321</sup>, growth of water layers<sup>322</sup>, hydrogen storage in magnesium<sup>101</sup>, (bio)mineralization<sup>323</sup>, as well as protein folding and aggregation<sup>227,261,277</sup>. Phase transitions in different material classes such as ferroelectrics<sup>231</sup>, correlated oxides<sup>52,229,233,245,256,324,325</sup> and transition metal dichalcogenides<sup>326</sup> are another widely studied phenomenon, particularly the Mott metal–insulator transition in VO<sub>2</sub> (refs. 221–223,225,240) and V<sub>2</sub>O<sub>3</sub> (ref. 226) (Fig. 8g). Furthermore, the photoexcitation of charge carriers, as well as carrier accumulation at defects and grain boundaries, for example, in photovoltaic materials and battery materials, can be studied<sup>78,154,195,197,288,305</sup>. The nanoscale concentrated near fields at the tip apex also allow for circumventing the momentum mismatch between free-space light and ultra-confined hybrid light–matter quasiparticles, such as plasmons, phonons and exciton polaritons, and thus for mapping their propagation or localization on nanostructured surfaces<sup>106,135,136,140,144,150,152,173</sup>. For example, Fig. 8h shows an image of graphene plasmon interference fringes near the graphene edges, from which the plasmon dispersion can be measured<sup>135</sup> (see also Fig. 5b).

## Perspectives

Advances in instrumentation, light sources, scanning methods, environmental control and artificial intelligence are set to enhance s-SNOM applications across various fields.

Future developments at synchrotrons<sup>19,21,39,118,119</sup> and free electron lasers<sup>95,96,253</sup> together with tip engineering<sup>82,83,86,327,328</sup> could enable routine nano-FTIR spectroscopy at far-IR<sup>19</sup> and THz frequencies<sup>117</sup>. Monochromatic THz imaging could benefit from QCLs and self-detection schemes<sup>92,93</sup>. Tunable tabletop laser sources such as narrow-band OPO systems<sup>98</sup> could improve the S/N ratio of nanospectroscopy based on sweeping the laser frequency<sup>109,110</sup>. Implementations of ultrafast lasers and field-detecting approaches, such as electrooptic sampling, could be applied for space–time mapping of electromagnetic wave propagation in low-dimensional or photonic systems with ultra-short, subcycle time resolution<sup>78,329</sup> and for near-field imaging and spectroscopy approaching atomic length scales<sup>330</sup>. Non-classical light with time-correlated photon pairs<sup>331,332</sup> may be used for studying quantum phenomena at the single quasiparticle level.

The combination of s-SNOM with traditional scanning probe microscopy techniques, such as force–distance spectroscopy<sup>333</sup>, magnetic force microscopy<sup>233</sup> and Kelvin probe force microscopy<sup>288,334</sup>, will significantly advance multi-messenger nanoscopy<sup>233,335</sup>. This integration enables the simultaneous and comprehensive analysis of optical, mechanical, transport and magnetic properties. We particularly anticipate benefits from combining s-SNOM with other light-assisted scanning probe microscopy techniques (Table 1). Notably, a fruitful combination has emerged with photocurrent nanoscopy and laser THz

emission nanoscopy, both of which are largely developed from s-SNOM instrumentation and utilize higher-harmonic signal demodulation. Owing to their close connection with s-SNOM, these two methods are described in detail in the Supplementary information.

The use of different tip-modulation schemes (such as peak force AFM)<sup>336</sup>, better usage of low-repetition rate<sup>236,337,338</sup> and high-intensity ultrafast lasers may enable the nanoscale probing of nonlinear dynamics or photoinduced phase transitions<sup>223,240</sup>. Retrieving valuable information from hyperspectral data<sup>123,133</sup> with a low S/N ratio might be improved by the integration of compressed sensing<sup>124–128</sup> and advanced machine-learning methods<sup>219</sup> to enhance data analysis<sup>339</sup> and/or to accelerate data acquisition speed. Advances in modelling and calibration methods<sup>340</sup>, in combination with advanced machine learning, may also push forward the idea of near-field optical nanotomography<sup>74,76–78</sup>, that is, the measurement of the local sample permittivity in multilayer samples or more complex 3D sample geometries as a function of both lateral and vertical position.

We anticipate an increasing role of s-SNOM in probing corrosion and material degradation<sup>318–320,341</sup>, electrochemical processes<sup>262,263</sup>, artificial synaptic devices<sup>342</sup> and battery materials<sup>293</sup>. This includes nanoscale studies of the discharge behaviour in conversion batteries, decomposition pathways of electrolytes<sup>321</sup>, formation of interphases<sup>343</sup>, as well as physicochemical interplay at electrode/electrolyte interfaces<sup>293,344,345</sup>. Advances in wet cell sample fabrication<sup>260–262</sup> could facilitate the routine in situ nanoscopy of various aqueous biological materials, including living cells<sup>51</sup>, tissues and catalytic materials<sup>346</sup>. Mapping the secondary structure of proteins<sup>190,191,261,278</sup> might benefit the understanding of the molecular-level development of Alzheimer, Parkinson and other neuro-degenerative diseases. The capability of s-SNOM to quantitatively analyse polymer nanocomposite materials and particles could benefit polymer synthesis<sup>24,273,299,347</sup> and help the identification of microplastics and nanoplastics<sup>348</sup>.

We envision the further exploration of new quantum phases utilizing cryogenic s-SNOM at ultralow temperatures via the application of electric<sup>254,255</sup> or magnetic<sup>257</sup> fields. In this regard, THz or multi-THz photons are especially suitable for probing low-energy excitations (in the order of 1–10 meV) at cryogenic temperatures<sup>232,349</sup>, including correlation gaps, carrier densities or quasiparticle dispersions in topological semimetals<sup>350</sup>, low-dimensional material systems<sup>329,351,352</sup> or superconductors<sup>353–355</sup>. By integrating simultaneous near-field photocurrent mapping, new and innovative measurement techniques can be developed to advance the study of quantum phase transitions under extreme conditions.

We finally anticipate a growing role of s-SNOM in exploring fundamental aspects of nanoscale strong light–matter coupling involving plasmons, phonons, excitons and molecular vibrations<sup>146,356–364</sup>. Different application scenarios can be distinguished, depending on sample and illumination geometries: in one, s-SNOM minimally invasively probes the intrinsic light–matter coupling of the sample<sup>146,358,359,361</sup>; in another one, the probing tip actively engages in the coupling process<sup>356,357,363</sup>, enabling the controlled tuning of the coupling strength by adjusting, for example, the distance between the tip and the sample.

Published online: 10 February 2025

## References

1. Abbe, E. Beiträge zur theorie des mikroskops und der mikroskopischen wahrnehmung: I. Die construction von mikroskopen auf grund der theorie. *Arch. Mikroskop. Anat.* **9**, 413–418 (1873).
2. Hell, S. W. Far-field optical nanoscopy. *Science* **316**, 1153–1158 (2007).
3. Huang, B., Bates, M. & Zhuang, X. Super-resolution fluorescence microscopy. *Ann. Rev. Biochem.* **78**, 993–1016 (2009).



4. Liu, Z., Lavis, L. D. & Betzig, E. Imaging live-cell dynamics and structure at the single-molecule level. *Mol. Cell* **58**, 644–659 (2015).
5. Synge, E. H. XXXVIII. A suggested method for extending microscopic resolution into the ultra-microscopic region. *Lond. Edin. Dubl. Philos. Mag. J. Sci.* **6**, 356–362 (1928).
6. Ash, E. A. & Nicholls, G. Super-resolution aperture scanning microscope. *Nature* **237**, 510–512 (1972).
7. Pohl, D. W., Denk, W. & Lanz, M. Optical stethoscopy: image recording with resolution  $\lambda/20$ . *Appl. Phys. Lett.* **44**, 651–653 (1984).
8. Lewis, A., Isaacson, M., Harootunian, A. & Murray, A. Development of a 500 Å spatial resolution light microscope. I. Light is efficiently transmitted through  $\lambda/16$  diameter apertures. *Ultramicroscopy* **13**, 227–231 (1984).
9. Zenhausern, F., Martin, Y. & Wickramasinghe, H. K. Scanning interferometric apertureless microscopy: optical imaging at 10 angstrom resolution. *Science* **269**, 1083–1085 (1995).
10. Knoll, B. & Keilmann, F. Near-field probing of vibrational absorption for chemical microscopy. *Nature* **399**, 134–137 (1999).
11. Bachelot, R., Gleyzes, P. & Boccaro, A. C. Apertureless near field optical microscopy by local perturbation of a diffraction spot. *Ultramicroscopy* **61**, 111–116 (1995).
12. Kawata, S., Inouye, Y. & Sugiura, T. Near-field scanning optical microscope with a laser trapped probe. *Jpn. J. Appl. Phys.* **33**, L1725–L1727 (1994).
13. Keilmann, F., Van Der Weide, D. W., Eickelkamp, T., Merz, R. & Stöckle, D. Extreme sub-wavelength resolution with a scanning radio-frequency transmission microscope. *Opt. Commun.* **129**, 15–18 (1996).
14. Wurtz, G., Bachelot, R. & Royer, P. Imaging a GaAlAs laser diode in operation using apertureless scanning near-field optical microscopy. *EPJ Appl. Phys.* **5**, 269–275 (1999).
15. Knoll, B. & Keilmann, F. Enhanced dielectric contrast in scattering-type scanning near-field optical microscopy. *Opt. Commun.* **182**, 321–328 (2000).  
**This paper introduces the PDM of s-SNOM.**
16. Hillenbrand, R. & Keilmann, F. Complex optical constants on a subwavelength scale. *Phys. Rev. Lett.* **85**, 3029–3032 (2000).  
**This paper introduces amplitude-resolved and phase-resolved interferometric detection of the tip-scattered light combined with higher-harmonic signal demodulation, as well as the expression s-SNOM.**
17. Keilmann, F. & Hillenbrand, R. Near-field microscopy by elastic light scattering from a tip. *Phil. Trans. R. Soc. A* **362**, 787 (2004).
18. Atkin, J. M., Berweger, S., Jones, A. C. & Raschke, M. B. Nano-optical imaging and spectroscopy of order, phases, and domains in complex solids. *Adv. Phys.* **61**, 745–842 (2012).
19. Khatib, O., Bechtel, H. A., Martin, M. C., Raschke, M. B. & Carr, G. L. Far infrared synchrotron near-field nanoimaging and nanospectroscopy. *ACS Photon.* **5**, 2773–2779 (2018).
20. Chen, X. et al. Modern scattering-type scanning near-field optical microscopy for advanced material research. *Adv. Mater.* **31**, 1804774 (2019).  
**This work reviews the recent progress of s-SNOM, serving as a good overview of the s-SNOM technique and their applications in condensed matter research.**
21. Barcelos, I. D. et al. Probing polaritons in 2D materials with synchrotron infrared nanospectroscopy. *Adv. Opt. Mater.* **8**, 1901091 (2020).
22. Cocker, T. L., Jelic, V., Hillenbrand, R. & Hegmann, F. A. Nanoscale terahertz scanning probe microscopy. *Nat. Photon.* **15**, 558–569 (2021).
23. Choi, B., Jeong, G., Shin, H. H. & Kim, Z. H. Molecular vibrational imaging at nanoscale. *J. Chem. Phys.* **156**, 160902 (2022).
24. Muller, E. A., Pollard, B. & Raschke, M. B. Infrared chemical nano-imaging: accessing structure, coupling, and dynamics on molecular length scales. *J. Phys. Chem. Lett.* **6**, 1275–1284 (2015).
25. Bechtel, H. A., Johnson, S. C., Khatib, O., Muller, E. A. & Raschke, M. B. Synchrotron infrared nano-spectroscopy and -imaging. *Surf. Sci. Rep.* **75**, 100493 (2020).
26. Guo, X. et al. Terahertz nanoscopy: advances, challenges, and the road ahead. *Appl. Phys. Rev.* **11**, 021306 (2024).
27. Novotny, L. From near-field optics to optical antennas. *Phys. Today* **64**, 47–52 (2011).
28. Novotny, L. & Hecht, B. *Principles of Nano-Optics* (Cambridge Univ. Press, 2009).
29. Labardi, M., Patané, S. & Allegrini, M. Artifact-free near-field optical imaging by apertureless microscopy. *Appl. Phys. Lett.* **77**, 621–623 (2000).
30. Mooshammer, F. et al. Quantifying nanoscale electromagnetic fields in near-field microscopy by Fourier demodulation analysis. *ACS Photon.* **7**, 344–351 (2020).
31. Cvitkovic, A., Ocelic, N. & Hillenbrand, R. Analytical model for quantitative prediction of material contrasts in scattering-type near-field optical microscopy. *Opt. Express* **15**, 8550–8565 (2007).  
**This paper introduces and describes the FDM of s-SNOM and provides a corrected version of the PDM.**
32. Ocelic, N., Huber, A. & Hillenbrand, R. Pseudoheterodyne detection for background-free near-field spectroscopy. *Appl. Phys. Lett.* **89**, 101124 (2006).  
**This paper introduces s-SNOM with pseudo-heterodyne detection combined with higher-harmonic signal demodulation.**
33. Hillenbrand, R., Knoll, B. & Keilmann, F. Pure optical contrast in scattering-type scanning near-field microscopy. *J. Microsc.* **202**, 77–83 (2001).
34. Gomez, L. et al. Apertureless scanning near-field optical microscopy: a comparison between homodyne and heterodyne approaches. *J. Opt. Soc. Am. B* **23**, 823 (2006).
35. Stiegler, J. M. et al. Nanoscale free-carrier profiling of individual semiconductor nanowires by infrared near-field nanoscopy. *Nano Lett.* **10**, 1387–1392 (2010).
36. Brehm, M., Taubner, T., Hillenbrand, R. & Keilmann, F. Infrared spectroscopic mapping of single nanoparticles and viruses at nanoscale resolution. *Nano Lett.* **6**, 1307–1310 (2006).
37. Amarie, S. & Keilmann, F. Broadband-infrared assessment of phonon resonance in scattering-type near-field microscopy. *Phys. Rev. B* **83**, 45404 (2011).
38. Pollard, B., Muller, E. A., Hinrichs, K. & Raschke, M. B. Vibrational nano-spectroscopic imaging correlating structure with intermolecular coupling and dynamics. *Nat. Commun.* **5**, 3587 (2014).
39. Bechtel, H. A., Muller, E. A., Olmon, R. L., Martin, M. C. & Raschke, M. B. Ultrabroadband infrared nanospectroscopic imaging. *Proc. Natl Acad. Sci. USA* **111**, 7191–7196 (2014).  
**This work demonstrates nano-FTIR spectroscopy of semiconductor, biomaterial and protein nanostructures using synchrotron radiation.**
40. Hillenbrand, R., Keilmann, F., Hanarp, P., Sutherland, D. S. & Aizpurua, J. Coherent imaging of nanoscale plasmon patterns with a carbon nanotube optical probe. *Appl. Phys. Lett.* **83**, 368–370 (2003).
41. Esteban, R. et al. Direct near-field optical imaging of higher order plasmonic resonances. *Nano Lett.* **8**, 3155–3159 (2008).  
**This work introduces s-polarized illumination for minimally perturbed mapping of the near-field distribution in nanoresonators.**
42. Rang, M. et al. Optical near-field mapping of plasmonic nanoprisms. *Nano Lett.* **8**, 3357–3363 (2008).
43. Govyadinov, A. A., Amenabar, I., Huth, F., Scott Carney, P. & Hillenbrand, R. Quantitative measurement of local infrared absorption and dielectric function with tip-enhanced near-field microscopy. *J. Phys. Chem. Lett.* **4**, 1526–1531 (2013).
44. Huth, F. et al. Nano-FTIR absorption spectroscopy of molecular fingerprints at 20 nm spatial resolution. *Nano Lett.* **12**, 3973 (2012).  
**This paper demonstrates nano-FTIR spectroscopy of molecular vibrations and their correlation with conventional FTIR absorption spectra.**
45. Hillenbrand, R., Taubner, T. & Keilmann, F. Phonon-enhanced light-matter interaction at the nanometre scale. *Nature* **418**, 159 (2002).  
**This work demonstrates polariton-resonant near-field interaction in s-SNOM.**
46. Taubner, T., Hillenbrand, R. & Keilmann, F. Nanoscale polymer recognition by spectral signature in scattering infrared near-field microscopy. *Appl. Phys. Lett.* **85**, 5064–5066 (2004).
47. Mester, L., Govyadinov, A. A. & Hillenbrand, R. High-fidelity nano-FTIR spectroscopy by on-pixel normalization of signal harmonics. *Nanophotonics* **11**, 377–390 (2022).
48. Aizpurua, J., Taubner, T., de Abajo, F. J. G., Brehm, M. & Hillenbrand, R. Substrate-enhanced infrared near-field spectroscopy. *Opt. Express* **16**, 1529–1545 (2008).
49. Autore, M., Mester, L., Goikoetxea, M. & Hillenbrand, R. Substrate matters: surface-polariton enhanced infrared nanospectroscopy of molecular vibrations. *Nano Lett.* **19**, 8066–8073 (2019).
50. Wirth, K. G. et al. Tunable s-SNOM for nanoscale infrared optical measurement of electronic properties of bilayer graphene. *ACS Photon.* **8**, 418–423 (2021).
51. Kaltenecker, K. J., Götz, T., Bau, E. & Keilmann, F. Infrared-spectroscopy, dynamic near-field microscopy of living cells and nanoparticles in water. *Sci. Rep.* **11**, 21860 (2021).  
**This paper demonstrates infrared s-SNOM and nano-FTIR spectroscopy of water-suspended living cells through the 10 nm thick SiN membrane of a liquid cell.**
52. McLeod, A. S. et al. Nano-imaging of strain-tuned stripe textures in a Mott crystal. *npj Quant. Mater.* **6**, 46 (2021).
53. Malovichko, I., Govyadinov, A., Huth, F. & Diem, M. Method for referencing a near-field measurement with drift and fluctuation correction. Patent EP3940393A1 (2022).
54. Mastel, S., Govyadinov, A. A., de Oliveira, T. V. A. G., Amenabar, I. & Hillenbrand, R. Nanoscale-resolved chemical identification of thin organic films using infrared near-field spectroscopy and standard Fourier transform infrared references. *Appl. Phys. Lett.* **106**, 023113 (2015).
55. Heberle, J. & Pfizner, E. Infrared scattering-type scanning near-field optical microscopy of biomembranes in water. *J. Phys. Chem. Lett.* **11**, 8183–8188 (2020).
56. Man, T. et al. Hierarchically encapsulating enzymes with multi-shelled metal-organic frameworks for tandem biocatalytic reactions. *Nat. Commun.* **13**, 305 (2022).
57. Niehues, I. et al. Identification of weak molecular absorption in single-wavelength s-SNOM images. *Opt. Express* **31**, 7012–7022 (2023).
58. Paul, S. et al. 13C- and 15N-labeling of amyloid- $\beta$  and inhibitory peptides to study their interaction via nanoscale infrared spectroscopy. *Commun. Chem.* **6**, 163 (2023).
59. Raschke, M. B. & Lienau, C. Apertureless near-field optical microscopy: tip-sample coupling in elastic light scattering. *Appl. Phys. Lett.* **83**, 5089–5091 (2003).
60. Hillenbrand, R. & Keilmann, F. Material-specific mapping of metal/semiconductor/dielectric nanosystems at 10 nm resolution by backscattering near-field optical microscopy. *Appl. Phys. Lett.* **80**, 25–27 (2002).
61. Mastel, S. et al. Understanding the image contrast of material boundaries in IR nanoscopy reaching 5 nm spatial resolution. *ACS Photon.* **5**, 3372 (2018).
62. Chen, X. et al. THz near-field imaging of extreme subwavelength metal structures. *ACS Photon.* **7**, 687–694 (2020).
63. Bijeon, J. L., Adam, P. M., Barchiesi, D. & Royer, P. Definition of a simple resolution criterion in an apertureless scanning near-field optical microscope (A-SNOM): contribution of the tip vibration and lock-in detection. *EPJ Appl. Phys.* **26**, 45–52 (2004).
64. Krutokhvostov, R. et al. Enhanced resolution in subsurface near-field optical microscopy. *Opt. Express* **20**, 593–600 (2012).
65. Walford, J. N. et al. Influence of tip modulation on image formation in scanning near-field optical microscopy. *J. Appl. Phys.* **89**, 5159–5169 (2001).

66. Esteban, R., Vogelgesang, R. & Kern, K. Full simulations of the apertureless scanning near field optical microscopy signal: achievable resolution and contrast. *Opt. Express* **17**, 2518–2529 (2009).
67. Nishida, J. et al. Sub-tip-radius near-field interactions in nano-FTIR vibrational spectroscopy on single proteins. *Nano Lett.* **24**, 836–843 (2024).
68. Maissen, C., Chen, S., Nikulina, E., Govyadinov, A. & Hillenbrand, R. Probes for ultrasensitive THz nanoscopy. *ACS Photon.* **6**, 1279 (2019).
69. Taubner, T., Keilmann, F. & Hillenbrand, R. Nanoscale-resolved subsurface imaging by scattering-type near-field optical microscopy. *Opt. Express* **13**, 8893 (2005).
70. Mester, L., Govyadinov, A. A., Chen, S., Goikoetxea, M. & Hillenbrand, R. Subsurface chemical nanoidentification by nano-FTIR spectroscopy. *Nat. Commun.* **11**, 3359 (2020).
71. Moon, K. et al. Subsurface nanoimaging by broadband terahertz pulse near-field microscopy. *Nano Lett.* **15**, 549–552 (2015).
72. Jacob, R. et al. Intersublevel spectroscopy on single InAs-quantum dots by terahertz near-field microscopy. *Nano Lett.* **12**, 4336–4340 (2012).
73. Raschke, M. B. et al. Apertureless near-field vibrational imaging of block-copolymer nanostructures with ultrahigh spatial resolution. *ChemPhysChem* **6**, 2197–2203 (2005).
74. Govyadinov, A. A. et al. Recovery of permittivity and depth from near-field data as a step toward infrared nanotomography. *ACS Nano* **8**, 6911–6921 (2014).
75. Engelhardt, A. P., Hauer, B. & Taubner, T. Visibility of weak contrasts in subsurface scattering near-field microscopy. *Ultramicroscopy* **126**, 40–43 (2013).
76. Mooshammer, F. et al. Nanoscale near-field tomography of surface states on  $(\text{Bi}_{0.5}\text{Sb}_{0.5})_2\text{Te}_3$ . *Nano Lett.* **18**, 7515–7523 (2018).
77. Sun, J., Schotland, J. C., Hillenbrand, R. & Carney, P. S. Nanoscale optical tomography using volume-scanning near-field microscopy. *Appl. Phys. Lett.* **95**, 121108 (2009).
78. Eisele, M. et al. Ultrafast multi-terahertz nano-spectroscopy with sub-cycle temporal resolution. *Nat. Photon.* **8**, 841–845 (2014).  
**This work demonstrates time-resolved multi-THz nanospectroscopy using electro-optic sampling.**
79. Cvitkovic, A., Ocelic, N., Aizpurua, J., Guckenberger, R. & Hillenbrand, R. Infrared imaging of single nanoparticles via strong field enhancement in a scanning nanogap. *Phys. Rev. Lett.* **97**, 60801 (2006).
80. Mattis Hoffmann, J., Hauer, B. & Taubner, T. Antenna-enhanced infrared near-field nanospectroscopy of a polymer. *Appl. Phys. Lett.* **101**, 193105 (2012).
81. von Ribbeck, H.-G. et al. Spectroscopic THz near-field microscope. *Opt. Express* **16**, 3430–3438 (2008).
82. Siday, T., Hale, L. L., Hermans, R. I. & Mitrofanov, O. Resonance-enhanced terahertz nanoscopy probes. *ACS Photon.* **7**, 596–601 (2020).
83. Mastel, S. et al. Terahertz nanofocusing with cantilevered terahertz-resonant antenna tips. *Nano Lett.* **17**, 6526–6533 (2017).
84. Moon, Y. et al. Reference-free self-calibrating tip-based scattering-type THz near-field microscopy. *AIP Adv.* **13**, 065211 (2023).
85. Pistore, V. et al. Near-field probes for sensitive detectorless near-field nanoscopy in the 2.0–4.6 THz range. *Appl. Phys. Lett.* **124**, 221105 (2024).
86. Huth, F. et al. Resonant antenna probes for tip-enhanced infrared near-field microscopy. *Nano Lett.* **13**, 1065–1072 (2013).
87. Deutsch, B., Hillenbrand, R. & Novotny, L. Near-field amplitude and phase recovery using phase-shifting interferometry. *Opt. Express* **16**, 494–501 (2008).
88. Schnell, M., Carney, P. S. & Hillenbrand, R. Synthetic optical holography for rapid nanoimaging. *Nat. Commun.* **5**, 3499 (2014).
89. Berweger, S. et al. Nano-chemical infrared imaging of membrane proteins in lipid bilayers. *J. Am. Chem. Soc.* **135**, 18292–18295 (2013).
90. Huber, A. J., Keilmann, F., Wittborn, J., Aizpurua, J. & Hillenbrand, R. Terahertz near-field nanoscopy of mobile carriers in single semiconductor nanodevices. *Nano Lett.* **8**, 3766–3770 (2008).  
**This work demonstrates THz s-SNOM with a spatial resolution below 100 nm.**
91. Thomas, L. et al. Imaging of THz photonic modes by scattering scanning near-field optical microscopy. *ACS Appl. Mater. Interfaces* **14**, 32608–32617 (2022).
92. Dean, P. et al. Apertureless near-field terahertz imaging using the self-mixing effect in a quantum cascade laser. *Appl. Phys. Lett.* **108**, 091113 (2016).
93. Giordano, M. C. et al. Phase-resolved terahertz self-detection near-field microscopy. *Opt. Express* **26**, 18423–18435 (2018).
94. Liewald, C. et al. All-electronic terahertz nanoscopy. *Optica* **5**, 159 (2018).
95. Kehr, S. C. et al. Anisotropy contrast in phonon-enhanced apertureless near-field microscopy using a free-electron laser. *Phys. Rev. Lett.* **100**, 256403 (2008).
96. de Oliveira, T. V. A. G. et al. Nanoscale-confined terahertz polaritons in a van der Waals crystal. *Adv. Mater.* **33**, 2005777 (2021).
97. Kuschewski, F. et al. Narrow-band near-field nanoscopy in the spectral range from 1.3 to 8.5 THz. *Appl. Phys. Lett.* **108**, 113102 (2016).
98. Hegenbarth, R. et al. High-power femtosecond mid-IR sources for s-SNOM applications. *J. Opt.* **16**, 094003 (2014).
99. Matson, J. et al. Controlling the propagation asymmetry of hyperbolic shear polaritons in beta-gallium oxide. *Nat. Commun.* **14**, 5240 (2023).
100. Sternbach, A. J. et al. Negative refraction in hyperbolic hetero-bicrystals. *Science* **379**, 555–557 (2023).
101. Karst, J. et al. Watching in situ the hydrogen diffusion dynamics in magnesium on the nanoscale. *Sci. Adv.* **6**, eaaz0566 (2020).
102. Beddoe, M. et al. Probing the micro- and nanoscopic properties of dental materials using infrared spectroscopy: a proof-of-principle study. *Acta Biomater.* **168**, 309–322 (2023).
103. Chen, S. et al. Real-space nanoimaging of THz polaritons in the topological insulator  $\text{Bi}_2\text{Se}_3$ . *Nat. Commun.* **13**, 1374 (2022).
104. Chen, C. et al. Terahertz nanoimaging and nanospectroscopy of chalcogenide phase-change materials. *ACS Photon.* **7**, 3499–3506 (2020).
105. Pogna, E. A. A. et al. Mapping propagation of collective modes in  $\text{Bi}_2\text{Se}_3$  and  $\text{Bi}_2\text{Te}_{2-x}\text{Se}_{x+8}$  topological insulators by near-field terahertz nanoscopy. *Nat. Commun.* **12**, 6672 (2021).
106. Chen, S. et al. Real-space observation of ultraconfined in-plane anisotropic acoustic terahertz plasmon polaritons. *Nat. Mater.* **22**, 860–866 (2023).
107. Fei, Z. et al. Infrared nanoscopy of dirac plasmons at the graphene- $\text{SiO}_2$  interface. *Nano Lett.* **11**, 4701–4705 (2011).
108. Zhang, S. et al. Nano-spectroscopy of excitons in atomically thin transition metal dichalcogenides. *Nat. Commun.* **13**, 542 (2022).
109. Yoxall, E., Schnell, M., Mastel, S. & Hillenbrand, R. Magnitude and phase-resolved infrared vibrational nanospectroscopy with a swept quantum cascade laser. *Opt. Express* **23**, 13358–13369 (2015).
110. Barnett, J. et al. Mid-infrared near-field fingerprint spectroscopy of the 2D electron gas in  $\text{LaAlO}_3/\text{SrTiO}_3$  at low temperatures. Preprint at <https://doi.org/10.48550/arXiv.2311.07354> (2023).
111. Brehm, M., Schliesser, A. & Keilmann, F. Spectroscopic near-field microscopy using frequency combs in the mid-infrared. *Opt. Express* **14**, 11222–11233 (2006).
112. Amarie, S., Ganz, T. & Keilmann, F. Mid-infrared near-field spectroscopy. *Opt. Express* **17**, 21794–21801 (2009).
113. Xu, X. G., Rang, M., Craig, I. M. & Raschke, M. B. Pushing the sample-size limit of infrared vibrational nanospectroscopy: from monolayer toward single molecule sensitivity. *J. Phys. Chem. Lett.* **3**, 1836–1841 (2012).  
**This paper demonstrates nano-FTIR spectroscopy of molecular monolayers.**
114. Huth, F., Schnell, M., Wittborn, J., Ocelic, N. & Hillenbrand, R. Infrared-spectroscopic nanoimaging with a thermal source. *Nat. Mater.* **10**, 352 (2011).
115. Németh, G., Bechtel, H. A. & Borondics, F. Origins and consequences of asymmetric nano-FTIR interferograms. *Opt. Express* **32**, 15280 (2024).
116. Larson, J. M., Bechtel, H. A. & Kostecki, R. Detection and signal processing for near-field nanoscale Fourier transform infrared spectroscopy. *Adv. Funct. Mater.* **34**, 2406643 (2024).
117. Wehmeier, L. et al. Ultrabroadband terahertz near-field nanospectroscopy with a HgCdTe detector. *ACS Photon.* **10**, 4329–4339 (2023).
118. Peragut, F., Frubach, J.-B., Roy, P. & De Wilde, Y. Infrared near-field imaging and spectroscopy based on thermal or synchrotron radiation. *Appl. Phys. Lett.* **104**, 251118 (2014).
119. Hermann, P. et al. Near-field imaging and nano-Fourier-transform infrared spectroscopy using broadband synchrotron radiation. *Opt. Express* **21**, 2913–2919 (2013).
120. Lahneman, D. J. et al. Broadband near-field infrared spectroscopy with a high temperature plasma light source. *Opt. Express* **25**, 20421–20430 (2017).
121. Wagner, M. et al. Ultrabroadband nanospectroscopy with a laser-driven plasma source. *ACS Photon.* **5**, 1467–1475 (2018).
122. Santos, T. M. et al. Synchrotron infrared nanospectroscopy in fourth-generation storage rings. *J. Synchrotron Radiat.* **31**, 547–556 (2024).
123. Amenabar, I. et al. Hyperspectral infrared nanoimaging of organic samples based on Fourier transform infrared nanospectroscopy. *Nat. Commun.* **8**, 14402 (2017).
124. Schnell, M., Goikoetxea, M., Amenabar, I., Carney, P. S. & Hillenbrand, R. Rapid infrared spectroscopic nanoimaging with nano-FTIR holography. *ACS Photon.* **7**, 2878 (2020).
125. Fu, M. et al. Accelerated nano-optical imaging through sparse sampling. *Nano Lett.* **24**, 2149–2156 (2024).
126. Johnson, S. C. et al. Infrared nanospectroscopic imaging in the rotating frame. *Optica* **6**, 424–429 (2019).
127. Labouesse, S., Johnson, S. C., Bechtel, H. A., Raschke, M. B. & Piestun, R. Smart scattering scanning near-field optical microscopy. *ACS Photon.* **7**, 3346–3352 (2020).
128. Kästner, B. et al. Compressed sensing FTIR nano-spectroscopy and nano-imaging. *Opt. Express* **26**, 18115–18124 (2018).
129. Koch, M., Mittleman, D. M., Ornik, J. & Castro-Camus, E. Terahertz time-domain spectroscopy. *Nat. Rev. Methods Primers* **3**, 48 (2023).
130. Chen, H.-T., Kersting, R. & Cho, G. C. Terahertz imaging with nanometer resolution. *Appl. Phys. Lett.* **83**, 3009–3011 (2003).
131. Stinson, H. T. et al. Imaging the nanoscale phase separation in vanadium dioxide thin films at terahertz frequencies. *Nat. Commun.* **9**, 3604 (2018).
132. Moon, K. et al. Computed terahertz near-field mapping of molecular resonances of lactose stereo-isomer impurities with sub-attomole sensitivity. *Sci. Rep.* **9**, 16915 (2019).
133. Aghamiri, N. A. et al. Hyperspectral time-domain terahertz nano-imaging. *Opt. Express* **27**, 24231 (2019).
134. Tranca, D. E., Stanciu, S. G., Hristu, R., Latterini, L. & Stanciu, G. A. Surface optical characterization at nanoscale using phasor representation of data acquired by scattering scanning near-field optical microscopy. *Appl. Surf. Sci.* **509**, 145347 (2020).
135. Chen, J. et al. Optical nano-imaging of gate-tunable graphene plasmons. *Nature* **487**, 77–81 (2012).  
**In this work, s-SNOM is used to visualize the frequency-dependent propagation of graphene plasmons, as well as the tuning of resonant localized modes by electrical gating.**
136. Fei, Z. et al. Gate-tuning of graphene plasmons revealed by infrared nano-imaging. *Nature* **487**, 82 (2012).  
**In this work, s-SNOM is employed to image propagating graphene plasmons and to visualize how their wavelengths can be tuned by electrical gating.**

137. Shi, Z. et al. Observation of a Luttinger-liquid plasmon in metallic single-walled carbon nanotubes. *Nat. Photon.* **9**, 515–519 (2015).
138. Zhou, Y. et al. Tunable low loss 1D surface plasmons in InAs nanowires. *Adv. Mater.* **30**, 1802551 (2018).
139. Shi, Z. et al. Amplitude- and phase-resolved nanospectral imaging of phonon polaritons in hexagonal boron nitride. *ACS Photon.* **2**, 790–796 (2015).
140. Dai, S. et al. Tunable phonon polaritons in atomically thin van der Waals crystals of boron nitride. *Science* **343**, 1125–1129 (2014).  
**In this work, s-SNOM is used to image out-of-plane hyperbolic phonon polaritons in van der Waals materials.**
141. Xu, X. G. et al. One-dimensional surface phonon polaritons in boron nitride nanotubes. *Nat. Commun.* **5**, 4782 (2014).
142. Mancini, A. et al. Near-field retrieval of the surface phonon polariton dispersion in free-standing silicon carbide thin films. *ACS Photon.* **9**, 3696–3704 (2022).
143. Li, P. et al. Reversible optical switching of highly confined phonon-polaritons with an ultrathin phase-change material. *Nat. Mater.* **15**, 870–875 (2016).
144. Ma, W. et al. In-plane anisotropic and ultra-low-loss polaritons in a natural van der Waals crystal. *Nature* **562**, 557–562 (2018).  
**In this work, s-SNOM is used to visualize in real space in-plane hyperbolic phonon polaritons in a natural van der Waals crystal.**
145. Zheng, Z. et al. Highly confined and tunable hyperbolic phonon polaritons in van der Waals semiconducting transition metal oxides. *Adv. Mater.* **30**, 1705318 (2018).
146. Hu, F. et al. Imaging exciton-polariton transport in MoSe<sub>2</sub> waveguides. *Nat. Photon.* **11**, 356–360 (2017).
147. Hu, D. et al. Probing optical anisotropy of nanometer-thin van der Waals microcrystals by near-field imaging. *Nat. Commun.* **8**, 1471 (2017).
148. Walla, F. et al. Anisotropic excitation of surface plasmon polaritons on a metal film by a scattering-type scanning near-field microscope with a non-rotationally-symmetric probe tip. *Nanophotonics* **7**, 269–276 (2018).
149. Kaltenecker, K. J. et al. Mono-crystalline gold platelets: a high-quality platform for surface plasmon polaritons. *Nanophotonics* **9**, 509–522 (2020).
150. Nikitin, A. Y. et al. Real-space mapping of tailored sheet and edge plasmons in graphene nanoresonators. *Nat. Photon.* **10**, 239–243 (2016).
151. Fei, Z. et al. Edge and surface plasmons in graphene nanoribbons. *Nano Lett.* **15**, 8271–8276 (2015).
152. Li, P. et al. Optical nanoimaging of hyperbolic surface polaritons at the edges of van der Waals materials. *Nano Lett.* **17**, 228 (2017).
153. Hauer, B. et al. Exploiting phonon-resonant near-field interaction for the nanoscale investigation of extended defects. *Adv. Funct. Mater.* **30**, 1907357 (2020).
154. Fei, Z. et al. Electronic and plasmonic phenomena at graphene grain boundaries. *Nat. Nanotechnol.* **8**, 821–825 (2013).
155. Gerber, J. A., Berweger, S., O’Callahan, B. T. & Raschke, M. B. Phase-resolved surface plasmon interferometry of graphene. *Phys. Rev. Lett.* **113**, 55502 (2014).
156. Luo, Y. et al. In situ nanoscale imaging of moiré superlattices in twisted van der Waals heterostructures. *Nat. Commun.* **11**, 4209 (2020).
157. Sunku, S. S. et al. Photonic crystals for nano-light in moiré graphene superlattices. *Science* **362**, 1153–1156 (2018).
158. Woessner, A. et al. Highly confined low-loss plasmons in graphene-boron nitride heterostructures. *Nat. Mater.* **14**, 421–425 (2015).
159. Álvarez-Pérez, G. et al. Infrared permittivity of the biaxial van der Waals semiconductor  $\alpha$ -MoO<sub>3</sub> from near- and far-field correlative studies. *Adv. Mater.* **32**, 1908176 (2020).
160. Lyu, B. et al. Phonon polariton-assisted infrared nanoimaging of local strain in hexagonal boron nitride. *Nano Lett.* **19**, 1982 (2019).
161. Alfaro-Mozaz, F. J. et al. Nanoimaging of resonating hyperbolic polaritons in linear boron nitride antennas. *Nat. Commun.* **8**, 15624 (2017).
162. Feres, F. H. et al. Sub-diffractive cavity modes of terahertz hyperbolic phonon polaritons in tin oxide. *Nat. Commun.* **12**, 1995 (2021).
163. Yu, S. J. et al. Ultrahigh-quality infrared polaritonic resonators based on bottom-up-synthesized van der Waals nanoribbons. *ACS Nano* **16**, 3027–3035 (2022).
164. Tamagnone, M. et al. Ultra-confined mid-infrared resonant phonon polaritons in van der Waals nanostructures. *Sci. Adv.* **4**, eaat7189 (2018).
165. Conrads, L., Schüller, L., Wirth, K. G., Wuttig, M. & Taubner, T. Direct programming of confined surface phonon polariton resonators with the plasmonic phase-change material In<sub>3</sub>SbTe<sub>2</sub>. *Nat. Commun.* **15**, 3472 (2024).
166. Dai, S. et al. Efficiency of launching highly confined polaritons by infrared light incident on a hyperbolic material. *Nano Lett.* **17**, 5285–5290 (2017).
167. Yoxall, E. et al. Direct observation of ultraslow hyperbolic polariton propagation with negative phase velocity. *Nat. Photon.* **9**, 674 (2015).
168. Huber, A., Ocelic, N., Kazantsev, D. & Hillenbrand, R. Near-field imaging of mid-infrared surface phonon polariton propagation. *Appl. Phys. Lett.* **87**, 081103 (2005).
169. Ni, G. X. et al. Fundamental limits to graphene plasmonics. *Nature* **557**, 530–533 (2018).  
**This work investigates graphene plasmons at cryogenic temperatures down to 60K.**
170. Li, P. et al. Infrared hyperbolic metasurface based on nanostructured van der Waals materials. *Science* **359**, 892–896 (2018).
171. Hu, H. et al. Gate-tunable negative refraction of mid-infrared polaritons. *Science* **379**, 558–561 (2023).
172. Barnett, J. et al. Investigation of low-confinement surface phonon polariton launching on SiC and SrTiO<sub>3</sub> using scanning near-field optical microscopy. *Appl. Phys. Lett.* **120**, 211107 (2022).
173. Zheng, Z. et al. A mid-infrared biaxial hyperbolic van der Waals crystal. *Sci. Adv.* **5**, eaav8690 (2019).
174. Hu, G. et al. Real-space nanoimaging of hyperbolic shear polaritons in a monoclinic crystal. *Nat. Nanotechnol.* **18**, 64–70 (2023).
175. Zhang, Q. et al. Unidirectionally excited phonon polaritons in high-symmetry orthorhombic crystals. *Sci. Adv.* **8**, eaab9774 (2022).
176. Schnell, M. et al. Nanofocusing of mid-infrared energy with tapered transmission lines. *Nat. Photon.* **5**, 283–287 (2011).
177. Zenin, V. A. et al. Boosting local field enhancement by on-chip nanofocusing and impedance-matched plasmonic antennas. *Nano Lett.* **15**, 8148–8154 (2015).
178. Alonso-González, P. et al. Controlling graphene plasmons with resonant metal antennas and spatial conductivity patterns. *Science* **344**, 1369–1373 (2014).
179. Andryieuski, A. et al. Direct characterization of plasmonic slot waveguides and nanocouplers. *Nano Lett.* **14**, 3925–3929 (2014).
180. Sarriguarte, P., Schnell, M., Chuvilin, A. & Hillenbrand, R. Polarization-resolved near-field characterization of nanoscale infrared modes in transmission lines fabricated by gallium and helium ion beam milling. *ACS Photon.* **1**, 604–611 (2014).
181. Prämassing, M., Liebrau, M., Schill, H. J., Irsen, S. & Linden, S. Interferometric near-field resonant characterization of plasmonic slot waveguides in single- and poly-crystalline gold films. *Opt. Express* **28**, 12998–13007 (2020).
182. Tseses, S. et al. Optical skyrmion lattice in evanescent electromagnetic fields. *Science* **361**, 993–996 (2018).
183. Dorfmueller, J. et al. Fabry-Pérot resonances in one-dimensional plasmonic nanostructures. *Nano Lett.* **9**, 2372–2377 (2009).
184. Schnell, M. et al. Controlling the near-field oscillations of loaded plasmonic nanoantennas. *Nat. Photon.* **3**, 287–291 (2009).
185. Wang, T., Li, P., Hauer, B., Chigrin, D. N. & Taubner, T. Optical properties of single infrared resonant circular microcavities for surface phonon polaritons. *Nano Lett.* **13**, 5051–5055 (2013).
186. Alonso-González, P. et al. Resolving the electromagnetic mechanism of surface-enhanced light scattering at single hot spots. *Nat. Commun.* **3**, 684 (2012).
187. Kim, D.-S. et al. Real-space mapping of the strongly coupled plasmons of nanoparticle dimers. *Nano Lett.* **9**, 3619–3625 (2009).
188. Olmon, R. L. et al. Determination of electric-field, magnetic-field, and electric-current distributions of infrared optical antennas: a near-field optical vector network analyzer. *Phys. Rev. Lett.* **105**, 167403 (2010).
189. Neuman, T. et al. Mapping the near fields of plasmonic nanoantennas by scattering-type scanning near-field optical microscopy. *Laser Photon. Rev.* **9**, 637–649 (2015).
190. Paulite, M. et al. Imaging secondary structure of individual amyloid fibrils of a  $\beta$ 2-microglobulin fragment using near-field infrared spectroscopy. *J. Am. Chem. Soc.* **133**, 7376–7383 (2011).
191. Amenabar, I. et al. Structural analysis and mapping of individual protein complexes by infrared nanospectroscopy. *Nat. Commun.* **4**, 2890 (2013).  
**This work demonstrates the capability of s-SNOM and nano-FTIR spectroscopy for analyzing the secondary structure of individual protein complexes, membranes and fibrils.**
192. Meyns, M., Primpke, S. & Gerdts, G. Library based identification and characterisation of polymers with nano-FTIR and IR-sSNOM imaging. *Anal. Methods* **11**, 5195–5202 (2019).
193. Wolny, G., Bründermann, E., Arsov, Z., Quaroni, L. & Havenith, M. Nanoscale depth resolution in scanning near-field infrared microscopy. *Opt. Express* **16**, 7453–7459 (2008).
194. Knoll, B. & Keilmann, F. Infrared conductivity mapping for nanoelectronics. *Appl. Phys. Lett.* **77**, 3980–3982 (2000).
195. Wagner, M. et al. Ultrafast dynamics of surface plasmons in InAs by time-resolved infrared nanospectroscopy. *Nano Lett.* **14**, 4529 (2014).
196. Huber, A. J., Kazantsev, D., Keilmann, F., Wittborn, J. & Hillenbrand, R. Simultaneous IR material recognition and conductivity mapping by nanoscale near-field microscopy. *Adv. Mater.* **19**, 2209–2212 (2007).
197. Lewin, M. et al. Nanospectroscopy of infrared phonon resonance enables local quantification of electronic properties in doped SrTiO<sub>3</sub> ceramics. *Adv. Funct. Mater.* **28**, 1802834 (2018).
198. McLeod, A. S. et al. Model for quantitative tip-enhanced spectroscopy and the extraction of nanoscale-resolved optical constants. *Phys. Rev. B* **90**, 85136 (2014).
199. Xu, R. et al. Highly confined epsilon-near-zero and surface phonon polaritons in SrTiO<sub>3</sub> membranes. *Nat. Commun.* **15**, 4743 (2024).
200. Amarie, S. et al. Nano-FTIR chemical mapping of minerals in biological materials. *Beilstein J. Nanotechnol.* **3**, 312–323 (2012).
201. Dominguez, G. et al. Nanoscale infrared spectroscopy as a non-destructive probe of extraterrestrial samples. *Nat. Commun.* **5**, 5445 (2014).
202. Huber, A., Ocelic, N., Taubner, T. & Hillenbrand, R. Nanoscale resolved infrared probing of crystal structure and of plasmon-phonon coupling. *Nano Lett.* **6**, 774–778 (2006).
203. Ocelic, N. & Hillenbrand, R. Subwavelength-scale tailoring of surface phonon polaritons by focused ion-beam implantation. *Nat. Mater.* **3**, 606–609 (2004).
204. Huber, A. J., Ziegler, A., Köck, T. & Hillenbrand, R. Infrared nanoscopy of strained semiconductors. *Nat. Nanotechnol.* **4**, 153–157 (2009).
205. Bensmann, S. et al. Near-field imaging and spectroscopy of locally strained GaN using an IR broadband laser. *Opt. Express* **22**, 22369–22381 (2014).
206. Barnett, J. et al. Phonon-enhanced near-field spectroscopy to extract the local electronic properties of buried 2D electron systems in oxide heterostructures. *Adv. Funct. Mater.* **30**, 2004767 (2020).



207. Qin, T.-X. et al. Revealing the interaction of charge carrier–phonon coupling by quantification of electronic properties at the SrTiO<sub>3</sub>/TiO<sub>2</sub> heterointerface. *Nano Lett.* **22**, 2755–2761 (2022).
208. Ritchie, E. T. et al. Mapping free-carriers in multijunction silicon nanowires using infrared near-field optical microscopy. *Nano Lett.* **17**, 6591–6597 (2017).
209. Hauer, B., Engelhardt, A. P. & Taubner, T. Quasi-analytical model for scattering infrared near-field microscopy on layered systems. *Opt. Express* **20**, 13173–13188 (2012).
210. Vincent, T. et al. snumpy: a package for modelling scattering-type scanning near-field optical microscopy. Preprint at <https://arxiv.org/abs/2405.20948> (2024).
211. Jiang, B. Y., Zhang, L. M., Castro Neto, A. H., Basov, D. N. & Fogler, M. M. Generalized spectral method for near-field optical microscopy. *J. Appl. Phys.* **119**, 054305 (2016).
212. Chui, S. T., Chen, X., Liu, M., Lin, Z. & Zi, J. Scattering of electromagnetic waves from a cone with conformal mapping: application to scanning near-field optical microscope. *Phys. Rev. B* **97**, 81406 (2018).
213. Chen, X. et al. Rapid simulations of hyperspectral near-field images of three-dimensional heterogeneous surfaces — part II. *Opt. Express* **30**, 11228 (2022).
214. Ruta, F. L., Sternbach, A. J., Dieng, A. B., McLeod, A. S. & Basov, D. N. Quantitative nanoinfrared spectroscopy of anisotropic van der Waals materials. *Nano Lett.* **20**, 7933–7940 (2020).
215. Babicheva, V. E., Gamage, S., Stockman, M. I. & Abate, Y. Near-field edge fringes at sharp material boundaries. *Opt. Express* **25**, 23935 (2017).
216. Luan, Y., McDermott, L., Hu, F. & Fei, Z. Tip- and plasmon-enhanced infrared nanoscopy for ultrasensitive molecular characterizations. *Phys. Rev. Appl.* **13**, 34020 (2020).
217. McArdle, P., Lahneman, D. J., Biswas, A., Keilmann, F. & Qazilbash, M. M. Near-field infrared nanospectroscopy of surface phonon–polariton resonances. *Phys. Rev. Res.* **2**, 23272 (2020).
218. Zhao, Y., Chen, X., Yao, Z., Liu, M. K. & Fogler, M. M. Deep-learning-aided extraction of optical constants in scanning near-field optical microscopy. *J. Appl. Phys.* **133**, 133105 (2023).
219. Chen, X. et al. Machine learning for optical scanning probe nanoscopy. *Adv. Mater.* **35**, 2109171 (2023).
220. Chen, X., Ren, R. & Liu, M. Validity of machine learning in the quantitative analysis of complex scanning near-field optical microscopy signals using simulated data. *Phys. Rev. Appl.* **15**, 14001 (2021).
221. Qazilbash, M. M. et al. Mott transition in VO<sub>2</sub> revealed by infrared spectroscopy and nano-imaging. *Science* **318**, 1750–1753 (2007).  
**In this work, s-SNOM is used to demonstrate phase separation in correlated electron material systems.**
222. Liu, M. et al. Symmetry breaking and geometric confinement in VO<sub>2</sub>: results from a three-dimensional infrared nano-imaging. *Appl. Phys. Lett.* **104**, 121905 (2014).
223. O’Callahan, B. T. et al. Inhomogeneity of the ultrafast insulator-to-metal transition dynamics of VO<sub>2</sub>. *Nat. Commun.* **6**, 6849 (2015).
224. Liu, M. K. et al. Anisotropic electronic state via spontaneous phase separation in strained vanadium dioxide films. *Phys. Rev. Lett.* **111**, 96602 (2013).
225. Jones, A. C., Berweger, S., Wei, J., Cobden, D. & Raschke, M. B. Nano-optical investigations of the metal–insulator phase behavior of individual VO<sub>2</sub> microcrystals. *Nano Lett.* **10**, 1574–1581 (2010).
226. McLeod, A. S. et al. Nanotextured phase coexistence in the correlated insulator V<sub>2</sub>O<sub>3</sub>. *Nat. Phys.* **13**, 80–86 (2017).
227. Lee, W. et al. A rewritable optical storage medium of silk proteins using near-field nano-optics. *Nat. Nanotechnol.* **15**, 941–947 (2020).
228. Luo, W. et al. High sensitivity variable-temperature infrared nanoscopy of conducting oxide interfaces. *Nat. Commun.* **10**, 2774 (2019).
229. Post, K. W. et al. Coexisting first- and second-order electronic phase transitions in a correlated oxide. *Nat. Phys.* **14**, 1056–1061 (2018).
230. Yang, H. U., Hebestreit, E., Josberger, E. E. & Raschke, M. B. A cryogenic scattering-type scanning near-field optical microscope. *Rev. Sci. Instrum.* **84**, 023701 (2013).
231. Döring, J. et al. Low-temperature nanospectroscopy of the structural ferroelectric phases in single-crystalline barium titanate. *Nanoscale* **10**, 18074–18079 (2018).
232. Kim, R. H. J., Park, J. M., Haeuser, S. J., Luo, L. & Wang, J. A sub-2 Kelvin cryogenic magneto-terahertz scattering-type scanning near-field optical microscope (cm-THz-sSNOM). *Rev. Sci. Instrum.* **94**, 043702 (2023).
233. McLeod, A. S. et al. Multi-messenger nanoprobe of hidden magnetism in a strained manganite. *Nat. Mater.* **19**, 397–404 (2020).
234. Zhou, Y. et al. Thermal and electrostatic tuning of surface phonon-polaritons in LaAlO<sub>3</sub>/SrTiO<sub>3</sub> heterostructures. *Nat. Commun.* **14**, 7686 (2023).
235. Ni, G. et al. Long-lived phonon polaritons in hyperbolic materials. *Nano Lett.* **21**, 5767–5773 (2021).
236. Nishida, J. et al. Ultrafast infrared nano-imaging of far-from-equilibrium carrier and vibrational dynamics. *Nat. Commun.* **13**, 1083 (2022).
237. Wagner, M. et al. Ultrafast and nanoscale plasmonic phenomena in exfoliated graphene revealed by infrared pump–probe nanoscopy. *Nano Lett.* **14**, 894–900 (2014).  
**This work demonstrates ultrafast time-resolved s-SNOM with a time resolution below 100 fs.**
238. Sternbach, A. J. et al. Artifact free time resolved near-field spectroscopy. *Opt. Express* **25**, 28589 (2017).
239. Plankl, M. et al. Subcycle contact-free nanoscopy of ultrafast interlayer transport in atomically thin heterostructures. *Nat. Photon.* **15**, 594–600 (2021).
240. Dönges, S. A. et al. Ultrafast nanoimaging of the photoinduced phase transition dynamics in VO<sub>2</sub>. *Nano Lett.* **16**, 3029–3035 (2016).
241. Pushkarev, V. et al. Charge transport in single-crystalline GaAs nanobars: impact of band bending revealed by terahertz spectroscopy. *Adv. Funct. Mater.* **32**, 2107403 (2022).
242. Pizzuto, A. et al. Nonlocal time-resolved terahertz spectroscopy in the near field. *ACS Photon.* **8**, 2904–2911 (2021).
243. Siday, T. et al. Ultrafast nanoscopy of high-density exciton phases in WSe<sub>2</sub>. *Nano Lett.* **22**, 2561–2568 (2022).
244. Mrejen, M., Yadgarov, L., Levanon, A. & Suchowski, H. Transient exciton–polariton dynamics in WSe<sub>2</sub> by ultrafast near-field imaging. *Sci. Adv.* **5**, eaat9618 (2019).
245. Vitalone, R. A. et al. Nanoscale femtosecond dynamics of mott insulator (Ca<sub>0.99</sub>Sr<sub>0.01</sub>)<sub>2</sub>RuO<sub>4</sub>. *Nano Lett.* **22**, 5689–5697 (2022).
246. Sternbach, A. J. et al. Nanotextured dynamics of a light-induced phase transition in VO<sub>2</sub>. *Nano Lett.* **21**, 9052–9060 (2021).
247. Charnukha, A. et al. Ultrafast nonlocal collective dynamics of Kane plasmon-polaritons in a narrow-gap semiconductor. *Sci. Adv.* **5**, eaau9956 (2019).
248. Li, J. et al. Ultrafast optical nanoscopy of carrier dynamics in silicon nanowires. *Nano Lett.* **23**, 1445–1450 (2023).
249. Sternbach, A. J. et al. Programmable hyperbolic polaritons in van der Waals semiconductors. *Science* **371**, 617–620 (2021).
250. Huber, M. A. et al. Femtosecond photo-switching of interface polaritons in black phosphorus heterostructures. *Nat. Nanotechnol.* **12**, 207–211 (2017).
251. Ni, G. X. et al. Ultrafast optical switching of infrared plasmon polaritons in high-mobility graphene. *Nat. Photon.* **10**, 244–247 (2016).
252. He, M. et al. Polariton design and modulation via van der Waals/doped semiconductor heterostructures. *Nat. Commun.* **14**, 7965 (2023).
253. Luferau, A. et al. Hot-electron dynamics in a semiconductor nanowire under intense THz excitation. *ACS Photon.* **11**, 3123–3130 (2024).
254. Dong, Y. et al. Fizeau drag in graphene plasmonics. *Nature* **594**, 513–516 (2021).
255. Zhao, W. et al. Efficient Fizeau drag from Dirac electrons in monolayer graphene. *Nature* **594**, 517–521 (2021).
256. Zhang, J. et al. Nano-resolved current-induced insulator–metal transition in the Mott insulator Ca<sub>2</sub>RuO<sub>4</sub>. *Phys. Rev. X* **9**, 11032 (2019).
257. Dapolito, M. et al. Infrared nano-imaging of Dirac magnetoexcitons in graphene. *Nat. Nanotechnol.* **18**, 1409–1415 (2023).  
**This work demonstrates s-SNOM nano-imaging in a magnetic field up to 7 T.**
258. Blundo, E. et al. Vibrational properties in highly strained hexagonal boron nitride bubbles. *Nano Lett.* **22**, 1525–1533 (2022).
259. Khatib, O. et al. Graphene-based platform for infrared near-field nanospectroscopy of water and biological materials in an aqueous environment. *ACS Nano* **9**, 7968–7975 (2015).
260. Meireles, L. M. et al. Synchrotron infrared nanospectroscopy on a graphene chip. *Lab Chip* **19**, 3678–3684 (2019).
261. Zhao, X. et al. In vitro investigation of protein assembly by combined microscopy and infrared spectroscopy at the nanometer scale. *Proc. Natl Acad. Sci. USA* **119**, e2200019119 (2022).
262. Lu, Y.-H. et al. Infrared nanospectroscopy at the graphene–electrolyte interface. *Nano Lett.* **19**, 5388–5393 (2019).  
**This work introduces a suspended graphene liquid cell device that enables in situ nano-FTIR spectroscopy of solid–liquid interfaces.**
263. He, X., Larson, J. M., Bechtel, H. A. & Kostecký, R. In situ infrared nanospectroscopy of the local processes at the Li/polymer electrolyte interface. *Nat. Commun.* **13**, 1398 (2022).  
**In this work, nano-FTIR spectroscopy is used to show how the local chemistry of an Li/polymer electrolyte interface is modified by Li plating.**
264. Baü, E., Gözl, T., Benoit, M., Tittel, A. & Keilmann, F. Nanoscale mechanical manipulation of ultrathin SiN membranes enabling infrared near-field microscopy of liquid-immersed samples. *Small* **20**, 2402568 (2024).
265. O’Callahan, B. T. et al. In liquid infrared scattering scanning near-field optical microscopy for chemical and biological nanoimaging. *Nano Lett.* **20**, 4497–4504 (2020).
266. Virmani, D. et al. Amplitude- and phase-resolved infrared nanoimaging and nanospectroscopy of polaritons in a liquid environment. *Nano Lett.* **21**, 1360 (2021).
267. Emelianov, N. A. et al. Nanoscale visualization of photodegradation dynamics of MAPbI<sub>3</sub> perovskite films. *J. Phys. Chem. Lett.* **13**, 2744–2749 (2022).
268. Szostak, R. et al. Nanoscale mapping of chemical composition in organic–inorganic hybrid perovskite films. *Sci. Adv.* **5**, eaaw6619 (2023).  
**This paper demonstrates nano-FTIR spectroscopy of the chemical composition in organic–inorganic hybrid perovskite films.**
269. Gross, E. Challenges and opportunities in IR nanospectroscopy measurements of energy materials. *Nano Res.* **12**, 2200–2210 (2019).
270. Zhao, W. & Johnson, C. M. Perspective — nano infrared microscopy: obtaining chemical information on the nanoscale in corrosion studies. *J. Electrochem. Soc.* **166**, C3456 (2019).
271. Hu, X., Zhou, L., Wu, X. & Peng, Y. Review on near-field detection technology in the biomedical field. *Adv. Photon. Nexus* **2**, 044002 (2023).
272. Wang, H., Xie, Q. & Xu, X. G. Super-resolution mid-infrared spectro-microscopy of biological applications through tapping mode and peak force tapping mode atomic force microscope. *Adv. Drug Deliv. Rev.* **180**, 114080 (2022).
273. Ho, K. et al. Nanoscale subsurface morphologies in block copolymer thin films revealed by combined near-field infrared microscopy and mechanical mapping. *ACS Appl. Polym. Mater.* **1**, 933–938 (2019).
274. Kotov, N. et al. Elucidating the fine-scale structural morphology of nanocellulose by nano infrared spectroscopy. *Carbohydr. Polym.* **302**, 120320 (2023).



275. De Los Santos Pereira, A. et al. Conformation in ultrathin polymer brush coatings resolved by infrared nanoscopy. *Anal. Chem.* **92**, 4716–4720 (2020).
276. Peñas, M. I. et al. Nanostructural organization of thin films prepared by sequential dip-coating deposition of poly(butylene succinate), poly( $\epsilon$ -caprolactone) and their copolyesters (PBS-ran-PCL). *Polymer* **226**, 123812 (2021).
277. Eliaz, D. et al. Micro and nano-scale compartments guide the structural transition of silk protein monomers into silk fibers. *Nat. Commun.* **13**, 7856 (2022).
278. Qin, N. et al. Nanoscale probing of electron-regulated structural transitions in silk proteins by near-field IR imaging and nano-spectroscopy. *Nat. Commun.* **7**, 13079 (2016).
279. Kästner, B. et al. Infrared nanospectroscopy of phospholipid and surfactin monolayer domains. *ACS Omega* **3**, 4141–4147 (2018).
280. Cernescu, A. et al. Label-free infrared spectroscopy and imaging of single phospholipid bilayers with nanoscale resolution. *Anal. Chem.* **90**, 10179–10186 (2018).
281. Geith, T., Amarie, S., Milz, S., Bamberg, F. & Keilmann, F. Visualisation of methacrylate-embedded human bone sections by infrared nanoscopy. *J. Biophoton.* **7**, 418–424 (2014).
282. Zancajo, V. M. R. et al. FTIR nanospectroscopy shows molecular structures of plant biominerals and cell walls. *Anal. Chem.* **92**, 13694–13701 (2020).
283. Yesiltaş, M. et al. Biconical reflectance, micro-Raman, and nano-FTIR spectroscopy of the Didim (H3-5) meteorite: chemical content and molecular variations. *Meteorit. Planet. Sci.* **55**, 2404–2421 (2020).
284. David, O. et al. Correlating gas permeability and morphology of bio-based polyether-block-amide copolymer membranes by IR nanospectroscopy. *J. Membr. Sci.* **708**, 123001 (2024).
285. Müller, E. A., Pollard, B., Bechtel, H. A., Van Blerkom, P. & Raschke, M. B. Infrared vibrational nano-crystallography and nano-imaging. *Sci. Adv.* **2**, e1601006 (2016).
286. Xue, M. et al. Single-vesicle infrared nanoscopy for noninvasive tumor malignancy diagnosis. *J. Am. Chem. Soc.* **144**, 20278–20287 (2022).
287. Chevigny, R. et al. Nanoscale probing of the supramolecular assembly in a two-component gel by near-field infrared spectroscopy. *Chem. Eur. J.* **29**, e202300155 (2023).
288. Qin, T.-X. et al. Quantification of electron accumulation at grain boundaries in perovskite polycrystalline films by correlative infrared-spectroscopic nanoimaging and Kelvin probe force microscopy. *Light Sci. Appl.* **10**, 84 (2021).
289. Schäffer, S. et al. Imaging the terahertz nanoscale conductivity of polycrystalline CsPbBr<sub>3</sub> perovskite thin films. *Nano Lett.* **23**, 2074–2080 (2023).
290. Zhang, H.-T. et al. Reconfigurable perovskite nickelate electronics for artificial intelligence. *Science* **375**, 533–539 (2022).
291. Latypova, A. F. et al. Design principles for organic small molecule hole-transport materials for perovskite solar cells: film morphology matters. *ACS Appl. Energy Mater.* **5**, 5395–5403 (2022).
292. Komissarova, E. A. et al. Novel benzodithiophene-TTBTBT copolymers: synthesis and investigation in organic and perovskite solar cells. *Sustain. Energy Fuels* **6**, 3542–3550 (2022).
293. Lucas, I. T. et al. IR near-field spectroscopy and imaging of single Li<sub>2</sub>FePO<sub>4</sub> microcrystals. *Nano Lett.* **15**, 1–7 (2015).
294. Gamage, S. et al. Probing structural changes in single enveloped virus particles using nano-infrared spectroscopic imaging. *PLoS ONE* **13**, e0199112 (2018).
295. Bakir, G. et al. Orientation matters: polarization dependent IR spectroscopy of collagen from intact tendon down to the single fibril level. *Molecules* **25**, 4295 (2020).
296. Greaves, G. E., Kiryushko, D., Auner, H. W., Porter, A. E. & Phillips, C. C. Label-free nanoscale mapping of intracellular organelle chemistry. *Commun. Biol.* **6**, 583 (2023).
297. Kanevche, K. et al. Infrared nanoscopy and tomography of intracellular structures. *Commun. Biol.* **4**, 1341 (2021).
298. Freitas, R. O. et al. Nano-infrared imaging of primary neurons. *Cells* **10**, 2559 (2021).
299. Goikoetxea, M. et al. Cross-sectional chemical nanoimaging of composite polymer nanoparticles by infrared nanospectroscopy. *Macromolecules* **54**, 995–1005 (2021).
300. Rose, M.-A. et al. Local inhomogeneities resolved by scanning probe techniques and their impact on local 2DEG formation in oxide heterostructures. *Nanoscale Adv.* **3**, 4145–4155 (2021).
301. Hesp, N. C. H. et al. Nano-imaging photoresponse in a moiré unit cell of minimally twisted bilayer graphene. *Nat. Commun.* **12**, 1640 (2021).
302. Alonso-González, P. et al. Acoustic terahertz graphene plasmons revealed by photocurrent nanoscopy. *Nat. Nanotechnol.* **12**, 31 (2017).
303. Soltani, A. et al. Direct nanoscopic observation of plasma waves in the channel of a graphene field-effect transistor. *Light Sci. Appl.* **9**, 97 (2020).
304. Pogna, E. A. A. et al. Unveiling the detection dynamics of semiconductor nanowire photodetectors by terahertz near-field nanoscopy. *Light Sci. Appl.* **9**, 189 (2020).
305. Yao, K. et al. Plasmon-induced trap filling at grain boundaries in perovskite solar cells. *Light Sci. Appl.* **10**, 219 (2021).
306. Chaudhary, K. et al. Polariton nanophotonics using phase-change materials. *Nat. Commun.* **10**, 4487 (2019).
307. Dolado, I. et al. Nanoscale guiding of infrared light with hyperbolic volume and surface polaritons in van der Waals material ribbons. *Adv. Mater.* **32**, 1906530 (2020).
308. Zenin, V. A. et al. Direct amplitude-phase near-field observation of higher-order anapole states. *Nano Lett.* **17**, 7152–7159 (2017).
309. Alfaro-Mozaz, F. J. et al. Hyperspectral nanoimaging of van der Waals polaritonic crystals. *Nano Lett.* **21**, 7109–7115 (2021).
310. Herzog Sheinfux, H. et al. Transverse hypercrystals formed by periodically modulated phonon polaritons. *ACS Nano* **17**, 7377–7383 (2023).
311. Xiong, L. et al. Photonic crystal for graphene plasmons. *Nat. Commun.* **10**, 4780 (2019).
312. Yang, J. et al. Near-field excited archimedean-like tiling patterns in phonon-polaritonic crystals. *ACS Nano* **15**, 9134–9142 (2021).
313. Duan, J. et al. Multiple and spectrally robust photonic magic angles in reconfigurable  $\alpha$ -MoO<sub>3</sub> trilayers. *Nat. Mater.* **22**, 867–872 (2023).
314. Hu, G. et al. Topological polaritons and photonic magic angles in twisted  $\alpha$ -MoO<sub>3</sub> bilayers. *Nature* **582**, 209–213 (2020).
315. Folland, T. G. et al. Reconfigurable infrared hyperbolic metasurfaces using phase change materials. *Nat. Commun.* **9**, 4371 (2018).
316. Wu, C. Y. et al. High-spatial-resolution mapping of catalytic reactions on single particles. *Nature* **541**, 511–515 (2017).
- In this work, nano-FTIR spectroscopy using synchrotron radiation shows that the peripheries of Pt particles are more active in catalysing oxidation and reduction reactions.**
317. Say, Z. et al. Unraveling molecular fingerprints of catalytic sulfur poisoning at the nanometer scale with near-field infrared spectroscopy. *J. Am. Chem. Soc.* **144**, 8848–8860 (2022).
318. Johnson, C. M. & Böhmmler, M. Nano-FTIR microscopy and spectroscopy studies of atmospheric corrosion with a spatial resolution of 20 nm. *Corros. Sci.* **108**, 60–65 (2016).
319. Zhao, W., Chang, T., Leygraf, C. & Johnson, C. M. Corrosion inhibition of copper with octadecylphosphonic acid (ODPA) in a simulated indoor atmospheric environment. *Corros. Sci.* **192**, 109777 (2021).
320. Vogel, C. et al. Air and chlorine gas corrosion of different silicon carbides analyzed by nano-Fourier-transform infrared (nano-FTIR) spectroscopy. *Corros. Sci.* **131**, 324–329 (2018).
321. Nepel, T. C. M. et al. In situ infrared micro and nanospectroscopy for discharge chemical composition investigation of non-aqueous lithium-air cells. *Adv. Energy Mater.* **11**, 2101884 (2021).
322. Yalcin, S. E., Legg, B. A., Yeşilbaş, M., Malvankar, N. S. & Boily, J.-F. Direct observation of anisotropic growth of water films on minerals driven by defects and surface tension. *Sci. Adv.* **6**, eaaz9708 (2024).
323. Bai, Y. et al. Protein nanoribbons template enamel mineralization. *Proc. Natl Acad. Sci. USA* **117**, 19201–19208 (2020).
324. Luibrand, T. et al. Characteristic length scales of the electrically induced insulator-to-metal transition. *Phys. Rev. Res.* **5**, 13108 (2023).
325. Aghamiri, N. A. et al. Reconfigurable hyperbolic polaritonics with correlated oxide metasurfaces. *Nat. Commun.* **13**, 4511 (2022).
326. Zhang, S. S. et al. Nano-infrared imaging of metal insulator transition in few-layer 1T-TaS<sub>2</sub>. *Nanophotonics* **12**, 2841–2847 (2023).
327. Walter, B. et al. Terahertz near-field imaging using batch-fabricated cantilevers with 70  $\mu$ m long tips. In *Int. Conf. Infrared Millimeter Terahertz Waves (IEEE)*, (2019).
328. Xia-Hou, Y.-J. et al. Graphene-coated conductive probes with enhanced sensitivity for nanoIR spectroscopy. *Nano Res.* **16**, 11326–11333 (2023).
329. Xu, S. et al. Electronic interactions in Dirac fluids visualized by nano-terahertz spacetime interference of electron-photon quasiparticles. *Sci. Adv.* **10**, eado5553 (2024).
330. Siday, T. et al. All-optical subcycle microscopy on atomic length scales. *Nature* **629**, 329–334 (2024).
331. Heeres, R. W., Kouwenhoven, L. P. & Zwiller, V. Quantum interference in plasmonic circuits. *Nat. Nanotechnol.* **8**, 719–722 (2013).
332. Leon, C. C. et al. Photon superbunching from a generic tunnel junction. *Sci. Adv.* **5**, eaav4986 (2023).
333. Pollard, B. & Raschke, M. B. Correlative infrared nanospectroscopic and nanomechanical imaging of block copolymer microdomains. *Beilstein J. Nanotechnol.* **7**, 605–612 (2016).
334. Barnett, J. et al. Far-infrared near-field optical imaging and Kelvin probe microscopy of laser-crystallized and -amorphized phase change material Ge<sub>3</sub>Sb<sub>2</sub>Te<sub>6</sub>. *Nano Lett.* **21**, 9012–9020 (2021).
335. Zhang, S. et al. Visualizing moiré ferroelectricity via plasmons and nano-photocurrent in graphene/twisted-WSe<sub>2</sub> structures. *Nat. Commun.* **14**, 6200 (2023).
336. Wang, H., Wang, L., Jakob, D. S. & Xu, X. G. Tomographic and multimodal scattering-type scanning near-field optical microscopy with peak force tapping mode. *Nat. Commun.* **9**, 2005 (2018).
337. Palato, S., Schwendke, P., Grosse, N. B. & Stähler, J. Pseudoheterodyne near-field imaging at kHz repetition rates via quadrature-assisted discrete demodulation. *Appl. Phys. Lett.* **120**, 131601 (2022).
338. Wang, H., Wang, L. & Xu, X. G. Scattering-type scanning near-field optical microscopy with low-repetition-rate pulsed light source through phase-domain sampling. *Nat. Commun.* **7**, 13212 (2016).
339. Xu, S. et al. Deep learning analysis of polaritonic wave images. *ACS Nano* **15**, 18182–18191 (2021).
340. Guo, X., Bertling, K. & Rakić, A. D. Optical constants from scattering-type scanning near-field optical microscope. *Appl. Phys. Lett.* **118**, 041103 (2021).
341. Gamage, S. et al. Nanoscopy of black phosphorus degradation. *Adv. Mater. Interfaces* **3**, 1600121 (2016).
342. Gamage, S. et al. Infrared nanoimaging of hydrogenated perovskite nickelate memristive devices. *ACS Nano* **18**, 2105–2116 (2024).
343. Dopilka, A., Gu, Y., Larson, J. M., Zorba, V. & Kostecki, R. Nano-FTIR spectroscopy of the solid electrolyte interphase layer on a thin-film silicon li-ion anode. *ACS Appl. Mater. Interfaces* **15**, 6755–6767 (2023).

344. Ayache, M., Lux, S. F. & Kostecki, R. IR near-field study of the solid electrolyte interphase on a tin electrode. *J. Phys. Chem. Lett.* **6**, 1126–1129 (2015).
345. Ayache, M., Jang, D., Syzdek, J. & Kostecki, R. Near-field IR nanoscale imaging of the solid electrolyte interphase on a HOPG electrode. *J. Electrochem. Soc.* **162**, A7078 (2015).
346. Shan, Y. et al. Nanometre-resolved observation of electrochemical microenvironment formation at the nanoparticle–ligand interface. *Nat. Catal.* **7**, 422–431 (2024).
347. Tesema, T. E., McFarland-Porter, R., Zerai, E., Grey, J. & Habteyes, T. G. Hierarchical self-assembly and chemical imaging of nanoscale domains in polymer blend thin films. *J. Phys. Chem. C* **126**, 7764–7772 (2022).
348. Meyns, M. et al. Multi-feature round silicon membrane filters enable fractionation and analysis of small micro- and nanoplastics with Raman spectroscopy and nano-FTIR. *Anal. Methods* **15**, 606–617 (2022).
349. Hartmann, N., Wang, X. & Huber, A. J. Nanoscale THz imaging and spectroscopy at ambient and cryogenic sub 10K temperatures. In *Int. Conf. Infrared Millimeter Terahertz Waves* (IEEE, 2021).
350. Kim, R. H. J. et al. Terahertz nano-imaging of electronic strip heterogeneity in a Dirac semimetal. *ACS Photon.* **8**, 1873–1880 (2021).
351. Jing, R. et al. Phase-resolved terahertz nanoimaging of WTe<sub>2</sub> microcrystals. *Phys. Rev. B* **107**, 155413 (2023).
352. Jing, R. et al. Terahertz response of monolayer and few-layer WTe<sub>2</sub> at the nanoscale. *Nat. Commun.* **12**, 5594 (2021).
353. Sun, Z., Fogler, M. M., Basov, D. N. & Millis, A. J. Collective modes and terahertz near-field response of superconductors. *Phys. Rev. Res.* **2**, 23413 (2020).
354. Stinson, H. T. et al. Infrared nanospectroscopy and imaging of collective superfluid excitations in anisotropic superconductors. *Phys. Rev. B* **90**, 14502 (2014).
355. Lu, Q. et al. Surface Josephson plasma waves in a high-temperature superconductor. *npj Quantum Mater.* **5**, 69 (2020).
356. Wilcken, R. et al. Antenna-coupled infrared nanospectroscopy of intramolecular vibrational interaction. *Proc. Natl Acad. Sci. USA* **120**, e2220852120 (2023).
357. Muller, E. A. et al. Nanoimaging and control of molecular vibrations through electromagnetically induced scattering reaching the strong coupling regime. *ACS Photon.* **5**, 3594 (2018).
358. Dolado, I. et al. Remote near-field spectroscopy of vibrational strong coupling between organic molecules and phononic nanoresonators. *Nat. Commun.* **13**, 6850 (2022).
359. Bylinkin, A. et al. Real-space observation of vibrational strong coupling between propagating phonon polaritons and organic molecules. *Nat. Photon.* **15**, 197–202 (2021).
360. Wang, C.-F. et al. Observation of intersubband polaritons in a single nanoantenna using nano-FTIR spectroscopy. *Nano Lett.* **19**, 4620–4626 (2019).
361. Casses, L. N. et al. Full quantitative near-field characterization of strongly coupled exciton–plasmon polaritons in thin-layered WSe<sub>2</sub> on a monocrystalline gold platelet. *ACS Photon.* **11**, 3593–3601 (2024).
362. Hirschmann, O., Bhakta, H. H., Kort-Kamp, W. J. M., Jones, A. C. & Xiong, W. Spatially resolved near field spectroscopy of vibrational polaritons at the small N limit. *ACS Photon.* **11**, 2650–2658 (2024).
363. Wang, Y. et al. Tip-enhanced imaging and control of infrared strong light–matter interaction. *Laser Photon. Rev.* **18**, 2301148 (2024).
364. Wehmeier, L. et al. Landau-phonon polaritons in Dirac heterostructures. *Sci. Adv.* **10**, eadp3487 (2024).
365. Krouski, D., Dazzi, A., Zenobi, R. & Centrone, A. Infrared and Raman chemical imaging and spectroscopy at the nanoscale. *Chem. Soc. Rev.* **49**, 3315–3347 (2020).
366. Bailo, E. & Deckert, V. Tip-enhanced Raman scattering. *Chem. Soc. Rev.* **37**, 921–930 (2008).
367. Mauser, N. & Hartschuh, A. Tip-enhanced near-field optical microscopy. *Chem. Soc. Rev.* **43**, 1248–1262 (2014).
368. Verma, P. Tip-enhanced Raman spectroscopy: technique and recent advances. *Chem. Rev.* **117**, 6447–6466 (2017).
369. Centrone, A. Infrared imaging and spectroscopy beyond the diffraction limit. *Ann. Rev. Anal. Chem.* **8**, 101–126 (2015).
370. Sifat, A. A., Jahng, J. & Potma, E. O. Photo-induced force microscopy (PiFM) — principles and implementations. *Chem. Soc. Rev.* **51**, 4208–4222 (2022).
371. Klarskov, P., Kim, H., Colvin, V. L. & Mittleman, D. M. Nanoscale laser terahertz emission microscopy. *ACS Photon.* **4**, 2676–2680 (2017).
372. Pizzuto, A., Mittleman, D. M. & Klarskov, P. Laser THz emission nanoscopy and THz nanoscopy. *Opt. Express* **28**, 18778–18789 (2020).
373. Barber, M. E., Ma, E. Y. & Shen, Z.-X. Microwave impedance microscopy and its application to quantum materials. *Nat. Rev. Phys.* **4**, 61–74 (2022).
374. Ma, Q., Krishna Kumar, R., Xu, S. Y., Koppens, F. H. L. & Song, J. C. W. Photocurrent as a multiphysics diagnostic of quantum materials. *Nat. Rev. Phys.* **5**, 170–184 (2023).
375. Woessner, A. et al. Near-field photocurrent nanoscopy on bare and encapsulated graphene. *Nat. Commun.* **7**, 10783 (2016).
376. Ni, G. X. et al. Nanoscale infrared spectroscopy and imaging of catalytic reactions in Cu<sub>2</sub>O crystals. *ACS Photon.* **7**, 576–580 (2020).

## Acknowledgements

R.H. received financial support from Grant CEX2020-001038-M funded by MICIU/AEI/10.13039/501100011033 and Grant PID2021-123949OB-I00 (NANOSPEC) funded by MICIU/AEI/10.13039/501100011033 and by ERDF/EU. Y.A. acknowledges K.C. Goretta, the Air Force Office of Scientific Research (AFOSR) grant number FA9550-23-1-0375 and the Gordon and Betty Moore Foundation, GBMF12246. X.C., M.L. and D.N.B. acknowledge support from Programmable Quantum Materials, an Energy Frontier Research Center funded by the US Department of Energy (DOE), Office of Science, Basic Energy Sciences (BES), under award DE-SC0019443. M.L. also acknowledges Gordon and Betty Moore Foundation. Research at Columbia in van der Waals materials is supported as part of Programmable Quantum Materials, an Energy Frontier Research Center funded by the US DOE, Office of Science, BES, DE-SC0019443. Research at Columbia at charge transfer structures is supported by DOE-BES DE-SC0018426. Research at Columbia in topological materials is supported NSF-DMR DMR 2210186. D.N.B. is a Moore Investigator in quantum materials EPIQS GBMF9455. R.H. thanks F. Keilmann, L. Mester, M. Goikoetxea, A. Govyadinov, I. Niehues and M. Quijada for discussions and feedback on the manuscript. Y.A. acknowledges H. Bechtel, Z.H. Kim, M. Asjad and A. Alu for their constructive input. X.C. and M.L. acknowledge discussions with L. Wehmeier and J. Zhang.

## Author contributions

Y.A. proposed the initial idea and structure of this Review. R.H. completed the main text, with contributions and figures from Y.A., M.L. and X.C., and input from D.N.B. All authors contributed to the selection of key references used in this Review.

## Competing interests

R.H. is a co-founder of Neaspec, now part of attocube systems, a company producing scattering-type scanning near-field optical microscope systems, such as the one described in this Review. The remaining authors declare no competing interests.

## Additional information

**Supplementary information** The online version contains supplementary material available at <https://doi.org/10.1038/s41578-024-00761-3>.

**Peer review information** *Nature Reviews Materials* thanks Raul Freitas, who co-reviewed with Flavio Henrique Feres, and Eric Muller for their contribution to the peer review of this work.

**Publisher's note** Springer Nature remains neutral with regard to jurisdictional claims in published maps and institutional affiliations.

Springer Nature or its licensor (e.g. a society or other partner) holds exclusive rights to this article under a publishing agreement with the author(s) or other rightsholder(s); author self-archiving of the accepted manuscript version of this article is solely governed by the terms of such publishing agreement and applicable law.

© Springer Nature Limited 2025